Crystal Plasticity Finite Element Models for Predicting Deformation and Twinning in Polycrystalline Magnesium Alloys

by

Jiahao Cheng

A dissertation submitted to The Johns Hopkins University in conformity with the requirements for the degree of Doctor of Philosophy.

Baltimore, Maryland

February, 2016

Abstract

Magnesium alloys exhibit complex deformation related mechanical behavior, viz. plastic anisotropy, tension-compression asymmetry and premature failure. Their origins are in the underlying heterogeneous deformation due to dislocation slip and deformation twinning on different crystallographic systems. In the polycrystalline microstructure, the twin formations lead to strain localization and initiation of short cracks. Reliable prediction of mechanical response and material failure is predicated upon the ability of computational models of polycrystalline microstructures to accurately simulate the heterogeneous twin formations and deformation.

In this dissertation, a novel crystal plasticity finite element (CPFE) model is developed to predict the micro-mechanism and microstructure induced material failure in Mg alloys. The model accounts for dislocation slips, explicit micro-twin nucleation-propagation, geometrically necessary dislocation (GND) accumulation and stress/strain localization in the evolving microstructure. The micro-twin nucleation is modeled based on energy-partitioning following the dislocation dissociation process. The micro-twin propagation and associated localized plastic flow are described with micro-mechanism based crystal plasticity constitutive relations. The model predicts the twin-evolution-induced material re-

sponses at multi-scales, including at macroscopic scale the tension-compression asymmetry and the dramatic change of hardening rates due to twin activities, as well as at microscopic scale the strain localization and stress redistribution in the twined microstructure which is potentially responsible for short-crack initiation.

The proposed model is implemented with a new developed stabilized tetrahedral element, which avoids inaccuracy of micro-twin nucleation prediction due to element-locking. The simulation time steps are constrained by the high propagation rate of micro-twins and are several orders smaller than that of regular CPFE simulations. This increases the computation cost enormously and impedes high-fidelity CPFE simulation. A multi-time-scale subcycling algorithm for temporal integration of CPFE-twin model is innovated to improve the simulation efficiency. The algorithm divides the FE domain into sub-domains and computes local deformation in separate rates, followed by the coupling of residual forces to satisfy the global equilibrium. Significant acceleration is achieved using this method without compromising on the accuracy. The CPFE twin models, stabilized and accelerated with the proposed numerical methods, predict the microstructure-property relations and extend the study of failure initiation in single and polycrystalline Mg alloys.

ABSTRACT

Dissertation Committee:

Professor Somnath Ghosh, Advisor

Professor James K. Guest

Professor Michael D. Shields

Professor Kevin J. Hemker

Professor Jaafar A. El-Awady

Acknowledgments

It is difficult to overstate my gratitude to my advisor Prof. Somnath Ghosh, who has provided me with excellent guidance, unwavering support and continuous encouragement throughout my Ph.D. years. He sets an excellent example of a true scholar with innovative visions and never-dimming enthusiasm to the scientific research, which inspires me immensely.

I would also like to thank Prof. Kevin Hemker, Prof. Jaafar El-Awady, Prof. Timothy Weihs, Prof. James Guest and Prof. Michael Shields for being on my committee. My deepest thanks to my friends and lab-mates Jiaxi, Shu and Coleman for their constant help, support and companionship. I want to express my sincere appreciation to Prof. Fan Yang and Prof. Yuli Chen, who helped me patiently in my early days of working in the field of computational mechanics and left me with many good memories in doing research. I would like to thank Ahmad, Akbar, Deniz, Dhiru, George, Pritam, Reza, Shariyar, Shinu, Shravan, Subhendu, Xiaohui, Xiaofan, Yan, Zhiye and all the previous members of our lab for many insightful discussions in research and the good time that you spent with me.

My sincere thanks to Dr. Raja Mishra in General Motors Research & Development Center for providing experimental data. I would like to acknowledgment Dr. Thomas Siegmund, Program Manager US National Science Foundation (grant # CMMI-1100818) for

supporting this effort. I want to thank the staffs at Ohio Supercomputer Center, Homewood High-Performance Cluster and Maryland Advanced Research Computing Center for helping me work with the super-computers.

Finally, I would like to express my heartfelt gratitude to my wife, my parents and my sister for their long-time sacrifice and support.

This work is dedicated to my parents, my little sister, and my parents-in-law for their unconditional love and support in my life, and especially to Min and Alisa, my beloved wife and daughter, who have always been my strength in the deepest of my heart.

Contents

List of Tables

List of Figures

Chapter 1

Introduction

The quest for low density, high strength and durable materials in high performance automotive and aerospace applications has resulted in magnesium alloys as candidate materials with high potential [2, 3]. The density of magnesium is about 23% that of steel and 66% that of aluminum while its weight for equivalent bending stiffness is 62% less than steel and 23% less than aluminum. Being among the lightest of structural metals with high stiffness and strength at a range of temperatures, these alloys can offer considerably increased component strength to weight ratio. These desirable properties can have the ultimate consequences of significant savings in energy consumption and reduction in CO_2 emissions. An important consideration in the processing and high-performance industrial applications of Mg alloys is their deformation behavior and failure characteristics over a range of strain rates and temperatures. Of particular interest is their ductility properties, e.g. their behavior in forming processes like extrusion or rolling, or under impact loads as in crashworthiness tests. Understanding the physics of the plastic deformation and failure of magnesium alloys is, therefore, essential for tailoring their ductility, especially at room temperatures.

A complicating phenomenon of magnesium and its alloys (e.g., AZ31) is their deformation induced anomalous mechanical behavior [4–10]. These materials possess low-symmetry hexagonal closed packed (*hcp*) crystallographic structure, an attribute that leads to pronounced anisotropy in mechanical properties, e.g. tension-compression asymmetry of the yield strength. Low symmetry results in a variety of slip systems for the *hcp* crystalline lattice, shown in figure 2.1. At low temperatures, the critical resolved shear stress (CRSS) is much smaller for basal slip $(0001)\left\langle 11\bar{2}0\right\rangle$, than it is for prismatic $\{10\bar{1}0\}\left\langle 11\bar{2}0\right\rangle$ or pyramidal $\{11\bar{2}2\}\left\langle 11\bar{2}3\right\rangle$ slip systems [11]. Only the basal $\langle a\rangle$ slip can occur under low applied stresses. Any deformation involving changes in the $\langle c\rangle$ direction ensues a competition between the high CRSS $\langle c+a\rangle$ slip systems and the less understood micro-twin mechanisms [12]. The myriad of interactions among slip and twin systems lead to complex plastic behavior, involving plastic anisotropy, tension-compression asymmetry, and premature failure. Local stress and dislocation concentrations at locations of microstructural heterogeneities in polycrystalline aggregates close to grain boundaries with strong texture and grain size distribution are responsible for the micro-twin nucleations. Once a micro-twin nucleates, it propagates rapidly on twin planes and leads to the formation of thin twin bands. The twin band boundaries migrate from one twin plane to the adjacent twin planes and cause an increase in twin thickness[13]. Highly localized deformation occurs within heterogeneous twin bands. Crack initiation has been observed at twin-twin or twin-grain-boundary intersections, which causes premature failure of the material[14]. It is important to develop physics-based models of deformation and micro-twinning in Mg alloys with the goal of

understanding and predicting the effect of microstructure on failure.

Significant computational approaches have been developed for continuum-scale simulation of polycrystal aggregates of Mg alloys. The elasto-visco-plastic self-consistent or EVPSC method started in [15], evolved in [16] and was further developed in [17, 18] to account for large anisotropic viscoplastic deformation. Features like dislocation slip inside a twin band, detwinning, effect of solid solution and dislocation transmutation caused twin hardening have been included for *hcp* crystals in recent developments [19–24]. In the EVPSC scheme, each grain is treated as an ellipsoidal inclusion embedded in a homogeneous medium representing the averaged behavior of all other grains, while preserving equilibrium and compatibility. It is an efficient method for modeling the behavior and texture evolution of large grain aggregates. Grains, however, are not in direct interaction with their neighbors, and the effect of grain boundary, grain shape and stress heterogeneity inside each grain are not explicitly represented. Phase field models [25–28] have been adopted to model deformation twinning. Phase field models consider twinning as a phase transformation as it rotates the anisotropic material stiffness matrix and lead to a higher internal energy. Difficulties of using phase field models exist in the fact that the plastic deformation by dislocation slips is hard to incorporate, and it's computationally expensive to extend to large polycrystalline aggregates to study the effect of the microstructure. Crystal plasticity finite element models or CPFEM have been implemented to model deformation and twins in Mg alloys in [11, 29–33]. These models are based on a pseudo-slip approach which treats twins in the same way as dislocation slip. This method ignores the strain localization

in twin bands and heterogeneous deformation in the evolving microstructure and is incapable of predicting the onset of material failure triggered by heterogeneous micro-twins. Explicit twin formation model using CPFEM [34] is proposed based on phenomenological twin formation criteria and adaptive mesh-regeneration methods. The explicit CPFE twin formation model has potentials to the accurately capture the micro-twin induced material failure if the physics of micro-twin nucleation, propagation and interactions are modeled.

Physics-based constitutive model for deformation twinning is the key to failure prediction for Mg alloys. The formation of micro-twins is facilitated by the small number of easy slip systems in *hcp* metals. However, some important fundamental questions remain, e.g. how does a micro-twin nucleate, how the twin boundary migrate or when does a grain saturate with accommodating twins. The formation of micro-twins by the nucleation and glide of twinning dislocations are not on close packing planes as discussed in [35]. Two types of twin nucleation theories referred to as homogeneous and heterogeneous theories, have been proposed for *hcp* metals. The homogeneous theory [36] assumes nucleation from a perfect crystal lattice, while the heterogeneous theory [37–40] considers the effect of existing defects and microstructure on twinning. The homogeneous models require very high stress, close to material's theoretical strength, which can only happen under extreme loading conditions. The heterogeneous models are more suited for micro-twinning under lower strain rate and quasi-static loading conditions. [39] considered the twin nucleation from defects at low angle grain boundaries. [41] introduced a "pole mechanism", which considers the coplanar dissociation of $\langle c \rangle$ lattice dislocations as a source of twinning. This

was extended in [37] using linear elasticity theory to incorporate the dissociation of a $\langle a \rangle$, $\langle c \rangle$ or $\langle c + a \rangle$ dislocation into one or more glissile twinning dislocation loops and a sessile stair-rod dislocation, lying between the slip plane of the original dislocation and twin planes. In [38] it has been shown that it is not possible to form a stable twin unless it is at the head of a dislocation pileup. Studies on the dissociation of $\langle c \rangle$ and $\langle c + a \rangle$ type dislocation into n layer $\{10\bar{1}2\}$ twins in [40] have found them to be feasible mechanisms for nucleation of $\{10\bar{1}2\}$ tension twins.

The propagation of twin partial dislocations not only requires the uni-directional gliding on twin planes which provides a shear deformation but also requires a collaborative shuffling of atoms over more than one crystallographic plane [42]. This non-planar atomic shuffling, together with twin shear, reorients the initial crystallographic lattice in a mirror-symmetry and thickens the twin. The micro-twin grows in thickness when the twin boundary migrates from one twin plane to the adjacent twin planes. Molecular dynamic (MD) studies of twin boundaries [43] indicates the interactions with basal dislocation slips promotes the twin boundary migration by creating glissile basal-prismatic facets. The high-resolution transmission electron microscopy (TEM) observations [44] of the twin boundaries in Mg alloys AZ31 suggests the dislocations on the non-basal slip systems acts as barriers to twin propagation. Simulations based on three-dimensional discrete dislocation dynamics (DDD) [45] characterize the interaction between discrete dislocation loops with twin boundaries. The simulation results suggest that the competition between the tension-twin-boundaries-induced hardening and twin-growth-induced softening are responsible for

unique macroscopic 'S' shape stress-strain curve observed in Mg alloys.

While CPFEM deems an effective numerical tool for physics-based modeling of the deformation and the micro-twins in the polycrystalline microstructure, two numerical difficulties exist for current CPFE simulations. Firstly severe volumetric locking exists with the linear TET4 elements which are required for meshing the polycrystalline microstructure. The element-locking causes overestimated local stress at plastic deforming regime which is ignored by most CPFE modelers who have been focused on the development of constitutive laws. Secondly, the CPFE constitutive law adopts a power-law model for dislocation slips in HCP materials. The low rate sensitivity of metals at room temperature renders the power-law model a very stiff function that leads to numerical instability when deformation increment is large. The formation of micro-twins causes strain localization in the thin twin bands, which intensify the time step required to stabilize the power-law CPFE model. The very fine time step with high-resolution TET4 mesh increased the computation cost enormously. Multi-time-scale integration algorithm is needed to improve the computation efficiency.

1.1 Organization of the Thesis

The present dissertation develops a CPFE model for dislocation slip and twinning dominated heterogeneous deformation in single and polycrystalline Mg alloy microstructures. The model features local stress concentrations near soft-hard grain boundaries, the accumulation of geometrically necessary dislocations, the microstructures evolution due to the

heterogeneous formation of micro-twins and the deformation localization in the twin bands. In chapter 2 the crystal plasticity constitutive law is developed for dislocation slip and accumulation that is numerically implemented in a large deformation non-linear FE framework. Chapter 3 discusses the instability of the CPFE simulation caused by volumetric-locking of the linear TET4 element and develops two locking-free tetrahedron-mesh-based element formulations for reliable CPFE simulation. The CPFE model for Mg alloys AZ31 is calibrated for parameters and validated with the experimental data in chapter 4. Chapter 5 is devoted to the development of the micro-twin nucleation model in polycrystalline microstructures and detailed study on the effect of microstructure on twin nucleation. Chapter 6 develops a thermal activation based constitutive model for micro-twin propagation, followed by its numerical implementation into CPFE framework for explicit modeling of micro-twin-band formations in the microstructures of RVEs. Chapter 7 constructs a novel subcycling algorithm for multi-time-scale integration of the proposed CPFE twin propagation model. Without the multi-time-scale method, the CPFE twin simulation requires very fine time steps to compute the deformation localization inside twin bands, which increases the computation cost enormously and makes high-fidelity CPFE simulation of RVEs infeasible. Three numerical examples are solved in this chapter to validate the subcycling accelerated CPFE models with twin formation. The thesis is concluded in chapter 8.

Chapter 2

Crystal Plasticity Finite Element Model for Dislocation Slip Dominated Deformation in Mg Alloys

Image-based modeling and simulations of polycrystalline microstructures, using crystal plasticity finite element models, are effective methods for determining microstructure-property relationships. The CPFE models describe dislocation-slip dominated crystallographic plastic deformation in individual grains and polycrystalline aggregates. Deformation mechanisms and texture in CPFE models have been used to model creep and deformation response of metals and alloys in [46–49] using a power law description [50], and the thermally activated theory of plastic flow [51]. Advanced crystal plasticity FE models have been developed in recent years for simulating deformation and failure in a variety of metallic materials. These studies include creep and fatigue simulations for Ti alloys [52–55], dwell fatigue simulations in Ti alloys in [56, 57], cyclic deformation in HSLA steels [58] and hierarchical models of Ni-based superalloys in [59]. Accumulation and hardening of geometric necessary dislocations (GNDs) and statistically stored dislocations (SSDs) are

modeled for heterogeneous deformation and onset of failure in these models. A candidate non-local crystal plasticity model with the features of SSDs and GNDs is developed for slip-dominated deformation in Mg alloys these models in this chapter.

2.1 Large Deformation Non-Linear Finite Element Framework

The finite element weak form of equilibrium equations for a body undergoing finite deformation is obtained by taking the product of the governing equations with a weighting function and integrating over the volume in the current or reference configuration. In an incremental formulation and solution process, where a typical time step transcends discrete temporal points t and $t + \Delta t$, the principle of virtual work for a quasi-static process at time $t + \Delta t$ occupying the domain $\Omega^{t+\Delta t} \subset \mathcal{R}^3$ is written as [60] :

$$\begin{aligned} \int_{\Omega^{t+\Delta t}} (\nabla \delta \mathbf{u}^{t+\Delta t}) : \boldsymbol{\sigma}\, d\Omega^{t+\Delta t} &= \int_{\Omega^{t+\Delta t}} \delta \mathbf{u}^{t+\Delta t} \cdot \mathbf{b}\, d\Omega^{t+\Delta t} \\ &+ \int_{\Gamma_\sigma^{t+\Delta t}} \delta \mathbf{u}^{t+\Delta t} \cdot \bar{\mathbf{t}}\, d\Gamma_\sigma^{t+\Delta t} \quad \forall \delta \mathbf{u}^{t+\Delta t} \in \mathscr{U} \end{aligned} \tag{2.1}$$

where $\boldsymbol{\sigma}$ is the Cauchy stress tensor, $\mathbf{u}$ is the displacement field and $\mathbf{b}$ is the body force per unit volume. The test function $\delta \mathbf{u} = \delta u_i \mathbf{e}_i$ is defined in the space $\mathscr{U}$ of virtual displacements, i.e.

$$\mathscr{U} = \left\{ \delta u_i^{t+\Delta t} \mathbf{e}_i \in H^1(\Omega),\ \delta \mathbf{u}^{t+\Delta t} = \mathbf{0} \text{ on } \Gamma_u \right\} \tag{2.2}$$

where $\mathbf{e}_i$, $i = 1, 2, 3$ are the orthogonal unit basis vectors. The time dependent boundary conditions are:

$$\boldsymbol{\sigma} \cdot \mathbf{n} = \bar{\mathbf{t}} \quad on \ \Gamma_\sigma \qquad \text{and} \qquad \mathbf{u} = \bar{\mathbf{u}} \quad on \ \Gamma_u \tag{2.3}$$

Here $\bar{\mathbf{t}}$ and $\bar{\mathbf{u}}$ are time-dependent prescribed quantities on the traction boundary Γ_σ and displacement boundary Γ_u respectively, where $\Gamma = \Gamma_\sigma \bigcup \Gamma_u$, and $\mathbf{n}$ represents the outward unit vector normal to Γ_σ. An updated Lagrangian formulation is developed in this work [60], where the reference configuration for integrating the weak form corresponds to that at the beginning of the time step, i.e. at time t. In this formulation, the weak form in equation (2.1) reduces to:

$$\int_{\Omega^t} \delta \mathbf{E}_t^{t+\Delta t} : \mathbf{S}_t^{t+\Delta t} \, d\,\Omega^t = R^{ext\,t+\Delta t} \tag{2.4}$$

where

$$\mathbf{u}^{t+\Delta t} = \mathbf{u}^t + \Delta\mathbf{u} \qquad \text{Incremental displacement} \tag{2.5a}$$

$$\mathbf{E}_t^{t+\Delta t} = \frac{1}{2}\left(\frac{\partial \Delta\mathbf{u}}{\partial \mathbf{x}^t} + \left(\frac{\partial \Delta\mathbf{u}}{\partial \mathbf{x}^t}\right)^T + \left(\frac{\partial \Delta\mathbf{u}}{\partial \mathbf{x}^t}\right)^T \frac{\partial \Delta\mathbf{u}}{\partial \mathbf{x}^t}\right) \text{Green-Lagrange strain tensor} \tag{2.5b}$$

$$\mathbf{S}_t^{t+\Delta t} = J_t^{t+\Delta t} \left(\mathbf{F}_t^{t+\Delta t}\right)^{-1} \boldsymbol{\sigma}^{t+\Delta t} \left(\mathbf{F}_t^{t+\Delta t}\right)^{-T} \qquad \text{Second Piola-Kirchhoff stress} \tag{2.5c}$$

$$R^{ext\,t+\Delta t} = \int_{\Omega^{t+\Delta t}} \delta\mathbf{u}^{t+\Delta t}\mathbf{b} \, d\Omega^{t+\Delta t} + \int_{\Gamma_\sigma^{t+\Delta t}} \delta\mathbf{u}^{t+\Delta t}\bar{\mathbf{t}} \, d\Gamma_\sigma^{t+\Delta t} \quad \text{External virtual work} \tag{2.5d}$$

$\mathbf{F}$ corresponds to the deformation gradient tensor and J is its determinant or Jacobian. All quantities in equations (2.5) are at time $t + \Delta t$ and referred to the configuration at time t.

Equation (2.4) may be written in an incremental form as:

$$\int_{\Omega^t} \delta\triangle\mathbf{E} : \triangle\mathbf{S} d\Omega^t + \int_{\Omega^t} \delta\boldsymbol{\eta} : \boldsymbol{\sigma}^t d\,\Omega^t = R^{ext\,t+\triangle t} - \int_{\Omega^t} \delta\mathbf{e} : \boldsymbol{\sigma}^t d\,\Omega^t \tag{2.6}$$

In the above equation, $\triangle\mathbf{S} = \mathbf{S}_t^{t+\triangle t} - \boldsymbol{\sigma}^t$ is the increment of second Piola-Kirchhoff stress, $\triangle\mathbf{E} = \mathbf{E}_t^{t+\triangle t} - \mathbf{E}_t^t$ is the increment of Green-Lagrange strain. Furthermore, $\mathbf{e}$ and $\boldsymbol{\eta}$ are respectively the linear and non-linear parts of $\triangle\mathbf{E}$, expressed as:

$$\mathbf{e} = \frac{1}{2}\left[\left(\frac{\partial\triangle\mathbf{u}}{\partial\mathbf{x}^t}\right)^T + \frac{\partial\triangle\mathbf{u}}{\partial\mathbf{x}^t}\right] \quad \text{and} \quad \boldsymbol{\eta} = \frac{1}{2}\left(\frac{\partial\triangle\mathbf{u}}{\partial\mathbf{x}^t}\right)^T \frac{\partial\triangle\mathbf{u}}{\partial\mathbf{x}^t} \tag{2.7}$$

The nonlinear equation (2.6) is solved using an iterative method such as the Newton-Raphson solver. A linearized form of equation (2.6) is required to set up the tangent matrix. Employing an incremental constitutive law of the form $\triangle\mathbf{S} = \mathbf{C}^t : \mathbf{e}$ and using approximation $\delta\triangle\mathbf{E} = \delta\mathbf{e}$, the linearized equation to be solved becomes

$$\int_{\Omega^t} \delta\mathbf{e} : \mathbf{C}^t : \mathbf{e} d\Omega^t + \int_{\Omega^t} \delta\boldsymbol{\eta} : \boldsymbol{\sigma}^t d\Omega^t = R^{ext\,t+\triangle t} - \int_{\Omega^t} \delta\mathbf{e} : \boldsymbol{\sigma}^t\, d\Omega^t \tag{2.8}$$

where $\mathbf{C}^t$ is the history-dependent fourth-order tangent stiffness tensor at time t, which is derived from the specific crystal plasticity constitutive model in the following sections.

2.2 Crystal Plasticity Constitutive Relations for Mg alloys

Mg alloys, e.g. the wrought alloy AZ31, possess low-symmetry hexagonal closed packed (*hcp*) crystallographic structure, consisting of 5 different families of slip systems, namely the basal $\langle a \rangle$, prismatic $\langle a \rangle$, pyramidal $\langle a \rangle$, first order pyramidal $\langle c+a \rangle$ and second order pyramidal $\langle c+a \rangle$ with a total of 30 slip systems. Pronounced differences are found in the critical resolved shear stresses and strain-hardening rates in the different slip systems, causing high anisotropy in mechanical properties. Experimental observations for Mg alloys e.g. in [61] have indicated that only 12 slip systems are active while others like the first-order pyramidal slip system tend to dissociate and are rarely active in dislocation glide [62]. Consequently for efficiency, the present model considers 3 basal slip modes $(0001)\left\langle 11\bar{2}0\right\rangle$, 3 prismatic slip modes $\{10\bar{1}0\}\left\langle 11\bar{2}0\right\rangle$ and 6 second-order pyramidal $\langle c+a \rangle$ slip modes $\{11\bar{2}2\}\left\langle 11\bar{2}3\right\rangle$ in 12 slip systems [30, 63]. A schematic of the slip and twin systems in the *hcp* magnesium alloys is shown in figure 2.1. The crystal plasticity constitutive model is adapted from the size and time dependent, finite strain models that have been developed for Ti alloys in [52–57]. It's flow rule is enhanced by more physics-based thermally activated obstacle to slip and athermal obstacles, which correspond to the passing and cutting shear resistance respectively [59]. The crystal plasticity model accounts for microstructural features such as hardening due to statistically stored dislocation and geometrically necessary dislocation densities.

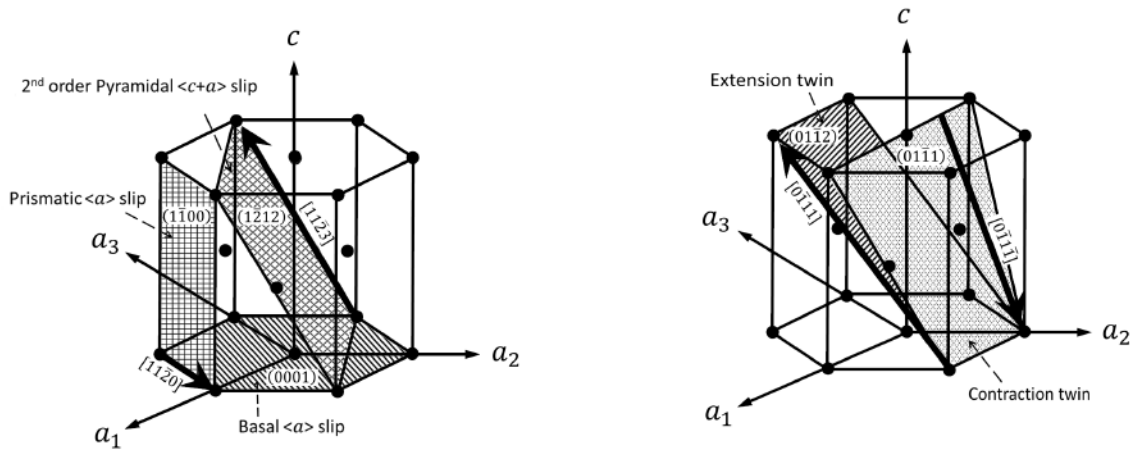

(a) (b)

Figure 2.1: Schematic showing: (a) active slip systems and (b) twin systems in *hcp* magnesium alloys.

2.2.1 Kinematic relations and flow rule

The deformation gradient $\mathbf{F}_0^t = \frac{\partial \mathbf{x}^t}{\partial \mathbf{x}^0}$ at time t with respect to the initial reference configuration at $t = 0$, is multiplicatively decomposed into elastic and plastic components as:

$$\mathbf{F}_0^t = \mathbf{F}^e \mathbf{F}^p \tag{2.9}$$

where $\mathbf{F}^e$ is its elastic component that describes stretching and rotation of the crystal lattice, and $\mathbf{F}^p$ is its incompressible plastic component, i.e. $\det \mathbf{F}^p = 1$. The decomposition admits an anholonomic unstressed intermediate configuration B_i associated with the population and motion of crystal defects, for which $\mathbf{F}^e$ is associated with the driving stress that

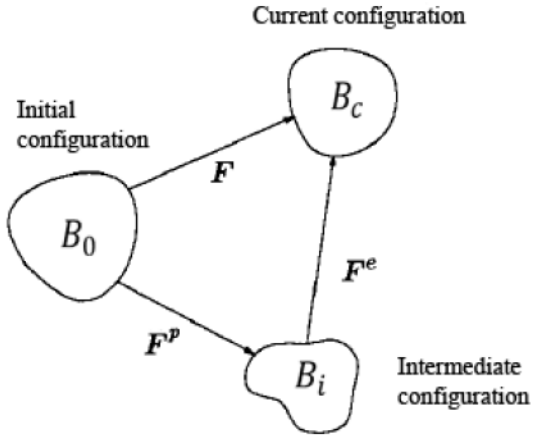

Figure 2.2: Multiplicative decomposition of the deformation gradient.

brings B_i to the current configuration B_c, as shown in figure 2.2. The stress-strain constitutive equation in the reference configuration is written in terms of the second Piola-Kirchoff stress tensor $\mathbf{S}$ and its work-conjugate Lagrange-Green strain tensor $\mathbf{E}^e$ as:

$$\mathbf{S} = \mathbf{C} : \mathbf{E}^e \quad \text{where} \quad \mathbf{E}^e = \frac{1}{2}(\mathbf{F}^{eT}\mathbf{F}^e - \mathbf{I}) \tag{2.10}$$

where $\mathbf{C}$ is a fourth order anisotropic elasticity tensor. Plastic deformation of magnesium alloys at moderate strain-rates is predominantly caused by dislocation glide on selected slip systems and micro-twin evolution. The flow rule , governing evolution of plastic deformation due to dislocations, is expressed in terms of the plastic velocity gradient $\mathbf{L}^p$ as:

$$\mathbf{L}^p = \dot{\mathbf{F}}^p\mathbf{F}^{\mathbf{p}-1} = \sum_{\alpha}^{nslip} \dot{\gamma}^\alpha \mathbf{s}_0^\alpha \tag{2.11}$$

where $\dot{\gamma}^\alpha$ is the slip rate on the α slip system and $nslip$ is the total number of active slip

systems. The Schmid tensor associated with α-th slip system $\mathbf{s}_0^\alpha$ is expressed in terms of the slip direction $\mathbf{m}_0^\alpha$ and slip plane normal $\mathbf{n}_0^\alpha$ in the unrotated reference configuration B_i as $\mathbf{s_0^\alpha} = \mathbf{m}_0^\alpha \otimes \mathbf{n}_0^\alpha$. Combining the models in [56, 57] and [59] the plastic slip rate $\dot{\gamma}^\alpha$ on the α-th slip system has a power law dependence on the resolved shear stress τ^α from the far-field stress, and the slip system deformation resistances overcoming the local thermal and athermal barriers. This can be expressed as:

$$\dot{\gamma} = \dot{\gamma}_0^\alpha \left| \frac{\tau^\alpha - s_a^\alpha}{s_*^\alpha} \right|^{\frac{1}{m}} sign(\tau^\alpha - s_a^\alpha) \tag{2.12}$$

Here, the temperature-dependent critical shear resistance s^α is assumed to be comprised of a thermally activated obstacle to slip s_*^α and a part due to the athermal obstacles s_a^α. The athermal resistance arises from the long-range internal stress field between parallel dislocation lines or from grain boundaries, while the thermal shear resistance is due to local obstacles caused by particles, dislocation jogs or forest dislocations. s_a^α and s_*^α correspond to the passing and cutting stress barriers respectively, with the driving force for dislocation motion on the slip system being the difference between the resolved shear stress and athermal shear resistance. The term $\tau^\alpha - s_a^\alpha$ is the local effective driving force applied on a dislocation line. The resolved shear stress on a slip system τ^α is derived as:

$$\tau^\alpha = (\mathbf{F}^{eT}\mathbf{F}^e\mathbf{S}) : (\mathbf{s_0^\alpha}) \tag{2.13}$$

The exponent m corresponds to the strain-rate sensitivity, $\dot{\gamma}_0^\alpha$ is the reference slip rate for α

system.

The power law model of equation (2.12) is the consistent with the activation energy based model [64] of the form:

$$\dot{\gamma} = \dot{\gamma}_0^\alpha \exp\left\{-\frac{1}{k_B T}\triangle F_* \left[1 - \left(\frac{|\tau^\alpha - s_a^\alpha|}{s_*^\alpha}\right)^p\right]^q\right\} \; sign(\tau^\alpha - s_a^\alpha) \tag{2.14}$$

where parameters p and q correspond to the shape of local obstacles and $\triangle F_*$ is the thermal activation energy. For cuboidal shapes of local barriers, $p = q = 1$. Moreover, for moderate rates of plastic deformation regime the factor $\frac{(\tau^\alpha - s_a^\alpha)}{s_*^\alpha}$ is of the order $O(1)$, for which the exponential term $\exp\left(\frac{|\tau^\alpha - s_a^\alpha|}{s_*^\alpha} - 1\right)$ can be expanded in a series while retaining only the linear term $\frac{|\tau^\alpha - s_a^\alpha|}{s_*^\alpha}$. Correspondingly, the exponent in equation (2.12) may be equated as $\frac{1}{m} = \frac{\triangle F_*}{k_B T}$, which for magnesium and its alloys has a value typically larger than 30 [65]. In the present work, an isothermal assumption is made, for which the value of the power-law exponent $\frac{1}{m}$ is constant.

2.2.2 Evolution of slip system resistance

The evolution of shear resistance on individual slip systems is governed by two types of dislocations, viz. statistically stored dislocations (SSDs) and geometrically necessary dislocations (GNDs) [57, 66, 67]. The accommodation of SSDs, which correspond to homogeneous plastic deformation that is characterized by vanishing net Burgers vector, is the result of random trapping and multiplication process in chance encounters. The

existence of GNDs corresponds to the storage of polarized dislocation densities, necessary to accommodate the crystal lattice curvature such as in single crystal bending or near polycrystalline grain boundaries. Phenomenological hardening laws, proposed in [59], are assumed for the evolution of thermal and athermal shear resistances contributing to the overall shear resistance. The thermal shear resistance s_*^α accounts for the effect of forest dislocations normal to α slip plane, while the athermal shear resistance s_a^α reflects the effect of parallel dislocations in the slip direction $\mathbf{m}^\alpha$. They are constituted of three components, viz. the initial shear resistance and contributions due to the evolution of the SSDs and GNDs respectively, i.e. $s_{a/*}^\alpha = s_{a/*,0}^\alpha + s_{a/*,SSD}^\alpha + s_{a/*,GND}^\alpha$. For SSDs, the rate of evolution of these resistances is expressed as:

$$\dot{s}_{a,SSD}^\alpha = \sum_{\beta=1}^{N} h_a^{\alpha\beta} \left| \dot{\gamma}^\beta \sin\left(\mathbf{n}^\alpha, \boldsymbol{t}^\beta\right) \right| \tag{2.15a}$$

$$\dot{s}_{*,SSD}^\alpha = \sum_{\beta=1}^{N} h_*^{\alpha\beta} \left| \dot{\gamma}^\beta \cos\left(\mathbf{n}^\alpha, \boldsymbol{t}^\beta\right) \right| \tag{2.15b}$$

where $\boldsymbol{n}^\alpha$ is the normal to the slip system plane α and $\boldsymbol{t}^\beta$ is the dislocation line tangent vector for edge dislocation on the slip plane β. It is derived as the cross product of the slip direction and slip plane normal, i.e. $\boldsymbol{t}^\beta = \mathbf{m}^\beta \times \mathbf{n}^\beta$. Equation (2.15a) corresponds to the projection of β slip system dislocations parallel to the α slip plane, while equation (2.15b) projects them on a plane normal to α slip plane. In this work, SSDs due to edge dislocations are considered only [59, 67]. To incorporate the contribution of screw dislocations in SSDs

e.g. in [68] for $Ti6Al4V$ alloys, the direction of the dislocation line tangent vector should be $\mathbf{m}^\beta$, and the projection relations in equations (2.15) should additionally incorporate the projection angle corresponding to $\left(\mathbf{n}^\alpha, \mathbf{m}^\beta\right)$. Moduli $h_*^{\alpha\beta}$ and $h_a^{\alpha\beta}$ describe strain hardening rate due to both self and latent hardening on the slip system α due to slip on the slip system β. The hardening moduli for athermal and thermal shear resistances are assumed to be identical in this work, i.e.

$$h_a^{\alpha\beta} = h_*^{\alpha\beta} = q^{\alpha\beta} h^\beta, \quad (no\ sum\ on\ \beta) \tag{2.16}$$

Here h^β is the self-hardening coefficient on the slip system β and $q^{\alpha\beta}$ is a matrix describing latent hardening. The evolution of self hardening rate is expressed as:

$$h^\beta = h_{ref}^\beta \left| 1 - \frac{s^\beta}{s_{sat}^\beta} \right|^r \ sign\left(1 - \frac{s^\beta}{s_{sat}^\beta}\right) \tag{2.17}$$

where the exponent r is a material constant and s_{sat}^β is the reference value of saturation stress on β slip system. The magnitude of the total shear resistance is given as $s^\beta = \sqrt{(s_a^\beta)^2 + (s_*^\beta)^2}$.

The consideration of hardening due to geometrically necessary dislocations or GNDs is important for hcp crystals that exhibit anisotropy due to a high degree of heterogeneity between different slip systems. Grains with different orientations have significant differences in response under loading that result in lattice curvatures and accumulation of GNDs at grain

boundaries. They are necessary for providing additional stresses to maintain compatibility at grain boundaries. The components of GNDs may be derived from the Nye's dislocation density tensor $\mathbf{\Lambda}$, which measures the incompatibility in the intermediate configuration and is expressed as [69]:

$$\mathbf{\Lambda} = -(\nabla_X \times \mathbf{F}^{p^T})^T \tag{2.18}$$

where ∇_X is the gradient operator with respect to the reference coordinates. Both edge and screw components of GNDs contribute to $\mathbf{\Lambda}$ in the incompatible intermediate configuration [67]. Thus the GNDs on each slip system are decomposed into three groups, viz. one group of screw components $\rho^{\alpha}_{GND,s}$ with their line tangent vector parallel to the slip direction $\mathbf{m}^{\alpha}$, and two groups of edge components $\rho^{\alpha}_{GND,en}$ and $\rho^{\alpha}_{GND,et}$ with their respective line tangent vectors parallel to slip plane normal $\mathbf{n}^{\alpha}$ and $\boldsymbol{t}^{\alpha} = \mathbf{m}^{\alpha} \times \mathbf{n}^{\alpha}$. This may be written as:

$$\mathbf{\Lambda} = \sum_{\alpha=1}^{nslip} \rho^{\alpha}_{GND,s} \mathbf{b}^{\alpha} \otimes \mathbf{m}^{\alpha} + \rho^{\alpha}_{GND,et} \mathbf{b}^{\alpha} \otimes \mathbf{t}^{\alpha} + \rho^{\alpha}_{GND,en} \mathbf{b}^{\alpha} \otimes \mathbf{n}^{\alpha} \tag{2.19}$$

where $nslip = 12$, and $\mathbf{b}^{\alpha}$ is the Burgers vector on the slip system α. Equations (2.18) and (2.19) constitute an under-constrained problem, in which 36 independent components of ρ^{α}_{GND}, viz. 12 $\rho^{\alpha}_{GND,s}$, 12 $\rho^{\alpha}_{GND,et}$ and 12 $\rho^{\alpha}_{GND_en}$ need to be solved from 9 equations. Equation (2.19) may be written in a matrix form as:

$$\left\{\hat{\mathbf{\Lambda}}\right\} = [\mathbf{A}] \left\{\boldsymbol{\rho}_{GND}\right\} \tag{2.20}$$

where $\{\hat{\mathbf{\Lambda}}\}$ is 9×1 vector form of the Nye's dislocation density tensor $\mathbf{\Lambda}$, $[\mathbf{A}]$ is a 9×36 linear operator matrix containing the basis tensors $\mathbf{b}^\alpha \otimes \mathbf{m}^\alpha$, $\mathbf{b}^\alpha \otimes \mathbf{t}^\alpha$ and $\mathbf{b}^\alpha \otimes \mathbf{n}^\alpha$, and $\{\boldsymbol{\rho}_{GND}\}$ is the 36×1 vector column of GND components. Equation (2.20) yields an under-determined system of linear equations that has an infinite solutions, if any. Consequently, following discussions in [70], a minimization problem is solved for the L_2 norm of the GND density (see below) subject to the constraints of equation (2.20). The L_2 norm is expressed as the sum of the squares of GND densities on each slip system as:

$$\{\boldsymbol{\rho}_{GND}\}^T\{\boldsymbol{\rho}_{GND}\} = \sum_\alpha \left(\rho^\alpha_{GND,s}\right)^2 + \left(\rho^\alpha_{GND,et}\right)^2 + \left(\rho^\alpha_{GND,en}\right)^2 = \sum_\alpha \left(\rho^\alpha_{GND}\right)^2 \tag{2.21}$$

Geometric constraints posed in equation (2.20) allows only certain dislocations to exist on the slip planes, which is taken into account by minimizing the functional of the form:

$$\mathcal{F}\left(\{\boldsymbol{\rho}_{GND}\},\{\boldsymbol{\lambda}\}\right) = \left\{\{\boldsymbol{\rho}_{GND}\}^T\{\boldsymbol{\rho}_{GND}\} + \{\boldsymbol{\lambda}\}^T\left([\mathbf{A}]\{\boldsymbol{\rho}_{GND}\} - \{\hat{\mathbf{\Lambda}}\}\right)\right\} \tag{2.22}$$

Here $\{\boldsymbol{\lambda}\}$ is a 9×1 column vector containing components of the Lagrange multipliers. The stationarity conditions $\frac{\partial\mathcal{F}}{\partial\{\boldsymbol{\rho}_{GND}\}} = 0$ and $\frac{\partial\mathcal{F}}{\partial\{\boldsymbol{\lambda}\}} = 0$ yield the equation to be solved:

$$\{\boldsymbol{\rho}_{GND}\} = [\mathbf{A}]^T([\mathbf{A}][\mathbf{A}]^T)^{-1}\{\hat{\mathbf{\Lambda}}\} \tag{2.23}$$

The GNDs contribute to slip system resistance through increase in the long-range passing stress due to the interaction of mobile dislocations with parallel dislocations, as well as

increase in cutting stress due to mobile dislocations cutting the forest dislocations perpendicular to the slip plane. Parallel and forest dislocation densities due to the GNDs may be expressed in terms of the components as [67]:

$$\rho^{\alpha}_{GND,P} = \sum_{\beta=1}^{nslip} \chi^{\alpha\beta} \left[\rho^{\beta}_{GND,s} \left| \sin(\boldsymbol{n}^{\alpha}, \boldsymbol{m}^{\beta}) \right| + \rho^{\beta}_{GND,et} \left| \sin(\boldsymbol{n}^{\alpha}, \boldsymbol{t}^{\beta}) \right| + \rho^{\beta}_{GND,en} \left| \sin(\boldsymbol{n}^{\alpha}, \boldsymbol{n}^{\beta}) \right| \right] \tag{2.24a}$$

$$\rho^{\alpha}_{GND,F} = \sum_{\beta=1}^{nslip} \chi^{\alpha\beta} \left[\rho^{\beta}_{GND,s} \left| \cos(\boldsymbol{n}^{\alpha}, \boldsymbol{m}^{\beta}) \right| + \rho^{\beta}_{GND,et} \left| \cos(\boldsymbol{n}^{\alpha}, \boldsymbol{t}^{\beta}) \right| + \rho^{\beta}_{GND,en} \left| \cos(\boldsymbol{n}^{\alpha}, \boldsymbol{n}^{\beta}) \right| \right] \tag{2.24b}$$

The coefficient $\chi^{\alpha\beta}$ describes the strengthening effect due to the interaction between α slip system and β slip system, e.g. in the formation of dislocation locks. For *hcp* crystals $\chi^{\alpha\beta}$ is taken as 1 in this work. As noted in [67], equation (2.24) uses the absolute value of GND density without accounting for the sign of Burgers vector, which may result in a loss of the kinematic hardening due to GNDs. The athermal and thermal shear resistances from GND hardening at time t are expressed as:

$$s^{\alpha}_{a,GND} = c_1 G b^{\alpha} \sqrt{\rho^{\alpha}_{GND,P}} \quad \text{and} \quad s^{\alpha}_{*,GND} = \frac{Q^{\alpha}_{slip}}{c_2 c_3 b^{\alpha 2}} \sqrt{\rho^{\alpha}_{GND,F}} \tag{2.25}$$

where the athermal shear resistance is from the long-range internal stress field between

mobile dislocation lines on α slip system and parallel GNDs and the thermal shear resistance arises from mobile dislocation cutting forest GNDs. Here G is the shear modulus, c_1 is a constant for passing stress, c_2 is a constant for jump width, c_3 is a constant for obstacle width, b^α is the magnitude of Burgers vector for α slip system and Q^α_{slip} is the effective activation energy for dislocation slip. In this work, an approximation that $Q^\alpha_{slip} = 10Gb^{\alpha^3}$ is made for hcp crystals. Adding all contributions, the thermal and athermal shear resistance with both SSD and GND hardening at time t are expressed as:

$$s^\alpha_a = s^\alpha_{a,0} + \int_{t'=0}^{t'=t} \sum_{\beta=1}^{nslip} h^{\alpha\beta} \left| \dot{\gamma}^\beta \sin(\boldsymbol{n}^\alpha, \boldsymbol{t}^\beta) \right| \, dt' + c_1 G b^\alpha \sqrt{\rho^\alpha_{GND,P}} \tag{2.26a}$$

$$s^\alpha_* = s^\alpha_{*,0} + \int_{t'=0}^{t'=t} \sum_{\beta=1}^{nslip} h^{\alpha\beta} \left| \dot{\gamma}^\beta \cos(\boldsymbol{n}^\alpha, \boldsymbol{t}^\beta) \right| \, dt' + \frac{Q^\alpha_{slip}}{c_2 c_3 b^{\alpha^2}} \sqrt{\rho^\alpha_{GND,F}} \tag{2.26b}$$

The first terms corresponds to the initial shear resistance and the second terms are derived from the time integration of equations (2.15a) and (2.15b) for the rate of shear resistance due to SSDs.

It has been discussed in [54] that the initial slip system resistance in a polycrystalline aggregate depends on the grain size. The grain boundary acts as dislocation barrier and reduce the dislocation glide mean free path, which in turn contributes to the hardness through increased initial slip system shear resistance. A Hall-Petch type relation has been implemented in [54] to augment the initial thermal shear resistance in (2.26) as:

$$\hat{s}^\alpha_{*,0} = s^\alpha_{*,0} + \frac{K^\alpha}{\sqrt{D_g}} \tag{2.27}$$

where D_g is the equivalent grain diameter and $K^\alpha = \sqrt{\frac{(2-\nu)\pi\tau^* G b^\alpha}{2(1-\nu)}}$. Here ν is the PoissonâĂŹs ratio, G is the shear modulus, b^α is the Burgers vector and τ^* is the barrier strength for the grain boundary, which is taken as $\tau^* = 0.01G$.

2.2.3 Evaluation of the tangent stiffness matrix

In this section, the tangent stiffness tensor $\mathbf{C}^t$ in equation (2.8) is derived from the crystal plasticity constitutive model. $\mathbf{C}^t$ at time t is expressed as:

$$\mathbf{C}^t = \frac{1}{det\mathbf{F}_0^t}\left(\mathbf{F}_0^t \otimes \mathbf{F}_0^t\right) : \mathbf{C}^0 : \left(\mathbf{F}_0^t \otimes \mathbf{F}_0^t\right) \tag{2.28}$$

where $\mathbf{C}^0$ has been derived in [71] as:

$$\begin{aligned} \mathbf{C}^0 &= \frac{\partial \mathbf{S}_0^t}{\partial \mathbf{E}_0^t} = (det\mathbf{F}^p)\left(\mathbf{F}^p \underline{\otimes} \mathbf{F}^p\right)^{-1} \\ &: \left\{\frac{\partial \mathbf{S}^*}{\partial \mathbf{E}} + \left[\mathbf{S}^* \otimes \mathbf{F}^{p^{-T}} - (det\mathbf{F}^p)^{-1}\left[\mathbf{I} \underline{\otimes} \left(\mathbf{S}\mathbf{F}^{p^T}\right)^T + (\mathbf{F}^p\mathbf{S}) \bar{\otimes} \mathbf{I}\right]\right] : \frac{\partial \mathbf{F}^p}{\partial \mathbf{E}}\right\} \end{aligned} \tag{2.29}$$

with

$$\mathbf{S}^* = (det\mathbf{F}^p)^{-1}\mathbf{F}^p\mathbf{S}\mathbf{F}^{p^T} \tag{2.30a}$$

$$\frac{\partial \mathbf{S}^*}{\partial \mathbf{E}} = \left[\mathbf{I}\underline{\otimes}\mathbf{I} + \sum_{\alpha}^{Nslip}\left(C^\alpha \otimes \frac{\partial \triangle\gamma^\alpha}{\partial \mathbf{S}^*}\right)\right]^{-1}\left[\mathbf{A}^\alpha - \sum_{\alpha}^{Nslip}\triangle\gamma^\alpha\mathbf{B}^\alpha\right] \tag{2.30b}$$

$$\mathbf{A} = \mathbf{C}^e : \left(\mathbf{F}^{p^{-1}}\underline{\otimes}\mathbf{F}^{p^{-1}}\right) \tag{2.30c}$$

$$\mathbf{B}^\alpha = \mathbf{C}^e : \left[\mathbf{F}^{p^{-T}}\underline{\otimes}\left(\mathbf{F}^{p^{-1}}\mathbf{s}_0^\alpha\right)^T + \left(\mathbf{F}^{p^{-1}}\mathbf{s}_0^\alpha\right)^T\underline{\otimes}\mathbf{F}^{p^{-T}}\right] \tag{2.30d}$$

$$\frac{\partial \mathbf{F}^p}{\partial \mathbf{E}} = \sum_{\alpha}^{Nslip}\left(\mathbf{s}_0^\alpha\mathbf{F}^p\right)\otimes\left(\frac{\partial \triangle\gamma^\alpha}{\partial \mathbf{S}^*}\frac{\partial \mathbf{S}^*}{\partial \mathbf{E}}\right) \tag{2.30e}$$

The lower and upper tensor product operators $\underline{\otimes}$ and $\bar{\otimes}$ are defined as $\left(A\underline{\otimes}B\right)_{ijkl} = A_{ik}B_{jl}$ and $(A\bar{\otimes}B)_{ijkl} = A_{il}B_{jk}$. $\mathbf{C}^t$ is a function of path-dependent state variables, i.e. $\mathbf{C}^t = \mathbf{C}^t\left(\mathbf{F}^t, \mathbf{F}^{pt}, \dot{\gamma}^t, ...\right)$. The time-integration algorithm developed in chapter 2 is implemented here to incrementally update state variables. The fourth order tensor $\mathbf{C}^t$ is written as a 6×6 matrix, using the property of major symmetry, for implementation to finite element weak form.

2.3 Numerical Implementation of Crystal Plasticity Constitutive Model

The non-local rate-dependent crystal plasticity equations in section 2.2 are implemented in a crystal plasticity FE (CPFE) code, using an implicit time-integration scheme. The implicit scheme implements a two-step, staggered iterative approach using the backward

Euler time integration methods. In the first step, local stress components, deformation and state variables, e.g. $\mathbf{F}^p$, $\dot{s}^{\alpha}_{a,SSD}$ and $\dot{s}^{\alpha}_{*,SSD}$, are integrated from time t to time $t + \Delta t$ with a fixed GND density $\boldsymbol{\rho}_{GND}$ at each integration point using an iterative Newton-Raphson solver. In the second step the GND density $\boldsymbol{\rho}_{GND}$ is updated by solving the non-local equations (2.18), (2.19) and (2.20) in the neighborhood of each integration point. Upon achieving convergence in the two-step iteration process, the Cauchy stress σ_{ij} and elasto-plastic tangent stiffness matrix $C^{ep}_{ijkl} = \partial\sigma_{ij}/\partial\varepsilon_{kl}$ are computed and passed on to the equilibrium problem solver.

2.3.1 Time integration algorithm for integrating crystal plasticity constitutive equations

An implicit time integration algorithm is developed following the steps developed in [52]. In an increment from t to $t + \Delta t$, the algorithm seeks the solution of six nonlinear algebraic equations corresponding to the number of second Piola-Kirchoff stress components. With known values of deformation variables at time t, viz. $\mathbf{F}(t)$, $\mathbf{F}^p(t)$, $s^{\alpha}_a(t)$, $s^{\alpha}_*(t)$, as well as a prescribed deformation gradient $\mathbf{F}(t + \Delta t)$ at time $t + \Delta t$, the algorithm updates stresses, plastic strains and all deformation state variables, with the GND density and its rate of hardening held fixed. After convergence is reached in this step, the GNDs are updated and the procedure is repeated. Integrating equation (2.11) as:

$$\mathbf{F}^p(t + \Delta t) = \left(\mathbf{I} + \sum_{\alpha=1}^{nslip} \Delta\gamma^{\alpha}\mathbf{s}^{\alpha}_0\right)\mathbf{F}^p(t) \tag{2.31}$$

and substituting in equations (2.9) and (2.10), yields the nonlinear equations for the updated second Piola-Kirchoff stress:

$$\mathbf{S}(t+\triangle t) = \mathbf{S}^{tr} - \sum_{\alpha=1}^{nslip} \triangle\gamma^{\alpha}\left(\mathbf{S}(t+\triangle t), s_a^{\alpha}(t+\triangle t), s_*^{\alpha}(t+\triangle t)\right)\mathbf{B}^{\alpha} \tag{2.32}$$

where

$$\mathbf{A}(t+\triangle t) = \mathbf{F}^{p^{-T}}(t)\mathbf{F}^{T}(t+\triangle t)\mathbf{F}(t+\triangle t)\mathbf{F}^{p^{-1}}(t) \tag{2.33a}$$

$$\mathbf{B}^{\alpha} = \mathbf{C} : \left[\frac{1}{2}\left(\mathbf{A}(t+\triangle t)\mathbf{s}_0^{\alpha} + \mathbf{s}_0^{\alpha}\mathbf{A}(t+\triangle t)\right)\right] \tag{2.33b}$$

$\mathbf{S}^{tr}$ is the trial stress and is expressed as:

$$\mathbf{S}^{tr} = \mathbf{C} : \frac{1}{2}\left(\mathbf{A}(t+\triangle t) - \mathbf{I}\right) \tag{2.34}$$

The nonlinear equation (2.32) is solved using Newton-Raphson iterative solver. For the $i-th$ iteration the update in the second Piola-Kirchoff stress is obtained as:

$$\mathbf{S}^{i+1}(t+\triangle t) = \mathbf{S}^{i}(t+\triangle t) - \left.\frac{\partial \mathbf{G}}{\partial \mathbf{S}}\right|_{i}^{-1} \mathbf{G}(\mathbf{S}^{i}(t+\triangle t)) \tag{2.35}$$

where $\mathbf{G}\left(\mathbf{S}^{i}(t+\triangle t)\right)$ is the residual defined from equation (2.32) as:

$$\mathbf{G}(\mathbf{S}^i(t+\triangle t)) = \mathbf{S}^i(t+\triangle t) - \mathbf{S}^{tr} + \sum_{\alpha=1} \triangle\gamma^\alpha \mathbf{B}^\alpha \tag{2.36}$$

The Jacobian matrix is:

$$\frac{\partial \mathbf{G}}{\partial \mathbf{S}^i} = \mathbf{I} + \sum_{\alpha}^{nslip} \mathbf{B}^\alpha \otimes \frac{\partial \triangle\gamma^\alpha}{\partial \mathbf{S}^i} \tag{2.37}$$

for which an analytical expression can be derived from equation (2.12). In this step of updating $\mathbf{S}(t+\triangle t)$ and the increment of slip system resistance from SSDs ($\dot{s}^\alpha_{a,SSD}$ and $\dot{s}^\alpha_{*,SSD}$) the slip system resistance component from GNDs are held fixed.

2.3.2 Updating GNDs and related variables

The GNDs and associated variables are updated after reaching convergence in the solution of equation (2.35). In the hardening-based CPFE framework, in which GNDs are not explicit variables, the GND density $\boldsymbol{\rho}_{GND}$ is evaluated from the Nye's dislocation density tensor $\boldsymbol{\Lambda}$ using equation (2.23). $\boldsymbol{\Lambda}$ has been defined in equation (2.18).

Numerical evaluation of $\boldsymbol{\Lambda}$ requires computing the derivatives of the plastic deformation gradient at each integration point of an element. The derivatives may be numerically determined at a given point in the interior of an element, from nodal values of the variable, using element shape functions as:

$$\frac{\partial \hat{F}^p_{ij}}{\partial x_k} = \sum_{\alpha=1}^{Nnode} (\hat{F}^p)^\alpha_{ij} \frac{\partial N_\alpha}{\partial x_k} \tag{2.38}$$

Here $(\hat{F}^p)^\alpha_{ij}$ are components of the nodal values of the plastic deformation gradient and

N_α are the element shape functions. This requires the values of $(\hat{F}^p)^\alpha_{ij}$ at the nodal points that should be determined from those element integration point. The super-convergent patch recovery (SPR) method in [72] is deemed to be the most appropriate method for this purpose. The SPR method evaluates nodal values within a super-convergent patch $\mathbf{\Omega}_p$ by interpolating the variables using a higher order (p) polynomial expansion within the patch, expressed as:

$$\tilde{F}(\mathbf{x})^p_{ij} = [\mathbf{P}(\mathbf{x})]\,\{\mathbf{a}\}^{ij} \tag{2.39}$$

where $\tilde{F}(\mathbf{x})^p_{ij}$ represents higher order representations of plastic deformation gradient tensor components at a point $\mathbf{x}$ in the patch, $[\mathbf{P}(\mathbf{x})]$ is the interpolation matrix constituted of polynomial basis functions, e.g.:

$$[\mathbf{P}(\mathbf{x})] = \{1, x, y, z, x^2, y^2, z^2, xy, yz, zx, \ldots\}$$

and $\{\mathbf{a}\}^{ij}$ is the coefficient vector. A second order polynomial is used for the $\mathbf{F}^p$ field in this work. The coefficient vector is obtained by least-squares minimization of the difference between the function in equation (2.39) and known FEM solution F^p_{ij} at element integration points within the patch. The function to be minimized with respect to $\{\mathbf{a}\}^{ij}$ is:

$$f(\{\mathbf{a}\}^{ij}) = \sum_{IP=1}^{N_{IP}} \left(F^p_{ij}(x, y, z) - [\mathbf{P}(x, y, z)]\,\{\mathbf{a}\}^{ij}\right)^2_{IP} \tag{2.40}$$

where N_{IP} is the number of integration points. The minimizing solution is given in [72] as:

$$\{\mathbf{a}\}^{ij} = [\mathbf{X}]^{-1} \{\mathbf{y}\}^{ij} \tag{2.41}$$

where

$$\begin{aligned} [\mathbf{X}] &= \sum_{IP=1}^{N_{IP}} [\mathbf{P}(x,y,z)]_{IP}^{T} [\mathbf{P}(x,y,z)]_{IP} \quad \text{and} \\ \{\mathbf{y}\}^{ij} &= \sum_{IP=1}^{N_{IP}} [\mathbf{P}(x,y,z)]_{IP}^{T} F_{ij}^{p}(x,y,z)_{IP} \end{aligned} \tag{2.42}$$

The nodal values of each component F_{ij}^{p} can be evaluated using equation (2.39). The super-convergent patches can be defined separately for each grain by selecting the appropriate surrounding elements. The selection of this patch is important to avoid the ill-conditioning of the [**X**] matrix because of the higher powers. Typically normalized coordinates are used in the construction of $[\mathbf{P}(x,y,z)]$ [72] as:

$$\bar{x} = -1 + 2\frac{x - x_{min}}{x_{max} - x_{min}}, \quad \bar{y} = -1 + 2\frac{y - y_{min}}{y_{max} - y_{min}}, \quad \bar{z} = -1 + 2\frac{z - z_{min}}{z_{max} - z_{min}} \tag{2.43}$$

where subscripts *max* and *min* correspond to the maximum and minimum coordinates in the patch. The normalized nodal coordinates lie within the bounds $1 \leq \bar{x} \leq 1$, $-1 \leq \bar{y} \leq 1$, and $-1 \leq \bar{z} \leq 1$ for nodes within a grain. A weighted least-square method is used in this work that can be used with large patches without discrimination. In this method, a weighting function that decays with the distance from the node from which the patch is

being set up is used. The minimizer function in (2.40) is correspondingly modified as:

$$f(\{\mathbf{a}\}^{ij}) = \sum_{IP=1}^{N_{IP}} w_{IP} \left(F_{ij}^{p}(x,y,z) - [\mathbf{P}(x,y,z)] \{\mathbf{a}\}^{ij} \right)_{IP}^{2} \tag{2.44}$$

where an exponentially decaying weight is chosen as $w_{IP} = exp(-\alpha l)$, with l being the distance from the integration point to the target node in question and α being a constant taken as 1.5 in this work.

Finally components of the Nye's dislocation density tensor in equation (2.18) at a point in an element are evaluated as:

$$\Lambda_{ij} = \epsilon_{jrs} \frac{\partial F_{is}^{p}}{\partial X_r} = \epsilon_{jrs} \sum_{\alpha=1}^{Nnode} \frac{\partial N_\alpha}{\partial X_r} (\hat{F}^{p})_{ij}^{\alpha} \tag{2.45}$$

where ϵ_{irs} is the permutation tensor.

The sequence of computational operations in the crystal plasticity constitutive update procedure is provided in table 2.1.

2.4 Conclusion

This chapter develops a physics-based crystal plasticity FE model of dislocation-dominated heterogeneous deformation. The constitutive model for crystallographic slip incorporates

Table 2.1: Flowchart of computational operations in constitutive update procedure

Step **A**	Update local stress and deformation variables from t to $t+\Delta t$, with known $\mathbf{F}(t+\Delta t)$ and other variables at time t
i	Calculate trial second Piola-Kirchhoff stress $\mathbf{S}^{tr}$ and slip-system RSS $\tau^{\alpha^{tr}}$ using equations (2.32) and (2.13); subsequently update slip rates and deformation variables using equations (2.14) and (2.15)
ii	Obtain the starting iterate $\mathbf{S}^{I}(t+\Delta t)$ from equation (2.32)
iii	For the i-th iteration step in the Newton-Raphson algorithm:
	(a) Evaluate $\tau^{\alpha^{i}} = \mathbf{S}^{i}(t+\Delta t) : \mathbf{s}_{\mathbf{0}}^{\alpha}$ and update slip rates
	(b) Update $\mathbf{S}^{i+1}(t+\Delta t) = \mathbf{S}^{i}(t+\Delta t) - \frac{\partial \mathbf{G}}{\partial \mathbf{S}}\Big\|_{i}^{-1} \mathbf{G}(\mathbf{S}^{i}(t+\Delta t))$ from equations (2.33), (2.35), (2.36) and (2.37)
	(c) Check for convergence: if no, go back to step (a); if yes, proceed to step iv.
iv	Evaluate $\tau^{\alpha}\left(\mathbf{S}^{i+1}(t+\Delta t)\right)$ and update slip system shear resistance with SSDs hardening using equations (2.15), (2.16) and (2.17)
v	Check for convergence of SSDs: if no, go back to step iii and compute stress with updated slip system shear resistance; if yes, proceed to step vi
vi	Evaluate $\mathbf{F}^{p}(t+\Delta t)$ and execute step **B**
vii	Calculate $\mathbf{F}^{e}(t+\Delta t) = \mathbf{F}(t+\Delta t)\mathbf{F}^{p^{-1}}(t+\Delta t)$, Cauchy stress $\boldsymbol{\sigma}(t+\Delta t) = \frac{1}{det(\mathbf{F}^{e}(t+\Delta t))}\mathbf{F}^{eT}(t+\Delta t)\mathbf{S}(t+\Delta t)\mathbf{F}^{e}(t+\Delta t)$ and $\mathbf{W} = \frac{\partial \boldsymbol{\sigma}}{\partial \boldsymbol{\varepsilon}}$
Step **B**	Update non-local deformation variables related to GNDs
i	Evaluate $\mathbf{F}^{p}(t+\Delta t)$ using equation (2.31) and compute nodal value of $\mathbf{F}^{p}(t+\Delta t)$ using equation (2.39)
ii	Compute Nye's tensor using equation (2.45) and obtain GND density from equation (2.23)
iii	Update slip system shear resistance with GND hardening using equations (2.24) and (2.26)
iv	Check for convergence in GNDs: if no, go to step **A**-iii with updated GNDs; if yes, proceed to step **A**-vii.

both the hardening effect from the evolution of statistically stored dislocations and geometrically necessary dislocations at grain boundaries. The SSDs are responsible for homogeneous plastic deformation of the lattice which is characterized by vanishing net Burger's vector. The GNDs are driven by plastic incompatibility and account for local dislocation accumulation which enhances the stress concentration close to the grain boundaries. Time integration of the CPFE model consists a local update of stress and SSDs variables at integration points, as well as a non-local computation of GND densities obtained from the nodal value of $\mathbf{F}^{\mathbf{p}}$ by superconvergent patch recovery method.

Chapter 3

Stabilized Tetrahedral Elements for CPFE Analysis Overcoming Volumetric Locking

The polycrystalline microstructures of many metals and alloys are quite complex with sharp and tortuous grain boundaries and multiple grain junctions. Image-based CPFE modeling commonly involves computer generation of virtual polycrystalline microstructures from experimental data, followed by discretization into finite element meshes. Discretization of these domains is best accomplished using three-dimensional four-node tetrahedral or TET4 elements, which conform to the complex geometries [73]. However, it has been commonly observed e.g. in [74–78] that TET4 elements suffer from severe volumetric locking when simulating the deformation of incompressible or nearly incompressible materials. A metric that is used to understand element performance for incompressible or nearly incompressible deformations is termed as the *incompressibility constraint ratio*. It is defined as the ratio of some available degrees of freedom (DOF) to the number of incompressibility constraints in a finite element mesh. Low incompressibility constraint ratio associated with TET4 elements can lead to large spurious hydrostatic stresses in models of plastically deforming metallic materials. This volumetric phenomenon is commonly

ignored by most CPFE modelers who have been focused on the development of constitutive laws. This work aims at developing stable, locking-free TET4 element formulations for efficient and accurate crystal plasticity finite element modeling and simulations.

A variety of methods have been proposed for the stabilization and control of volumetric locking in TET4 elements. A major idea in these methods is to associate nodal points with patches corresponding to an assembly of surrounding sub-elements, and subsequently to integrate the weak form over these patches, thus reducing the incompressibility constraint ratio. An average nodal pressure technique has been proposed for dynamic explicit formulations in [79], where the volumetric strain energy is integrated over the patch for each node. In [75], a node-based uniform strain (NUS) formulation is introduced for four-node tetrahedral elements associated with linear elasticity problems. The volumetric and deviatoric strain energy components are integrated over nodal patches in this formulation. Spurious zero energy modes were identified with this approach in [80], and consequently an additional stabilization term with a modified constitutive law was added to the potential energy functional. This approach was further extended in [81] into a locally integrated weighted strain formulation, where numerical integration is done at local Gauss points instead of nodes. In [76], the fact that instability is linked only to the isochoric strain energy contribution was exploited through a stress splitting operation, to stabilize the formulation in [75]. A generalized node-based, smoothed finite element method (NS-FEM) has been proposed in [82] that adopts an arbitrary polygonal element domain discretization. This

method provides an upper-bound solution for the strain energy and is shown to reduce to the formulation in [75] for the special case of linear tetrahedral elements. The strain smoothing operation in NS-FEM is later extended to edge-based smoothed finite element method (ES-FEM) [83, 84] and face-based smoothed finite element method (FS-FEM) [85]. The above methods are however not suitable for anisotropic crystal plasticity finite element formulations, since the stress or the elasto-plastic tangent stiffness tensor cannot be split into isochoric and deviatoric components. An element formulation with a F-bar patch method has been introduced in [77, 78] to overcome volumetric locking in TET4 elements for finite deformation problems. The original F-bar formulation in [86] was developed for four-node quadrilateral and eight-noded hexahedral elements. This simple and effective model can be used for any constitutive law and is easily implemented in any standard displacement-based finite element code. Other competing strategies in developing locking-free linear tetrahedral elements include stabilizing NUS formulation with additional higher order support function [87], and mixed enhanced elements [74] in which additional augmentation strain fields are used in conjunction with a linearly interpolated pressure field to treat the incompressible constraints. Volume and area bubble functions have been added to mixed tetrahedral elements in [88, 89] to stabilize the displacement and strain fields.

This chapter develops and examines three locking-free stabilized finite element formulations in the context of crystal plasticity finite element or CPFE analysis. They include a node-based uniform strain (NUS) element, a locally integrated B-bar (LIB) based element

and a F-bar patch (FP) based element. The locally integrated B-bar element is based on splitting of the gradient operator matrix **B** for TET4 elements. It selectively reduces the volumetric strain over a nodal patch and keeps the deviatoric strain unchanged in each TET4 element. The results are compared with the different methods and provides a guideline for conducting reliable CPFE analysis.

3.1 TET4 Elements in CPFE Analysis and Associated Volumetric Locking

For any element in the CPFE model, the displacement increment $\triangle\mathbf{u}$, increment of displacement gradient $\frac{\partial\triangle\mathbf{u}}{\partial\mathbf{x}^t}$ and the linearized strain increment $\mathbf{e}$ in equation (2.7) are respectively written as:

$$\triangle\mathbf{u} = \mathbf{N}\triangle\mathbf{q}, \qquad \frac{\partial\triangle\mathbf{u}}{\partial\mathbf{x}^t} = \frac{\partial\mathbf{N}}{\partial\mathbf{x}^t}\triangle\mathbf{q} = \mathbf{G}\triangle\mathbf{q}, \quad \text{and} \quad \mathbf{e} = \mathbf{B}\triangle\mathbf{q} \tag{3.1}$$

For the four-node constant strain tetrahedral or TET4 element, the shape function $\mathbf{N}$ is a 3×12 matrix, $\mathbf{G}$ is a 9×12 gradient operator matrix and $\mathbf{B}$ is the 6×12 strain-displacement matrix. Explicit forms of $\mathbf{N}$, $\mathbf{G}$ and $\mathbf{B}$ for the TET4 element are given in [90]. Stress and strain tensors are represented using the reduced order Voigt vector notation. Substituting equations (3.1) into equation (2.8) and integrating using the one-point Gaussian quadrature rule, yields the discrete form of the finite element equations as:

$$\sum_{i=1}^{N_e}\mathbf{B}^{t^T}\mathbf{C}^t\mathbf{B}^t\Omega^{t,i}\triangle\mathbf{q} + \sum_{i=1}^{N_e}\mathbf{G}^{t^T}\underset{\sim}{\boldsymbol{\sigma}}^t\mathbf{G}^t\Omega^{i,t}\triangle\mathbf{q} = \mathbf{f}^{ext^{t+\Delta t}} - \sum_{i=1}^{N_e}\mathbf{B}^{t^T}\boldsymbol{\sigma}\Omega^{i,t} \tag{3.2}$$

where $\Omega^{t,i}$ is the volume of element i at time t. The matrix $\underset{\sim}{\sigma}^t$ is explicitly written as:

$$\underset{\sim}{\sigma}^t = \begin{bmatrix} \boldsymbol{\sigma}^t & \mathbf{0} & \mathbf{0} \\ \mathbf{0} & \boldsymbol{\sigma}^t & \mathbf{0} \\ \mathbf{0} & \mathbf{0} & \boldsymbol{\sigma}^t \end{bmatrix} \tag{3.3}$$

where $\boldsymbol{\sigma}^t$ is the 3×3 stress matrix, $\mathbf{0}$ is a 3×3 matrix of zeros and $\mathbf{f}^{ext^{t+\Delta t}}$ is the external force vector corresponding to $R^{ext^{t+\Delta t}} = \mathbf{f}^{ext^{t+\Delta t}} : \delta\Delta\mathbf{q}$. The system of equations to be solved are:

$$\mathbf{K}^t \Delta\mathbf{q} = \mathbf{f}^{ext^{t+\Delta t}} - \mathbf{f}^{int^t} \tag{3.4}$$

$\mathbf{K}^t$ and $\mathbf{f}^{int^t}$ are the global stiffness matrix and internal force vector respectively. The material tangent stiffness tensor $\mathbf{C}^\mathbf{t}$ is needed for the evaluation of $\mathbf{K}^t$. The formulation of $\mathbf{C}^\mathbf{t}$ consistent with the proposed crystal plasticity constitutive model, is given in section 2.2.3 in chapter 2.

3.1.1 Volumetric locking in TET4 elements

TET4 elements are known to exhibit volumetric locking for incompressible or nearly incompressible materials. A simple example illustrates the occurrence of volumetric locking emanating from numerical interpolation of strains in the TET4 element. Consider a nearly-incompressible elastic bar of dimensions $4 \times 2 \times 2$ units, with Young's modulus $E = 1\ GPa$ and Poisson's ratio $\nu = 0.4999$. The bar is discretized into 6 TET4 elements as shown in

figure 3.1. The nodal coordinates and element connectivity list are tabulated in table 3.1.

All the 8 nodes are subjected to prescribed values corresponding to the displacement field

$$u_x = \frac{xy}{2}, \qquad u_y = \frac{x^2}{4} - \frac{\nu}{4(1-\nu)}y^2, \qquad u_z = 0 \tag{3.5}$$

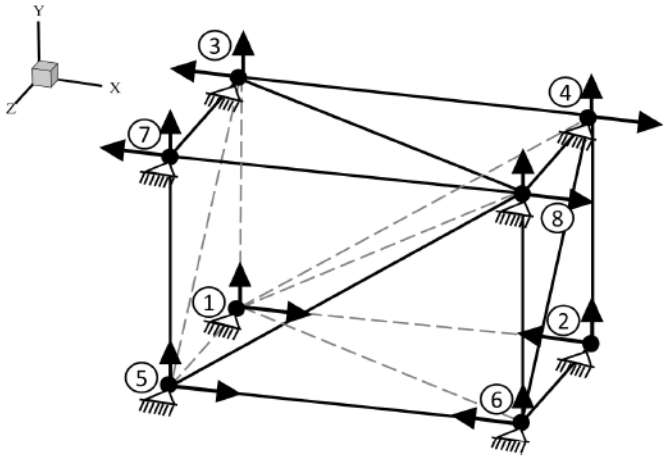

Figure 3.1: Mesh of TET4 elements subject to nodal displacements for illustrating volumetric locking.

Node ID	1	2	3	4	5	6	7	8
Coordinates	-2,-1,-1	2,-1,-1	-2, 1,-1	2, 1,-1	-2,-1,1	2,-1,1	-2,1,1	2,1,1

Element ID	1	2	3	4	5	6
Connectivity	1, 3, 8, 4	1, 3, 5, 8	3, 5, 8, 7	1, 2, 4, 6	1, 6, 8, 5	1, 4, 8, 6

Table 3.1: Nodal coordinates and element connectivity for the FE model in figure 3.1

The normal components of linear strain, corresponding to the prescribed displacement field, is analytically obtained as:

$$e_{xx} = \frac{y}{2}, \; e_{yy} = -\frac{\nu y}{2(1-\nu)}, \; e_{zz} = 0 \tag{3.6}$$

The corresponding volumetric strain is given as $e_{xx} + e_{yy} + e_{zz} = \frac{1-2\nu}{2(1-\nu)}y$. This is clearly dependent on the Poisson's ratio ν and the location y. For the given geometry $y \in [-1, 1]$ and Poisson's ratio $\nu = 0.4999$ the volumetric strain is nearly zero. However, for TET4 elements, the volumetric strain due to the use of the shape functions is clearly non-zero as listed in table 3.2. The large volumetric strains induce high spurious dilatational energy that results in element locking and high stresses.

Strain Component	Element ①	Element ②	Element ③	Element ④	Element ⑤	Element ⑥
e_{xx}	0.25	0.25	0.25	-0.25	-0.25	-0.25
e_{yy}	0	0	0	0	0	0
Volumetric	0.25	0.25	0.25	-0.25	-0.25	-0.25

Table 3.2: Strain components for each TET4 element for the problem in figure 3.1

Crystal plasticity constitutive models exhibit isochoric plastic flow, i.e. $det\ \mathbf{F}^p = 1$. Since plastic strains are significantly larger than elastic strains, the use of TET4 element in CPFE simulations may result in volumetric locking under different deformation modes, e.g. bending.

3.2 Locking-Free Formulations for TET4 Elements

Stabilization of TET4 elements, through node-based uniform strain (NUS) formulation was introduced in [75]. While the NUS method has been successful in avoiding volumetric locking, spurious zero energy modes were reported in [76]. Alternately, the **F**-bar patch

(FP) formulation [77, 78] has been shown to alleviate volumetric locking without the reintroduction of spurious zero energy modes. As an extension to the NUS formulation, a locally integrated B-bar (LIB) element is developed to stabilize TET4 elements in this work. The methods are termed in this work as locking free stabilized or LFS-TET4 elements. These formulations are summarized in the context of CPFE formulation in this section.

3.2.1 Node-based uniform strain (NUS) element formulation

In the NUS formulation, a patch of sub-elements is assigned to each nodal point in the finite element mesh. Consider $\hat{\Omega}^{s,t}$ to denote such a patch assigned to a node s at time t that is defined as:

$$\hat{\Omega}^{s,t} = \sum_{i=1}^{N^s} \Omega_s^{i,t} = \sum_{i=1}^{N^s} \alpha_s^i \, \Omega^{i,t} \tag{3.7}$$

N^s corresponds to the number of TET4 elements attached to the node s, $\Omega_s^{i,t}$ is the volume contribution of the $i-th$ TET4 element to the patch $\hat{\Omega}^s$ and α_s^i is a scalar weighting factor. For 3D meshes, $\alpha_s^i = \frac{1}{4}$. Figure 3.2a illustrates a 2D patch construction method for a node s, while figure 3.2b shows the partitioning of a 3D TET4 element to generate its contribution $\Omega_s^{i,t}$ to the patch.

Within each patch, the linear strain increment $\hat{\mathbf{e}}^s$ is taken to be uniform and obtained as the average value from surrounding elements, i.e. :

$$\hat{\mathbf{e}}^s = \sum_{i=1}^{N^s} w^i \mathbf{e}^{i,t} = \sum_{i=1}^{N^s} w^i \mathbf{B}^{i,t} \Delta \mathbf{q}^i = \hat{\mathbf{B}}^{s,t} \, \triangle \hat{\mathbf{q}}^s \tag{3.8}$$

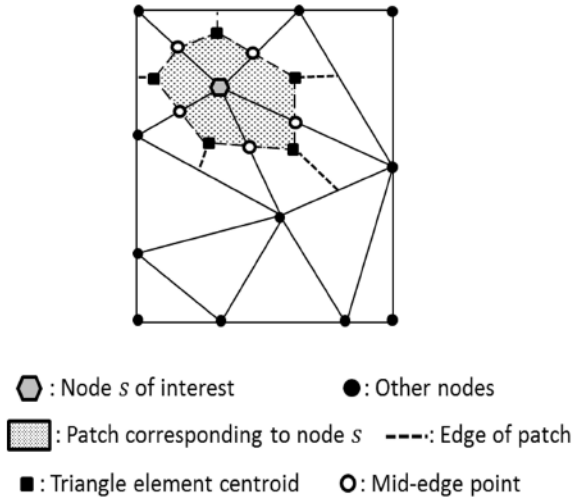

(a)

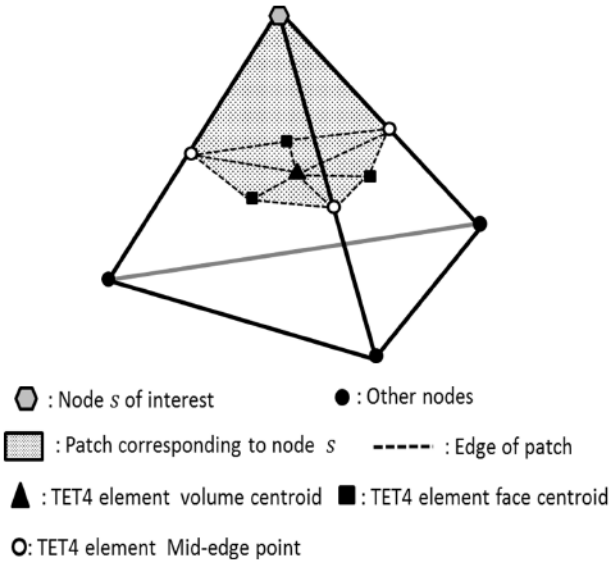

(b)

Figure 3.2: (a) 2D patch construction for node s; (b) 3D volume partitioning $\Omega_s^{i,t}$ for node s, in the NUS method .

where w^i is a relative volume-based weight for element i and $\hat{\mathbf{B}}^{t,s}$ is the gradient matrix associated with the patch s that is obtained by assembling $\mathbf{B}^{i,t}$ from surrounding elements with weight w^i. From equation (3.7) $w^i = \frac{1}{4}\frac{\Omega^{i,t}}{\hat{\Omega}^{s,t}}$. $\triangle\hat{\mathbf{q}}^s$ is the displacement increment vector associated with the patch s, obtained by assembling $\mathbf{q}^i$ from surrounding elements. Nodal averaging of the gradient of displacement increment $\frac{\partial\triangle\mathbf{u}}{\partial\mathbf{x}^t}$ is obtained in the same way as:

$$\left[\begin{array}{ccccccccc} \frac{\partial\triangle u_1}{\partial x_1^t} & \frac{\partial\triangle u_1}{\partial x_2^t} & \frac{\partial\triangle u_1}{\partial x_3^t} & \cdots & \frac{\partial\triangle u_3}{\partial x_1^t} & \frac{\partial\triangle u_3}{\partial x_2^t} & \frac{\partial\triangle u_3}{\partial x_3^t} \end{array}\right]^T_{patch\ s} = \sum_{i=1}^{N^s} w^i \mathbf{G}^{i,t}\ \triangle\mathbf{q}^i = \hat{\mathbf{G}}^{s,t}\ \triangle\hat{\mathbf{q}}^s \quad (3.9)$$

$\hat{\mathbf{G}}^{s,t}$ is the gradient matrix associated with the patch s created by assembling $\mathbf{G}^{i,t}$ from surrounding elements with weight w^i. From equation (2.7), (3.8) and (3.9) it is seen that the strain increment $\triangle\mathbf{E}$ over the patch is uniform, which makes the cumulative strain uniform as well.

The linearized weak form (2.8) with constant strain patches is represented for the discrete model as:

$$\sum_{s=1}^{N_{nodes}} \int_{\hat{\Omega}^{s,t}} \mathbf{C}^{s,t} : \hat{\mathbf{e}}^s \delta\hat{\mathbf{e}}^s\, d\hat{\Omega}^{s,t} + \sum_{s=1}^{N_{nodes}} \int_{\hat{\Omega}^{s,t}} \boldsymbol{\sigma}^{s,t} : \delta\hat{\boldsymbol{\eta}}^s d\hat{\Omega}^{s,t} = R^{ext^{t+\Delta t}} - \sum_{s=1}^{N_{nodes}} \int_{\hat{\Omega}^{s,t}} \boldsymbol{\sigma}^{s,t} : \delta\hat{\mathbf{e}}^s\, d\hat{\Omega}^{s,t} \quad (3.10)$$

where $\boldsymbol{\sigma}^{s,t}$ is the Cauchy stress, obtained from the constitutive model, and $\mathbf{C}^{s,t}$ is the crystal plasticity tangent stiffness matrix in node-based patch s. The NUS formulation assumes that $\mathbf{C}^{s,t}$ and $\boldsymbol{\sigma}^{s,t}$ are also uniform and constant over the patch s. Thus the one-point numerical integration may be used for each patch and the crystal plasticity constitutive updates are

made for the node of the patch. This removes volumetric locking through a reduction in the number of incompressibility constraints. The incompressibility constraint ratio approaches an optimal value of 3. Substituting equation (3.8) and (3.9) into equation (3.10), the tangent stiffness matrix and internal nodal force vector are derived as:

$$\mathbf{K}^t = \sum_{s=1}^{N_{nodes}} \hat{\mathbf{B}}^{s,t,T}\, \mathbf{C}^{s,t}\, \hat{\mathbf{B}}^{s,t} \hat{\Omega}^{s,t} + \sum_{s=1}^{N_{nodes}} \hat{\mathbf{G}}^{s,t,T}\, \underset{\sim}{\boldsymbol{\sigma}}^{s,t}\, \hat{\mathbf{G}}^{s,t} \hat{\Omega}^{s,t} \tag{3.11a}$$

$$\mathbf{f}^{int^t} = \sum_{s=1}^{N_{nodes}} \hat{\mathbf{B}}^{s,t,T}\, \boldsymbol{\sigma}^{s,t} \hat{\Omega}^{s,t} \tag{3.11b}$$

This node-based uniform strain (NUS) element has however been reported to exhibit spurious zero or low energy modes in [80]. Such spurious energy modes can cause large distortion of the TET4 element and eventually lead to a negative determinant of the Jacobian matrix.

3.2.2 Locally integrated B-bar (LIB) element

Several stabilization methods have been developed to overcome the zero-energy modes in the original NUS formulation [76, 80]. These methods are based on splitting the stress or the tangent stiffness matrix $\mathbf{C}$. Such decomposition is not however possible in CPFE analysis with anisotropic elasto-plastic stiffness matrix $\mathbf{C}$. To overcome this issue, a locally integrated B-bar (LIB) based element is proposed in this work. Following procedures in [91], the linear strain increment is decomposed into volumetric and deviatoric parts by

splitting the gradient matrix $\mathbf{B}$ in this formulation, i.e.

$$\mathbf{e} = \mathbf{e}^{vol} + \mathbf{e}^{dev} = \mathbf{B}^{vol}\triangle\mathbf{q} + \mathbf{B}^{dev}\triangle\mathbf{q} \tag{3.12}$$

Only the volumetric part of the linear strain increment $\mathbf{e}^{vol}$ is assumed to be uniform inside the patch for each node to reduce constraints. For node s, the uniform volumetric strain increment $\hat{\mathbf{e}}^{s,vol}$ is obtained as:

$$\hat{\mathbf{e}}^{s,vol} = \sum_{i=1}^{N^s} w^i \mathbf{e}^{i,vol} = \sum_{i=1}^{N^s} w^i \mathbf{B}^{i,vol}\triangle\mathbf{q}^i = \bar{\mathbf{B}}^{s,vol}\triangle\hat{\mathbf{q}}^s \tag{3.13}$$

$\bar{\mathbf{B}}^{s,vol}$ is the volumetric part of the gradient matrix associated with patch s that is assembled from surrounding element $\mathbf{B}^{i,vol}$'s with weights w^i. The deviatoric part of the strain increment $\mathbf{e}^{dev}$ is constant over each TET4 element. This leads to two separate distributions of the volumetric and deviatoric strain increment over the domain, as illustrated in figure 3.3.

Each TET4 element is divided into 4 equal sub-domains. Within each sub-domain, the volumetric and deviatoric parts of the strain increment are constant. The strain increment in a sub-domain $\Omega^{i,s}$ is thus represented as:

$$\bar{\mathbf{e}}^{i,s} = \bar{\mathbf{e}}^{s,vol} + \mathbf{e}^{i,dev} = \bar{\mathbf{B}}^{s,vol}\triangle\hat{\mathbf{q}}^s + \mathbf{B}^{i,dev}\triangle\mathbf{q}^i = \bar{\mathbf{B}}^{i,s}\triangle\hat{\mathbf{q}}^s \tag{3.14}$$

$\bar{\mathbf{B}}^{i,s}$ is the modified gradient matrix associated with sub-domain $\Omega^{i,s}$. Note that $\triangle\mathbf{q}^i$ is contained in $\triangle\hat{\mathbf{q}}^s$ as shown in equation (3.8). Thus it allows the additive decomposition

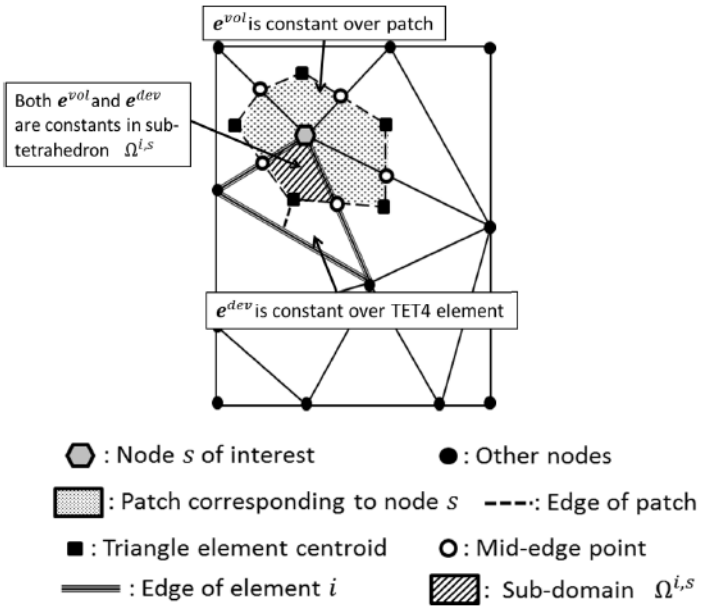

Figure 3.3: Strain distributions in the patch, tetrahedron and sub-domain of tetrahedron in the LIB method.

$\bar{\mathbf{B}}^{i,s} = \bar{\mathbf{B}}^{s,vol} + \mathbf{B}^{i,dev}$. Analogous to $\mathbf{B}$, the 9×12 gradient matrix $\mathbf{G}$ can be split into volumetric and deviatoric parts i.e. $\mathbf{G} = \mathbf{G}^{vol} + \mathbf{G}^{dev}$. The explicit form of $\mathbf{G}^{vol}$ is :

$$\mathbf{G}^{vol} = \left[\mathbf{G}^{vol}_{n1}, \mathbf{G}^{vol}_{n2}, \mathbf{G}^{vol}_{n3}, \mathbf{G}^{vol}_{n4} \right] \tag{3.15}$$

where $n1, ..., n4$ are the local node indices in the element. For any $a \in [n1, ..., n4]$, $\mathbf{G}_a^{vol}$ is explicitly written as:

$$\mathbf{G}_a^{vol} = \begin{bmatrix} G_1 & G_2 & G_3 \\ 0 & 0 & 0 \\ 0 & 0 & 0 \\ 0 & 0 & 0 \\ G_1 & G_2 & G_3 \\ 0 & 0 & 0 \\ 0 & 0 & 0 \\ 0 & 0 & 0 \\ G_1 & G_2 & G_3 \end{bmatrix} \tag{3.16}$$

where $G_i = \frac{\partial N_a}{\partial x_i}$ and N_a is the shape function associated with node a. Substituting $\mathbf{G}^{vol}$ and $\mathbf{G}^{dev}$, the 9×1 displacement gradient vector in the sub-domain $\mathbf{\Omega}^{i,s}$ is expressed as:

$$\begin{bmatrix} \frac{\partial \triangle u_1}{\partial x_1^t} & \frac{\partial \triangle u_1}{\partial x_2^t} & \frac{\partial \triangle u_1}{\partial x_3^t} & \cdots & \frac{\partial \triangle u_3}{\partial x_1^t} & \frac{\partial \triangle u_3}{\partial x_2^t} & \frac{\partial \triangle u_3}{\partial x_3^t} \end{bmatrix}_{\Omega_s^i}^T = \bar{\mathbf{G}}^{s,vol} \triangle \hat{\mathbf{q}}^s + \mathbf{G}^{i,dev} \triangle \mathbf{q}^i = \bar{\mathbf{G}}^{i,s} \triangle \hat{\mathbf{q}}^s \tag{3.17}$$

Correspondingly, the linearized weak form (2.8) with constant strain sub-domains reduces to:

$$\sum_{i=1}^{N_{sub-tet}} \int_{\Omega^{i,t}} \mathbf{C}^{i,t} : \bar{\mathbf{e}}^i \delta \bar{\mathbf{e}}^i \, d\Omega^{i,t} + \sum_{i=1}^{N_{sub-tet}} \int_{\Omega^{i,t}} \boldsymbol{\sigma}^{i,t} : \delta \bar{\boldsymbol{\eta}}^i d\Omega^{i,t} = R^{ext^{t+\Delta t}} - \sum_{i=1}^{N_{sub-tet}} \int_{\Omega^{i,t}} \boldsymbol{\sigma}^{i,t} : \delta \bar{\mathbf{e}}^i \, d\Omega^{i,t} \tag{3.18}$$

where $N_{sub-tet}$ $(= 4 \times N_e)$ is the total number of sub-domains and $\mathbf{\Omega}^{i,t}$ is the sub-domain volume at time t. $\boldsymbol{\sigma}^{i,t}$ and $\mathbf{C}^{i,t}$ are updated using the crystal plasticity constitutive models. Again it is assumed they are uniform and constant over the sub-domain i and one-point numerical integration can be used.

$\mathbf{C}^{i,t+\Delta t}$ and $\boldsymbol{\sigma}^{i,t+\Delta t}$ depend on the deformation gradient $\mathbf{F}_0^t$, as well as other history-dependent state variables. In the LIB element formulation, the evaluation of $\mathbf{F}_0^{t+\Delta t}$ in each sub-domain must be consistent with the interpolation of strain with $\bar{\mathbf{B}}$. This is achieved using the following relation:

$$\mathbf{F}_0^{t+\Delta t} = \mathbf{F}_t^{t+\Delta t}\mathbf{F}_0^t = \left(\mathbf{I} + \frac{\partial \triangle \mathbf{u}}{\partial \mathbf{x}^t}\right)\frac{\partial \triangle \mathbf{x}^t}{\partial \mathbf{x}^0} = \left(\mathbf{I} + \bar{\mathbf{G}}^t \triangle \mathbf{q}\right)\frac{\partial \triangle \mathbf{x}^t}{\partial \mathbf{x}^0} \tag{3.19}$$

Substituting equations (3.14) and (3.17) into (3.18), the tangent stiffness matrix and internal nodal force vector in the LIB element formulation are expressed as:

$$\mathbf{K}^t = \sum_{i=1}^{N_{sub-tet}} \bar{\mathbf{B}}^{i,t\,T}\,\mathbf{C}^{i,t}\,\bar{\mathbf{B}}^{i,t}\mathbf{\Omega}^{i,t} + \sum_{i=1}^{N_{sub-tet}} \bar{\mathbf{G}}^{i,t\,T}\,\underset{\sim}{\boldsymbol{\sigma}}^{i,t}\,\bar{\mathbf{G}}^{i,t}\mathbf{\Omega}^{i,t} \tag{3.20a}$$

$$\mathbf{f}^{int^t} = \sum_{i=1}^{N_{sub-tet}} \bar{\mathbf{B}}^{i,t\,T}\,\boldsymbol{\sigma}^{i,t}\mathbf{\Omega}^{i,t} \tag{3.20b}$$

The LIB element selectively reduces the volumetric strain components over the node-based patch and keeps the deviatoric strain components unchanged in each tetrahedral element. This stabilization method effectively alleviates volumetric locking without introducing spu-

rious zero-energy modes.

3.2.3 F-bar patch-based (FP) element

The **F**-bar patch (FP) based stabilization method has been proposed in [77] for relieving volumetric locking in lower order tetrahedral elements. The **F**-bar patch method modifies the deformation gradient for stress tensor calculations such that incompressibility is enforced in the element in a weak sense, rather than a point-wise enforcement.

The Cauchy stress at the end of a time interval $[t, t + \Delta t]$ may be computed in terms of the deformation gradient and state variables α_t at time t as:

$$\boldsymbol{\sigma}^{t+\Delta t} = \boldsymbol{\sigma}\left(\alpha^t, \mathbf{F}^{t+\Delta t}\right) \tag{3.21}$$

The deformation gradient is decomposed into isochoric and volumetric components as:

$$\mathbf{F} = \mathbf{F}_{iso}\mathbf{F}_{vol} \quad \text{where } \mathbf{F}_{iso} = (det\mathbf{F})^{-\frac{1}{3}}\mathbf{F} \text{ and } \mathbf{F}_{vol} = (det\mathbf{F})^{\frac{1}{3}}\mathbf{I} \tag{3.22}$$

In the original **F**-bar formulation for four-node quadrilateral and eight-node hexahedral elements in [86], **F** is first calculated at all Gauss quadrature points, as well as $\mathbf{F}_0$ at the element centroid. Subsequently, the stabilized deformation gradient $\bar{\mathbf{F}}$ at the Gauss points

are obtained by replacing the volumetric component with its value at the centroid, i.e.

$$\bar{\mathbf{F}} = \mathbf{F}_{iso}\left(\mathbf{F}_0\right)_{vol} = \left(\frac{det\mathbf{F}_0}{det\mathbf{F}}\right)^{\frac{1}{3}}\mathbf{F} \tag{3.23}$$

This implies that the determinant of $\bar{\mathbf{F}}$ within the element is equal to the determinant of $\mathbf{F}_0$. Thus, incompressibility in the constitutive model is enforced only at the centroid of the element, rather than at all Gauss points. The constitutive model is then solved at Gauss points using $\bar{\mathbf{F}}$, i.e.

$$\boldsymbol{\sigma}^{t+\Delta t} = \boldsymbol{\sigma}\left(\alpha_t, \bar{\mathbf{F}}^{t+\Delta t}\right) \tag{3.24}$$

This methodology has been effective in overcoming volumetric locking for bilinear quadrilateral and trilinear hexahedral elements in [86]. However it is not directly applicable to linear tetrahedral elements as they have only one Gauss point located at the element centroid. Additionally the deformation gradient is constant in the element and hence, $\bar{\mathbf{F}}$ in equation (3.23) becomes:

$$\bar{\mathbf{F}} = \mathbf{F}_0 = \mathbf{F} \tag{3.25}$$

Clearly, this relation will not help in overcoming volumetric locking in TET4 elements in the incompressibility limit. A modified formulation has been proposed in [77] where constitutive incompressibility is enforced over a patch of elements, rather than in each element. This requires that elements in the mesh be assigned to non-overlapping patches as illustrated in figure 3.4 in 2D. Let $\mathscr{P}$ denote a set of elements forming a patch. The

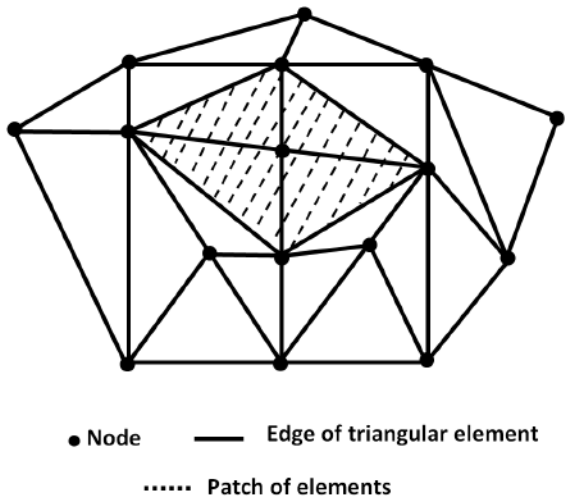

Figure 3.4: Patch of elements in the **F**-bar-patch method

modified deformation gradient for element $K \in \mathscr{P}$, is defined as

$$\bar{\mathbf{F}}_K = \left[\frac{\Omega^{t+\Delta t}_{patch}}{\Omega^{0}_{patch}\, det\mathbf{F}_K} \right]^{\frac{1}{3}} \mathbf{F}_K \tag{3.26}$$

where $\Omega^{t+\Delta t}_{patch}$ and Ω^{0}_{patch} are respectively the current and undeformed volumes of the patch $\mathscr{P}$, calculated as:

$$\Omega^{0}_{patch} = \sum_{K \in \mathscr{P}} \Omega^{K,0} \quad , \quad \Omega^{t+\Delta t}_{patch} = \sum_{K \in \mathscr{P}} \Omega^{K,t+\Delta t} \tag{3.27}$$

It is noteworthy that **F**-bar patch method reduces to the conventional tetrahedral element formulation if each element is identified with a patch. Adding more elements to the patch relaxes the incompressibility constraint ratio and helps relieve volumetric locking. However, the presence of too many elements in a patch may result in spurious energy modes. Through numerical experiments, it was inferred in [78] that 8 elements per patch is adequate

for 3D problems without spurious mechanisms.

The internal force vector in the **F**-bar patch method is evaluated using the modified deformation gradient in equation (3.26) as:

$$\mathbf{f}^{int^K} = \Omega^{K,t}\mathbf{B}^{K,t^T}\boldsymbol{\sigma}^{K,t} \tag{3.28}$$

The tangent stiffness matrix has a non-conventional structure in the sense that it not only depends on the degrees of freedom of the element, but also on the degrees of freedom of other elements in the patch. The tangent stiffness matrix for element K is derived as:

$$\mathbf{K}^{KK} = \Omega^{K,t}\ \mathbf{G}^{K,t^T}\ \mathbf{a}\ \mathbf{G}^{K,t} + \left(\frac{\Omega^{K,t}}{\Omega^{t}_{patch}} - 1\right)\Omega^{K,t}\ \mathbf{G}^{K,t^T}\ \mathfrak{I}\ \mathbf{G}^{K,t} \tag{3.29a}$$

$$\mathbf{K}^{KJ} = \frac{\Omega^{K,t^2}}{\Omega^{t}_{patch}}\ \mathbf{G}^{K,t^T}\ \mathfrak{I}\ \mathbf{G}^{J,t}, \quad J \in \mathscr{P}; \quad J \neq K \tag{3.29b}$$

Here $\mathbf{K}^{KK}$ corresponds to stiffness components whose rows and columns are associated with the degrees of freedom of element K, whereas $\mathbf{K}^{KJ}$ corresponds to components whose rows and columns are respectively associated with the degrees of freedom of elements K and J in the patch, *s.t.* $J \neq K$. The fourth-order spatial elasticity tensor **a** is evaluated at $\mathbf{F} = \bar{\mathbf{F}}$ [78], as

$$a_{ijkl} = \frac{1}{det\mathbf{F}} A_{imkn} F_{jm} F_{ln} \tag{3.30}$$

where **A** denotes the elasticity tensor derived from the first Piola-Kirchhoff stress **P** as

$A_{imkn} = \frac{\partial P_{im}}{\partial F_{kn}}$. $\mathfrak{I}$ in equation (3.29) corresponds to the fourth-order tensor $\mathfrak{I} = \frac{1}{3}\mathbf{a} : (\mathbf{I} \otimes \mathbf{I}) - \frac{2}{3}(\boldsymbol{\sigma} \otimes \mathbf{I})$.

The FP method is flexible to be used for various material constitutive models. Its implementation in any standard displacement-based FE code is quite straightforward as DOFs are merely nodal displacements and constitutive updates are performed at the element quadrature points. While the calculation of internal force vector is similar to that for TET4 elements, evaluation and assembly of the tangent stiffness matrix in (3.29) requires more attention.

3.2.4 Applying LIB and FP Stabilization Methods in Polycrystalline CPFE Models

This section examines the application of LIB and FP induced LFS-TET4 elements to finite element models of polycrystalline microstructures, incorporating non-local rate-dependent crystal plasticity constitutive models. A special feature of these models is that they must account for discrete polycrystalline grain boundaries in the construction of the FE mesh and associated sub-structures. The constitutive update algorithms for the time increment between t and $t+\Delta t$, use implicit time integration methods [92] to evaluate the Cauchy stress $\hat{\boldsymbol{\sigma}}^{t+\Delta s,t}$, slip rates and all deformation state variables, as well as evaluating the fourth-order tangent moduli tensor $\mathbf{C}^{t+\Delta s,t}$. Important steps in the implementation are discussed next.

Creating stabilization patches conforming to grain boundaries

For polycrystalline microstructures, the node-based patches needed with the LIB and the FP methods must conform to the grain structures. Consider a node s located on the grain boundary of a 2D model as shown in figure 3.5. Slip systems are not continuous across the boundary of grains with crystallographic misorientation, which leads to discontinuities in the plastic strains. With this consideration, the patch assigned to the node s should not cross grain boundaries. It is not logical to construct and smooth over a single patch for a grain boundary node that connects multiple grains. Correspondingly sub-patches that are exclusive to a single grain are created with representation:

$$\hat{\Omega}^{s,t} = \hat{\Omega}^{s,t}_{grain_1} + \hat{\Omega}^{s,t}_{grain_2} \tag{3.31a}$$

$$\text{where } \hat{\Omega}^{s,t}_{grain_1} = \sum_{K=1}^{N^s_{grain_1}} \frac{1}{4}\,\Omega^{K,t} \quad \text{and} \quad \hat{\Omega}^{s,t}_{grain_2} = \sum_{J=1}^{N^s_{grain_2}} \frac{1}{4}\,\Omega^{J,t} \tag{3.31b}$$

Here $N^s_{grain_1}$ and $N^s_{grain_2}$ correspond to the number of TET4 elements attached to a node s that is common to grains 1 and 2. This procedure can be generalized for nodes at triple and quadruple points. The smoothing process, and evaluation of constitutive variables, tangent stiffness matrix and internal forces, are carried out separately for each sub-patch.

3.3 Numerical Examples and Discussions

The performance of the locally integrated B-bar (LIB) and **F**-bar patch (FP) based TET4 elements in CPFE analysis of polycrystalline materials is studied in this section. A standard

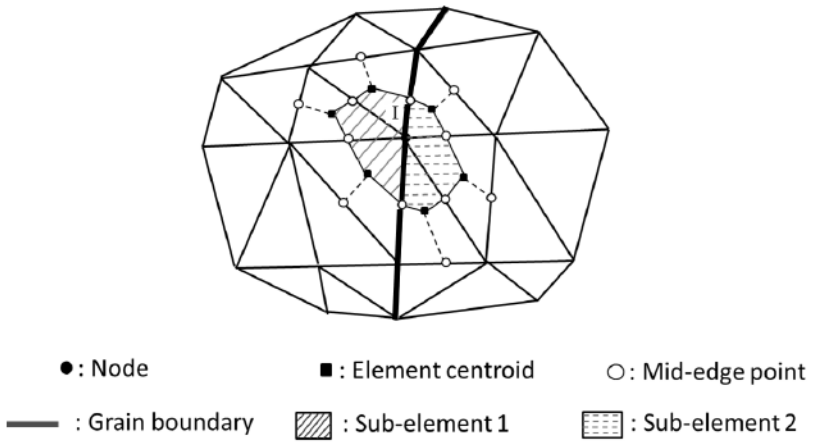

Figure 3.5: Constructing sub-patches for nodes on grain boundary in polycrystalline microstructures.

patch test is performed in the first example. Subsequently an elastic bending problem and several crystal plasticity examples, including a bicrystal compression test, polycrystalline beam bending and constant strain rate deformation of a polycrystalline aggregate, are solved. The results are compared with those of the standard TET4 element. When possible, the 8-noded hexahedral element with B-bar stabilization method is used to generate reference solutions for comparison. The computational costs for different element formulations are then compared for a crystal plasticity problem. For crystal plasticity problems, two low-symmetry HCP metallic alloys, viz. a magnesium alloy $AZ31$ and titanium alloy $Ti6Al$, are chosen for numerical simulations. For Mg alloy simulations, the constitutive model presented in chapter 2 is used, while a constitutive model described in [52] is used for Ti alloys.

3.3.1 Element patch test

The patch test is a necessary condition that should be satisfied for all elements in a finite element ensemble. This test is performed on a $20 \times 20 \times 40$ cube discretized into 48 TET4 elements with 8 nodes on the outer surfaces and 13 nodes inside the cube. The material is assumed to be isotropic, linear elastic. Nodal displacements on the outer surfaces are prescribed using linear functions as:

$$\triangle u_1 = \frac{z+20}{200} - \frac{x-10}{100}, \qquad \triangle u_2 = \frac{z+20}{200} - \frac{y-10}{100}, \qquad \triangle u_3 = 0 \tag{3.32}$$

Nodal displacements inside the cube are calculated for NUS, LIB and FP based TET4 elements. A norm of the displacement error is defined as:

$$\overline{err}_{dis} = \frac{\sum_{\alpha=1}^{8}\sum_{i=1}^{3}\left(\mathbf{u}_{\alpha\, i}^{exact} - \mathbf{u}_{\alpha\, i}^{FE}\right)^2}{\sum_{\alpha=1}^{8}\sum_{i=1}^{3}\left(\mathbf{u}_{\alpha\, i}^{exact}\right)^2}$$

For both LIB and FP elements $\overline{err}_{dis} \leq 2.22 \times 10^{-15}$ and hence they pass the standard patch test. The NUS element, however, does not pass the patch test since the determinant of the Jacobian of some elements becomes negative and the elements undergo non-physical distortion. This corresponds to the presence of spurious modes in NUS element.

3.3.2 Bending of an elastic beam

In this example, a nearly incompressible elastic beam, subjected to a bending moment, is solved using the LIB, FP and standard TET4 elements. The material is isotropic, linear elastic with Young's modulus $E = 300$ MPa and Poisson ratio $\nu = 0.4999$. Dimensions of the beam are $4m \times 1m \times 1m$, which is discretized into 31758 elements consisting of 6513 nodes. The bending moment boundary condition is manifested through imposing a linearly distributed normal stress σ_{xx} on the $x = 4.0m$ surface. Displacement boundary conditions are applied on the surface $x = 0.0m$ to constrain rigid body motion, as shown in figure 3.6.

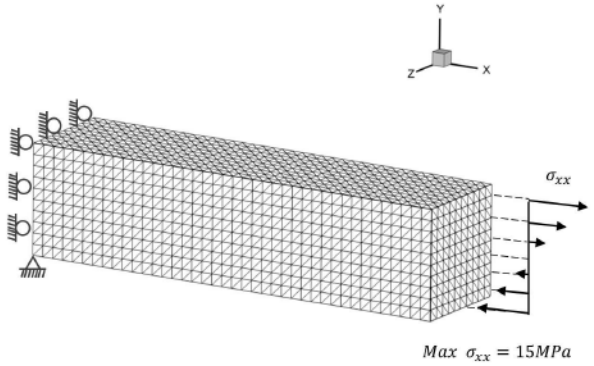

Figure 3.6: Mesh and boundary condition for the elastic beam bending problem

TET4 elements exhibits volumetric locking for nearly incompressible materials due to too many incompressibility constraints. To generate a locking-free *reference solution*, the beam is solved using 4961 nodes and 4000 8-noded hexahedral elements with B-bar

stabilization [91]. The maximum tip deflections are tabulated in table 3.3. The results clearly show that the standard TET4 element suffers from severe volumetric locking, resulting in very stiff behavior. The LIB and FP elements, on the other hand, provide satisfactory results in comparison with the reference solution. Convergence of the LIB and FP elements are

	8-noded hexahedral element with B-bar stabilization	Standard TET4 element	LIB element	FP element
Beam tip deflection	0.785m	0.271m	0.773m	0.779m

Table 3.3: Maximum tip deflection of the bending dominated elastic beam at the limits of incompressibility using different element formulations

examined by solving the beam problem with 5 different meshes consisting of 343, 845, 1246, 2929, 6513 nodes respectively. The tip deflections predicted by the LIB and FP elements with a patch size of 4 tetrahedrons (FP4) and FP element with a patch size of 8 tetrahedrons (FP8) are plotted in the figure 3.7. The reference solution using 8-noded hexahedral element with B-bar stabilization is plotted with the dashed line. The FP8 element shows the softest response and its solution is closest to the reference solution. This is due to the fact that a larger patch in the FP8 element is able to further reduce the incompressibility constraints. The patch construction for the LIB element formulation does not involve flexible patch size and it is observed that this element solution lies between those of FP4 and FP8 for all the meshes.

3.3.3 Bicrystal compression test

A bicrystal uniaxial compression loading test is simulated in this example to understand the effect of volumetric locking in crystal plasticity FE analyses. The loading is applied along

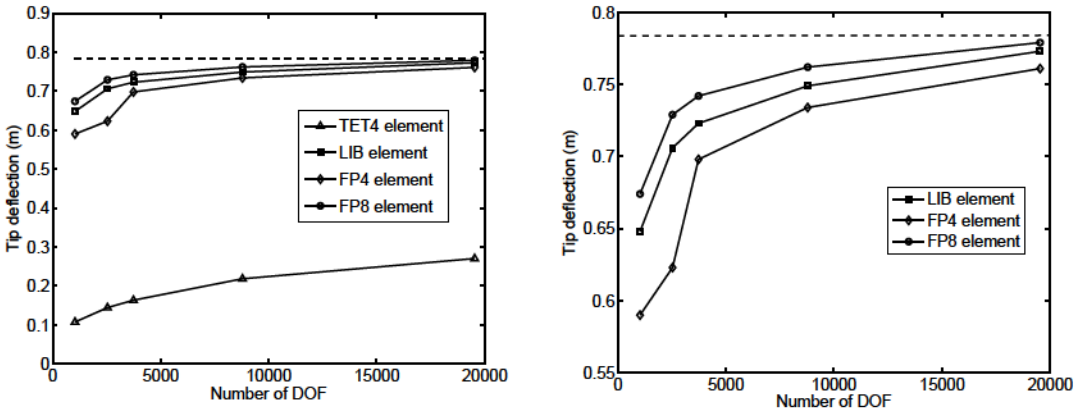

Figure 3.7: (a) Convergence of the tip deflection for different element formulations. The dashed line corresponds to the reference solution predicted by 8-noded hexahedral element with B-bar stabilization. (b) zoomed-in view of (a) showing the difference between LIB, FP4 and FP8 elements.

Z direction and simulations are conducted using standard TET4, LIB and FP elements. Grain boundaries are important in crystal plasticity analysis as they produce dislocation pile-ups, stress concentration and often trigger failure initiation. A flat simple-tilt grain boundary in the bicrystal is chosen in this example. The grain boundary is characterized by crystal orientations, which have Euler angles $[0°, 0°, 0°]$ and $[0°, 90°, 0°]$ defined in the $Z - X - Z$ convention for crystals 1 and 2 respectively. Both crystals have a dimension of $10\mu m \times 10\mu m \times 10\mu m$, as shown in figure 3.8a. Displacement boundary conditions are applied on the top surface and minimum displacement boundary conditions are imposed on other surfaces to remove the rigid body modes. The material constitutive models are those of the magnesium alloy AZ31 developed in [92].

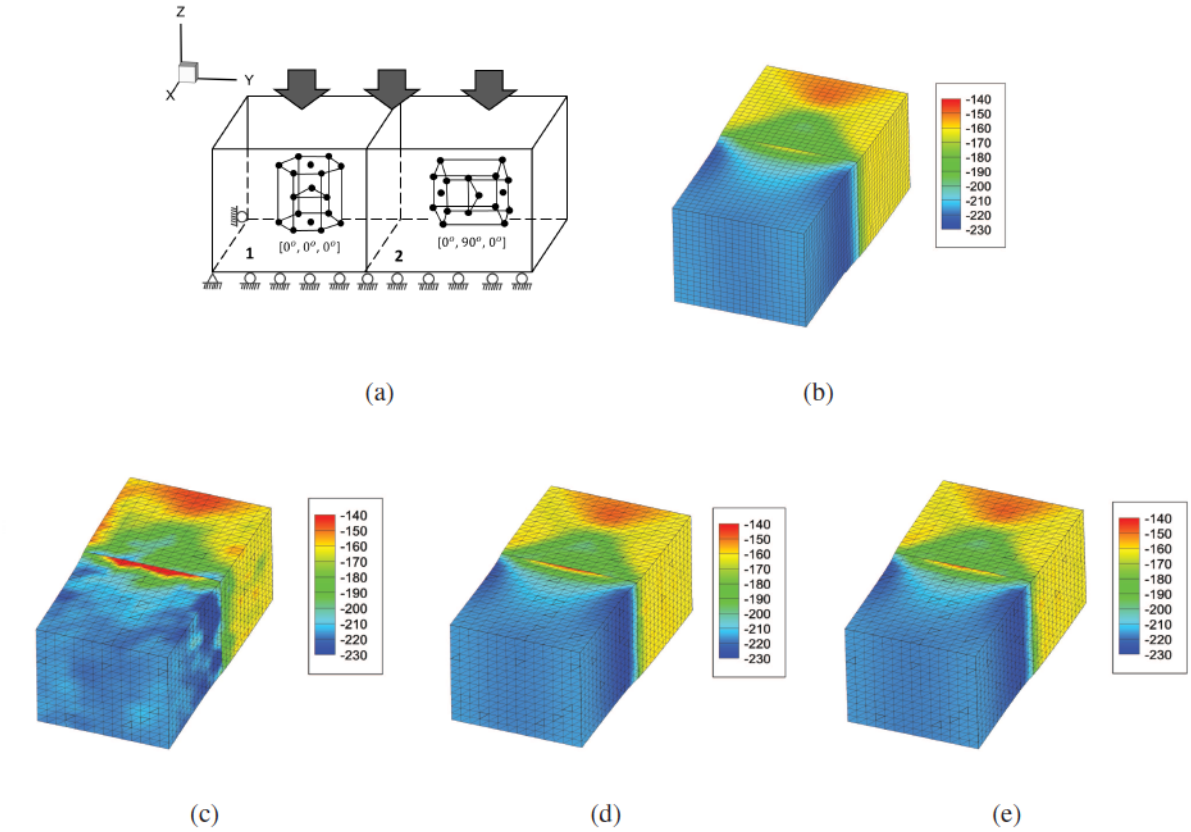

Figure 3.8: (a) Illustration of the boundary conditions and the crystallographic orientations for the constant strain rate compression test on a magnesium AZ31 alloy bicrystal; distribution of loading direction stress σ_{zz} in the deformed configuration at 5% strain using simulation results of: (b) 8-noded hexagonal element using B-bar method with a mesh of 18081 nodes, (c) standard TET4 element with a mesh of 11862 nodes, (d) LIB element with a mesh of 11862 nodes, and (e) FP element with a mesh of 11862 nodes.

This example shows that even for uniaxial loading, volumetric locking is observed in crystal plasticity FE analysis. This can be introduced by the lattice structure among grains rather than by external loading. From Schmid factor analysis, plastic deformation is expected to occur primarily on $\langle c+a \rangle$ pyramidal plane in crystal 1 and $\langle a \rangle$ prismatic plane in crystal 2. However dislocation glide may also occur on other slip systems close to the grain boundary as the local stress state deviates from average uniaxial stress state due to the lattice mismatch and plastic strain incompatibilities. Seven different meshes of different density, consisting of 766, 1106, 1583, 2742, 4400, 6421 and 11862 nodes are simulated using the standard TET4, LIB and FP elements. The reference solution, shown in figure 3.8b, is obtained by solving a mesh of 18081 nodes using the 8-noded hexahedral element with the B-bar stabilization method. The distribution of loading direction stress σ_{zz} using the standard, LIB and FP elements are shown in figures 3.8c-3.8e respectively. Very high stress concentration is observed at the grain boundary using standard TET4 element compared to the solution by other stabilized elements. Additionally, the result of the TET4 element shows a non-smooth distribution of the local stress, which is not seen for solutions with the LIB and FP elements. The error in the stress is evaluated as the $L2$ norm of the difference with the reference solution, expressed as:

$$\|e\|_{L2} = \frac{\left[\int_{\Omega} \left(\sigma_{ij} - \sigma_{ij}^{ref}\right)\left(\sigma_{ij} - \sigma_{ij}^{ref}\right) d\Omega\right]^{\frac{1}{2}}}{\left(\int_{\Omega} \sigma_{ij}\sigma_{ij} d\Omega\right)^{\frac{1}{2}}} \tag{3.33}$$

where $\boldsymbol{\sigma}$ and $\boldsymbol{\sigma}^{ref}$ are the solution and reference Cauchy stress respectively. The corre-

sponding error plots for different elements with increasing mesh densities are shown in figure 3.9. The average convergence rate for LIB and FP elements is 0.75. For CPFE analysis, the LIB and FP elements exhibit similar results with much smaller errors compared to the standard TET4 element.

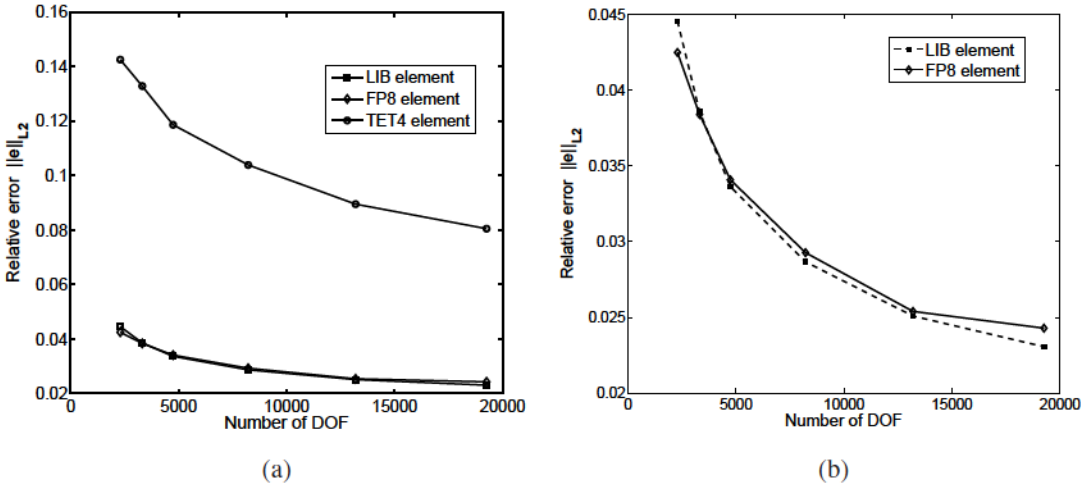

(a) (b)

Figure 3.9: (a) Error plot of $\|e\|_{L2}$ with increasing degrees of freedom (DOF). (b) zoomed-in view of (a) to compare the error between FP8 element and LIB element

For further stability analysis, the hydrostatic stress at the grain boundary is plotted in figure 3.10. Unrealistically large hydrostatic stresses are observed with conventional TET4 elements. With plastic incompressibility, the non-zero volumetric strain at each integration point gives rise to a large strain energy that results in a large hydrostatic stress. LIB and FP elements significantly alleviates this problem and exhibit a saturation of the hydrostatic stress, which is consistent with the results of the stabilized 8-noded hexahedral element. In contrast, all element formulations yield nearly the same values of the von Mises stress,

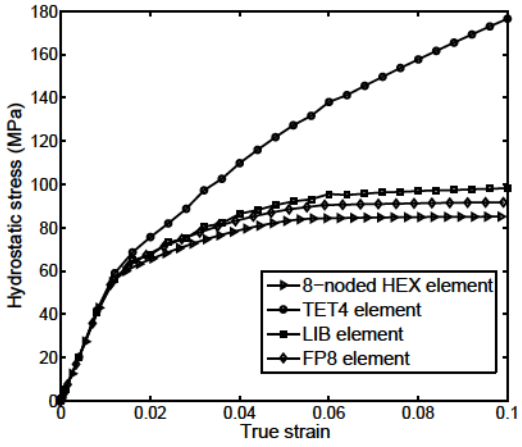

Figure 3.10: Evolution of maximum of local hydrostatic stress with strain for different element formulations.

as the deviatoric strain energy is nearly unaffected by volumetric locking for this bicrystal problem. In real polycrystalline microstructures however, the shear stress components are also affected by volumetric locking due to the existence of complex grain boundary patterns.

3.3.4 Bending of a polycrystalline cantilever beam

The effect of volumetric locking on bending of a polycrystalline $Ti6Al$ cantilever beam is investigated in this example. The beam is $2000\mu m$ long with a square cross-section of $300 \times 300\mu m^2$, as shown in figure 3.11a. It consists of 327 grains that are cumulatively discretized into 276544 TET4 elements as shown in figure 3.11a. All 3 translational degrees of freedom are fixed on the left end. A linearly increasing shear traction is imposed in the Y direction on the right end to bend the beam mainly about the Z direction.

Distribution of the effective plastic strain by the different element formulations are plot-

ted in figure 3.11. At early stages of deformation, the response is primarily elastic and all element formulations predict nearly the same tip deflection with almost no locking. With increasing deformation, the material starts to deform plastically near the fixed end as seen in figure 3.11b. This leads to formation of a plastic hinge near the clamped end, where the maximum bending moment occurs. As the material undergoes more plasticity near the fixed end further enhances the plastic hinge mechanism and overall rotation is facilitated. Volumetric locking causes less plastic strain with TET4 element than the other two leading to significant under-prediction of the tip deflection.

Figure 3.12 shows the distribution of hydrostatic stress on the XY face of the beam. A checkerboard type pattern is observed for the analysis done by TET4 elements near the fixed end of the beam where plastic strain is significant. These fluctuations are nearly eliminated in the results from the FP and LIB elements.

3.3.5 Constant strain-rate deformation of a polycrystalline microstructure

CPFE analysis, using different element formulations is performed to investigate the effects of volumetric locking on the response of a polycrystalline microstructure under constant rate of deformation. The $680 \times 680 \times 680 \mu m^3$ $Ti6Al$ polycrystalline microstructure consists of 540 grains. A constant rate of deformation $\dot{\epsilon} = 9 \times 10^{-5} s^{-1}$ is applied in the [001] direction as shown in figure 3.13 corresponding to the pole figures. Figure 3.14a shows the results

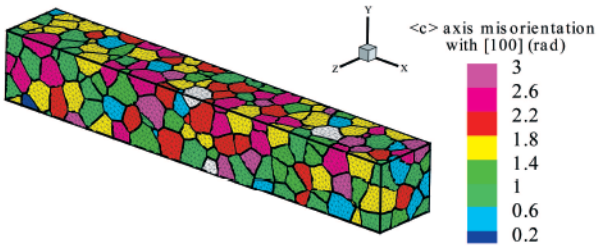

(a)

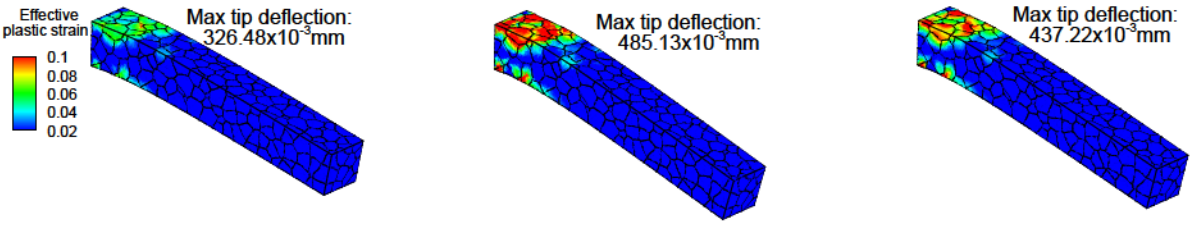

(b)

Figure 3.11: (a) Schematic of a 327-grain $Ti6Al$ polycrystalline beam showing misorientation distribution; (b) distribution of effective plastic strain for different element formulations after $324s$

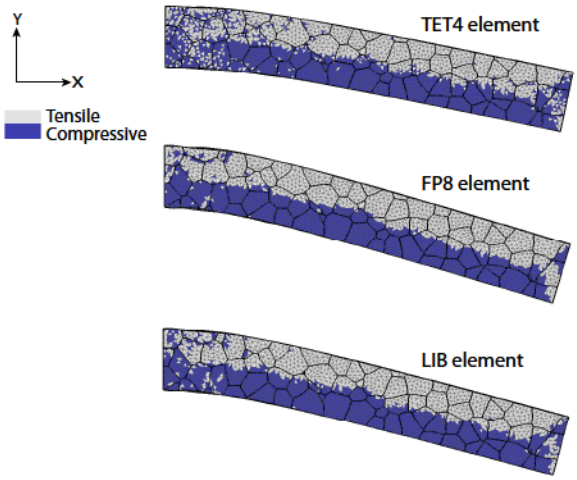

Figure 3.12: Distribution of hydrostatic stress on XY face of the beam after 324s using different element formulations.

of simulations using different element formulations. In the elastic regime, all formulations predict the same macroscopic response since the material is elastically compressible. With increasing plasticity, response obtained from TET4 element suffers volumetric locking and shows a stiffer response with a higher rate of hardening in comparison with the response predicted by FP8 and LIB elements.The FP8 and LIB elements predict almost the same response. The distribution of hydrostatic stress after 800s, corresponding to nearly %7 strain, in figure 3.14b clearly shows that TET4 element tends to over-predict hydrostatic stresses. It is observed that the FP8 and LIB elements perform equally well and their results have the same distributions.

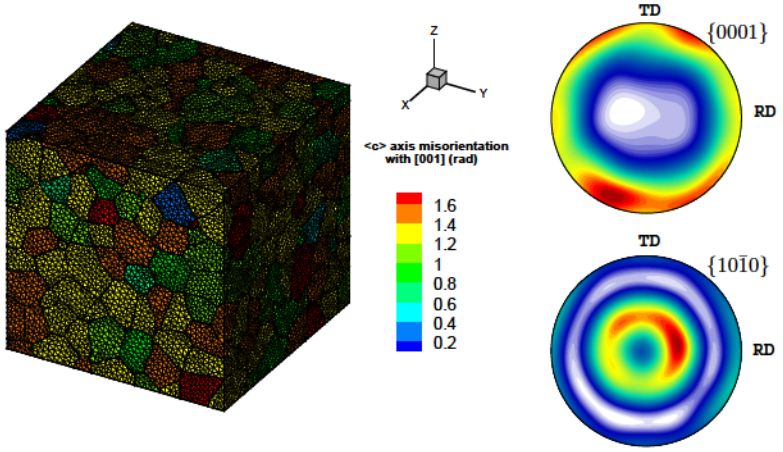

(a) (b)

Figure 3.13: A 540-grain polycrystalline microstructure of Ti6Al alloy discretized into 583432 TET4 elements.

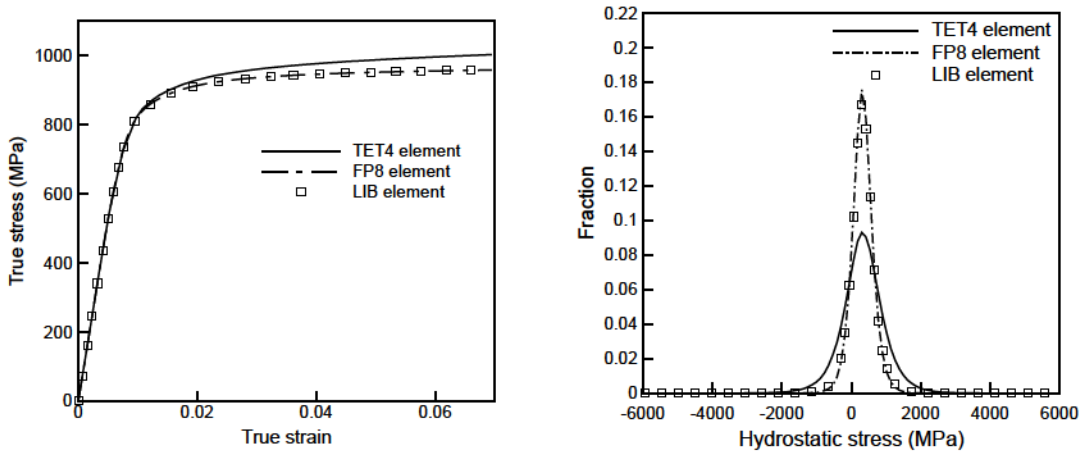

(a) (b)

Figure 3.14: Comparison of (a) loading-direction true stress-strain response of polycrystalline Ti-6Al alloy under uniaxial tension in the [001] direction, and (b) distribution of hydrostatic stress in the polycrystalline microstructure after 800s, by the different methods.

3.4 Computational Efficiency with Different Element Formulations

Methods of alleviating volumetric locking in either the LIB or FP elements result in more computational costs in comparison with the conventional TET4 element. The CPU time spent for LU factorization of the tangent stiffness matrix and element-level calculations, including computation of residual force and tangent stiffness matrix, are compared for efficiency of the three formulations. Only one processor is used in all the simulations to rule out the effects of improper parallel computing algorithms, if any, on the reported CPU times. LU factorization is carried out using the SuperLU package [93].

A small *Ti6Al* microstructure with 14 grains that is discretized into 2141 elements is considered for the efficiency study. The CPU times expended for LU factorization and element-level calculations for one iteration in the Newton-Raphson solution scheme are compared in table 3.4. The CPU time spent on LU factorization for locking-free elements is more than that for TET4 elements. This is due to the fact that more degrees of freedom are connected to one another in FP and LIB formulations. This makes the bandwidth of the tangent stiffness matrix larger and more vector operations are needed for LU factorization. The factorization for FP elements takes less time than LIB elements since the bandwidth of the former tangent stiffness matrix is generally smaller. In regard to element-level calculations, the FP elements take slightly longer time than TET4 elements.

This is mostly due to calculating the modified deformation gradient in the patch, calculating and assembling the cross-stiffness matrix K^{KJ} in equation (3.29). The LIB elements take significantly longer time to perform element-level calculations since each element is divided into 4 sub-tetrahedrons where the constitutive law is solved. The number of constitutive updates and assembly processes increases the CPU times for the LIB element. From this study, it is deemed that FP elements are preferred over LIB elements in CPFE simulations from an efficiency point of view.

Element Formulation	Time spent for LU factorization (s)	Time spent for element-level calculations (s)
TET4	0.098	0.832
FP	0.145	1.175
LIB	0.186	27.072

Table 3.4: Comparison of CPU time for different element formulations.

3.5 Conclusion

This Chapter examines three methods to overcome volumetric locking in 3D constant strain tetrahedral (TET4) elements and augments them for crystal plasticity finite element or CPFE analysis of polycrystalline metals and alloys. The three methods include node-based uniform strain (NUS) element, the locally integrated B-bar (LIB) element and the F-bar patch (FP) based element that incorporate stabilization patches for selectively integrating parts of the constitutive relations. The LIB element splits the gradient operator matrix into isochoric and volumetric components and then reduces the incompressibility constraint by smoothing the volumetric component within the patch. The FP element changes the

deformation gradient tensor at each integration point to a volume-averaged value within each patch. Both the LIB and FP elements provide stabilized solution without introducing spurious low-energy modes as with the NUS element. These elements also do not require isotropy in the material tangent stiffness tensor and can be applied to any constitutive law. Both of these elements pass the element patch test.

Various finite deformation CPFE simulations are conducted to investigate the performance of LIB and FP elements in eliminating volumetric locking. Bending simulations of a nearly incompressible elastic bar show that both the LIB and FP elements provide satisfactory results and converge to the reference solution. The FP element is capable of providing slightly better result than the LIB element for an optimal patch size. CPFE simulations of polycrystalline magnesium and titanium alloys under various loading modes reveal that these elements can relieve volumetric locking present with linear TET4 elements. The effects of locking are dominant near grain boundaries and cause locally high hydrostatic stresses and low plastic strains. The LIB and FB elements stabilize the displacement, local stresses and plastic strains, and GND distributions in CPFE analyzes. Linear convergence rates are seen in bicrystal compression tests. In modeling micro-twin induced material failure in polycrystalline microstructures of AZ31 alloy, significantly premature micro-twin nucleation time is predicted by linear TET4 elements. This can be overcome by using the LIB or FP elements in CPFE analyzes. Finally, when computational efficiency is considered the FP element outperforms the LIB element with a considerably lower simulation time.

The fact that LIB element performs constitutive updates once for each sub-tetrahedrons increases the number of Gauss points and slows down the simulations. From both accuracy and efficiency consideration, the FP element is deemed more suitable for stabilized CPFE analysis.

Chapter 4

Calibration and Validation of CPFE Model for Mg Alloy AZ31

The CPFE model for Mg alloys developed in chapter 2 are calibrated and validated in this chapter. The model parameters are first calibrated in single crystal tests by comparing to experimental data of pure Mg. When to apply to simulations of Mg alloy AZ31, the parameters are adjusted for the difference in alloy component elements. A Hall-Petch relation is incorporated into the model to account for the effect of grain boundaries which reduce the mean free path of dislocation slip and increase the shear resistance. The image-based virtual microstructure is constructed using the software Dream.3d [94] by matching the statistical distributions and correlations of the microstructure features in the AZ31 experiment samples examined by electron back-scattered diffraction (EBSD) sectioning. The simulation results of the virtual microstructure are compared to experimental data.

4.1 Calibration of Constitutive Parameters from Single Crystal Mg Experiments

Constitutive parameters to be calibrated in the low-symmetry *hcp* crystals include: (i) reference slip system shearing rate $\dot{\gamma}_0^\alpha$, (ii) initial shear resistance $s_{*,0}^\alpha$, (iii) hardening rate parameters h_{ref}^β and r, (iv) reference saturation stress s_{sat}^β, and (v) parameters related to GND hardening c_1, c_2 and c_3. Results of experiments and simulations in [30] suggest major dislocation activities in the basal $\langle a \rangle$, prismatic $\langle a \rangle$ and 2nd order pyramidal $\langle c + a \rangle$ slip systems for various deformation modes. This results in a total of 18 parameters to be calibrated. The strain-rate sensitivity parameter m in equation (2.12) and elastic constants have been experimentally measured in [95] and listed in table 4.1. From a sensitivity analysis similar to that in [52], the parameters to-be calibrated are identified to affect three experimentally observed macroscopic properties, viz. the initial macroscopic yield strength (σ_y), post yield slope (H) and macroscopic saturation stress (σ_s). For each property, a genetic algorithm-based minimization is applied to determine constitutive parameters from the experimental data. The corresponding minimization statement and objective function [96] are:

$$minimize \sum_{i}^{M} \left(\sum_{j=1}^{N} \left(\Phi_k^{experiment} - \Phi_k^{simulation}(X_k) \right)^2 \right) \qquad \forall k = 1, 2, 3 \tag{4.1}$$

In this equation, Φ_k, $(k = 1, 2, 3)$ corresponds to an experimentally observed property. For example, $\Phi_1 = \sigma_y$, $\Phi_2 = H$ and $\Phi_3 = \sigma_s$. Each property Φ_k is affected by a group of constitutive parameters X_i, $i = 1, 2, 3$, i.e. $\Phi_i = \Phi_i(X_i)$. The constitutive parameter groups are: $X_1 = [s^{\alpha}_{*,0}, \dot{\gamma}_0]$, $X_2 = [h^{\alpha}_{ref}, r]$ and $X_3 = [s^{\alpha}_{sat}]$ is sensitive to ϕ_3. M corresponds to the number of comparison experiments and N is the number of data points from each experimental result. Three experimental sets are selected for calibration using equation (4.1) and hence $M = 3$. These experiments are all conducted at room temperature under quasi-static strain-rates on bulk samples of single crystal pure Mg with nearly 100% purity. They are:

- Uniaxial compression test at 0.00016/s strain-rate along [0001] axis in [97]; Loading orientation maximizes the resolved shear stress on 2nd-order pyramidal $\langle c + a \rangle$ slip system.
- Uniaxial tension at 0.00006/s strain-rate along $\left[1\bar{1}20\right]$ direction in [98]; Loading orientation maximizes the resolved shear stress on the prismatic $\langle a \rangle$ slip system.
- Tension along $\left[2\bar{1}\bar{1}2\right]$ direction, followed by compression along the normal direction to the extruded sheet plane at 0.0002/s strain-rate in [99]; Loading orientation maximizes the resolved shear stress on the basal $\langle a \rangle$ slip system.

Each of the three experiments correspond to a crystallographic orientation that favors only one slip system. Their loading orientations [0001], $\left[1\bar{1}20\right]$ and $\left[2\bar{1}\bar{1}2\right]$ are selected to maximize the resolved shear stress on the 2nd-order-pyramidal $\langle c + a \rangle$, prismatic $\langle a \rangle$ and basal

$\langle a \rangle$ slip systems, respectively. Results of calibration are shown in figure 4.1 and the values of the calibrated parameters are given in table 4.1. Note that the single crystal experiment in figure 4.1 had stopped before reaching the saturation regime, as opposed to the polycrystal-based experiments in [100]. Consequently the value of s^{α}_{sat} cannot be calibrated at this step, but should be determined directly from polycrystalline simulations. The figure 4.1 shows that the crystal plasticity model can capture the anisotropic plastic yielding and hardening effects in different loading directions very well. The GND parameters are calibrated with polycrystalline AZ31 experiments in selected loading modes as discussed next.

Table 4.1: Constitutive parameters for single crystal pure Mg; subscripts bas, pri and pyr correspond to basal, prismatic and 2nd order pyramidal slip systems respectively.

C_{11} (GPa)	C_{12} (GPa)	C_{13} (GPa)	C_{33} (GPa)	C_{44} (GPa)
59.40	25.61	21.44	61.6	16.4
m	$\dot{\gamma}_0$ (s^{-1})	r		
0.02	0.0023	0.25		
$(s^{\alpha}_{*,0})_{bas}$ (MPa)	$(s^{\alpha}_{*,0})_{pri}$ (MPa)	$(s^{\alpha}_{*,0})_{pyr}$ (MPa)		
1.4	32.5	42		
$(h^{\alpha}_{ref})_{bas}$ (MPa)	$(h^{\alpha}_{ref})_{pri}$ (MPa)	$(h^{\alpha}_{ref})_{pyr}$ (MPa)		
20	1200	2250		

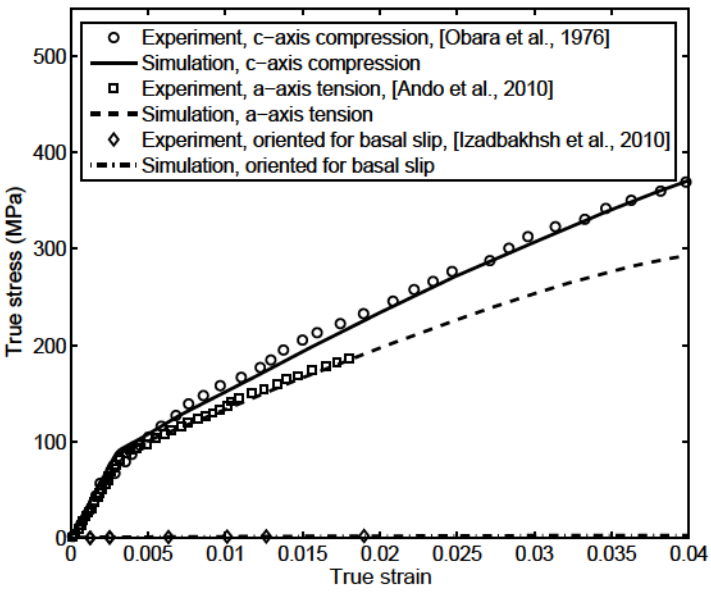

Figure 4.1: Comparing simulation results with calibrated parameters with experimental data for single crystal pure Mg for loading in different directions. The basal slip corresponds to $[2\bar{1}\bar{1}2]$ direction.

4.2 CPFE Simulation of Constant Strain-rate Tests of Polycrystalline AZ31 Alloy

In this example, a crystal plasticity finite element (CPFE) model is developed to simulate response of the polycrystalline AZ31 Mg alloy under constant strain-rate loading conditions. Various steps leading to the overall objective are discussed next.

4.2.1 3D virtual microstructure reconstruction, meshing and mesh convergence

The CPFE simulations are conducted for statistically-equivalent virtual microstructures of the Mg alloy AZ31. These microstructural domains are constructed using the DREAM.3D

software [94] that is based on methods described in [101, 102]. Virtual microstructures are generated by matching morphological and crystallographic statistics with electron back-scattered diffraction (EBSD) data obtained from focused ion beam or FIB-based serial sectioning experiments on the AZ31 alloy in [100, 103]. The first step in virtual microstructure synthesis involves characterization [101], where 3D polycrystalline microstructure data is first assembled from aligned, 2D scanned images in the dual-beam FIB grain segmentation process. Following this, statistics of microstructure descriptors e.g. distribution functions of morphological parameters like grain volume, number of contiguous neighbors, aspect ratio and surface-to-volume ratio, and crystallographic parameters such as orientation, mis-orientation and micro-texture are generated. The correlation between each parameter and grain size is also investigated. The second step involves using the distribution and correlation functions for generating statistically-equivalent synthetic 3D grain structures. A sequence of modules, viz. (i) equivalent ellipsoidal grain generator, (ii) constrained grain packer, (iii) seed point generator, (iv) constrained tessellation tool and (v) crystallographic orientation assignment is invoked for reconstructing virtual microstructures [102]. The collection of these modules and the experimental characterization processes constitute an automated methodology for simulating representative polycrystalline microstructures.

The DREAM.3D code [94] is used to generate a $70\ \mu m \times 70\ \mu m \times 70\ \mu m$ microstructural representative volume element or RVE containing 233 grains of the AZ31 alloy as shown in figure 4.2(a). Fig. 4.3 compares the statistical distributions of two representative microstructural descriptors for the reconstructed virtual microstructure and the FIB-EBSD

generated 3D data respectively. The comparison of grain size (equivalent grain diameter or EGD) distribution in Fig. 4.3(a) shows generally good agreement with the exception at the tails. The larger grains are not adequately represented in this reconstruction. The comparison of distribution of number of contiguous neighbors for different grain-sizes in Fig. 4.3(b), on the other hand, is generally quite satisfactory.

A mesh convergence study is conducted with constant strain tetrahedron (CST) elements prior to simulations with the model. CPFE simulations of the microstructural RVE are conducted with the specimen loaded in uniaxial compression to a total of 2% overall strain, in a direction that is normal to the extruded sheet plane (ND). Fig. 4.4(a) displays the results for two mesh densities, viz. with 190763 and 252562 CST elements respectively. The loading direction stress σ_{33} is plotted along a section parallel to the z-axis at 2% strain. From the convergence of the models with two mesh densities, it is inferred that the CPFE model with 190763 CST elements provides sufficient resolution for simulations in this study.

Furthermore, a convergence study on grain numbers in the RVE is conducted to validate the sufficiency of 233 grains for a meaningful analysis. Two additional virtual microstructure containing 60 and 467 grains has been generated from the aforementioned EBSD-FIB scanning results using DREAM3D. Again simulations of uniaxial compression tests with loading applied along ND direction are performed and the results are plotted in Fig. 4.4(b). The results suggest for the given microstructure statistics the two RVEs with 233 and 467 grains can provided converged results and thus the analysis based 233 grains microstructure is consistent.

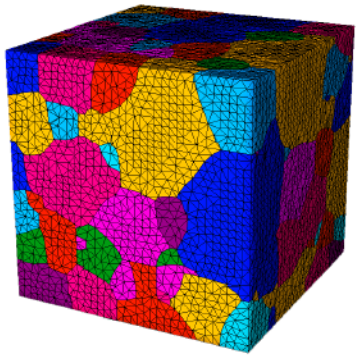

(a)

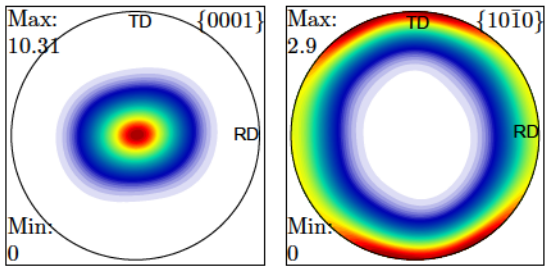

(b)

Figure 4.2: (a) 3D statistically equivalent polycrystalline microstructure reconstructed from EBSD-FIB sectioning images of Mg alloy AZ31, (b) pole figure showing initial texture assigned to the 233 grains microstructure.

4.2.2 Constitutive parameter calibration for AZ31 alloy

Single crystal data for the AZ31 alloy is not generally available in the literature. Hence, the crystal plasticity constitutive parameters are calibrated from experimental data for polycrystalline AZ31 alloy. Starting with the calibrated parameters for pure Mg in section 4.1, only necessary adjustments are made for the AZ31 alloy. For polycrystalline microstructure simulations, it is important to add the effect of the GNDs to the athermal and thermal shear resistances in equations (2.16). Experimental data for the calibration is taken from [100] for quasi-static strain rate and room temperature conditions. The uniaxial compression test normal to the extruded sheet plane direction (ND), which suppresses the formation of commonly observed $\{10\bar{1}2\}$ tension twins, is selected for validation of the dislocation glide model. The resulting constitutive parameters are listed in table 4.2.

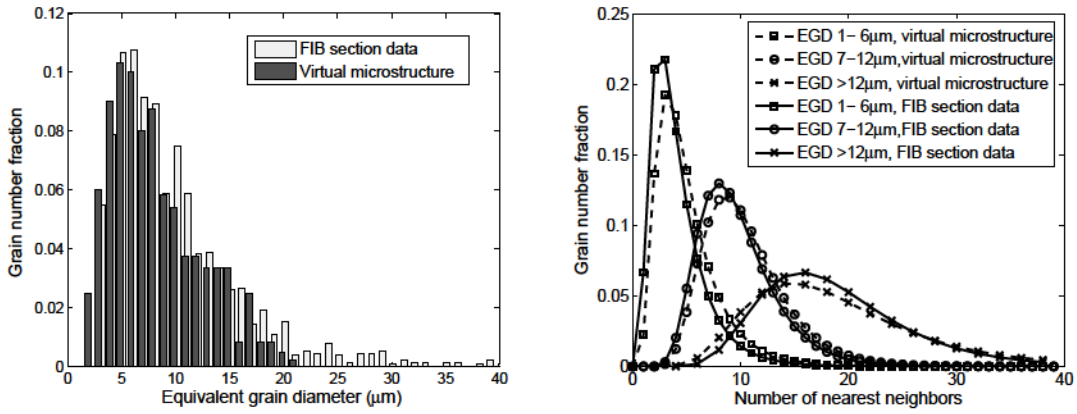

(a) (b)

Figure 4.3: Distribution of (a) equivalent grain diameters (size) and (b) nearest neighbors for different grain sizes, for the reconstructed virtual microstructure and the FIB-EBSD generated 3D data.

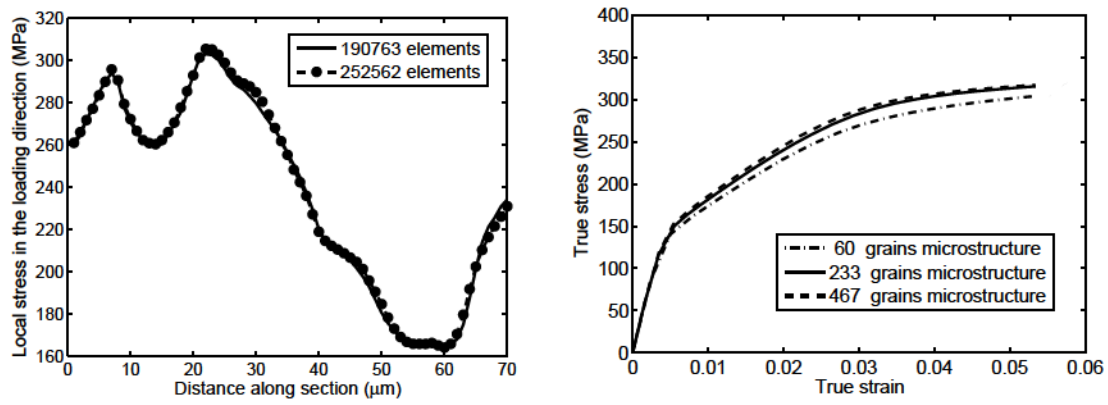

(a) (b)

Figure 4.4: (a) mesh convergence study with respect to the loading direction stress (σ_{33}) along a section parallel to the z-axis at 2% strain. (b) convergence study on number of grains in RVE.

Table 4.2: Crystal plasticity constitutive parameters for the alloy AZ31 with modified parameters from pure Mg to account for different chemical composition; subscripts bas, pri and pyr correspond to basal, prismatic and 2nd order pyramidal slip systems respectively.

C_{11} (GPa)	C_{12} (GPa)	C_{13} (GPa)	C_{33} (GPa)	C_{44} (GPa)
59.40	25.61	21.44	61.6	16.4
m	$\dot{\gamma}_0$ (s^{-1})	r		
0.02	0.0023	0.25		
$(s^{\alpha}_{*,0})_{bas}$ (MPa)	$(s^{\alpha}_{*,0})_{pri}$ (MPa)	$(s^{\alpha}_{*,0})_{pyr}$ (MPa)		
1.4	32.5	45		
$(h^{\alpha}_{ref})_{bas}$ (MPa)	$(h^{\alpha}_{ref})_{pri}$ (MPa)	$(h^{\alpha}_{ref})_{pyr}$ (MPa)	$(s^{\alpha}_{sat})_{bas}$ (MPa)	
20	800	2050	2.4	
$(s^{\alpha}_{sat})_{pri}$ (MPa)	$(s^{\alpha}_{sat})_{pyr}$ (MPa)	c_1	c_2	c_3
90	130	0.1	2.0	1.0

Fig. 4.5(a) compares the results of CPFE simulations with experiments in [100] for the AZ31 alloy. For reference, results of simulations and experiments for single crystal Mg [97] are also plotted in Fig. 4.5(a). The polycrystalline AZ31 simulations have reasonable agreement with experiments. Compared to the single crystal Mg, the polycrystalline alloy exhibits a lower hardening rate (slope). This is primarily due to the effect of texture, i.e. even with a 15 degree misalignment between the c-axis and loading direction, the basal $\langle a \rangle$ Schmid factor (for the easy deformation mode) can reach to > 0.2. The variation of highest basal $\langle a \rangle$ system Schmid factor as a function of the c-axis misorientation from loading direction is shown in fig 5 (b). Due to low activation stress and hardening rate of basal slip in these grains, basal $\langle a \rangle$ slip is activated. This results in lower macroscopic yield stress and hardening. Fig 4.5(a) also showed simulation results in which the contribution of GNDs were excluded from slip system resistance, i.e. the last terms in equation (2.26)

were removed. The comparison shows GNDs has a slight increase on the work hardening rate and macroscopic yield stress. This is due to the fact that GNDs only tend to accumulate close to grain boundaries where the plastic strain incompatibility occurs and only the local stress at such locations is primarily enhanced.

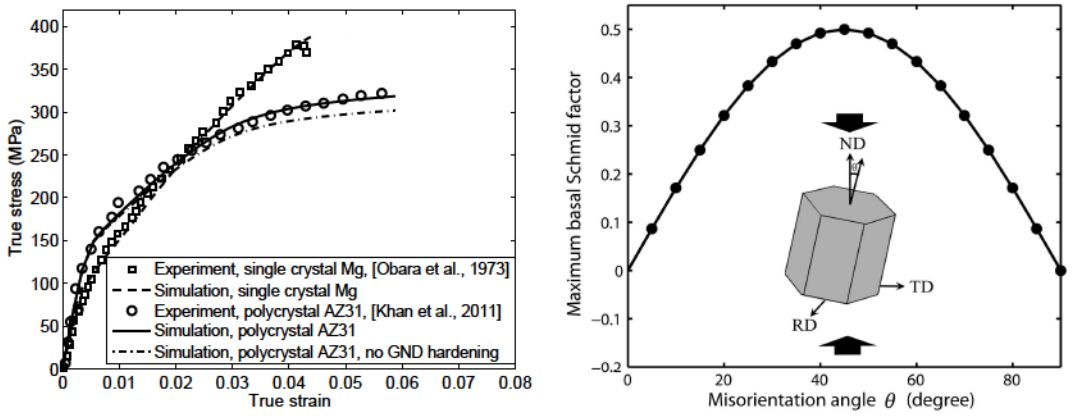

(a) (b)

Figure 4.5: (a) Comparison of simulation and experimental results for loading direction stress-strain response of polycrystalline AZ31 in uniaxial compression; (b) Variation of the highest basal Schmid factor with grain rotation about RD direction (θ is the c-axis misorientation angle from ND direction).

4.2.3 Analysis of CPFEM simulation results for polycrystalline AZ31

Stress and GND density distributions in the polycrystalline microstructure resulting from the CPFE simulations are analyzed in this section. The difference in the basal $\langle a \rangle$ Schmid factor between neighboring grains leads to incompatibility induced GND concentration at grain boundaries. The loading and boundary conditions are shown in figure 4.6a, while figures 4.6b and 4.6c depict the contour plots of the von Mises stress and total GND density at 6% strain respectively. Difference in the slip system deformation resistances or CRSS

and hardening rates, result in locally anisotropic behavior for these *hcp* alloys. Hard grains are nearly $< c + a >$ oriented with their [0001] crystal orientation close to the loading axis. Soft grains on the other hand primarily have the $< a >$ type slip on basal planes. The stress and GND density concentrate close to the grain boundaries, especially near those shared by hard and soft grains with large misorientations. Figures 4.7(a) and (b) show plots of the loading direction true stress and total GND density respectively, along a horizontal line A-A' through the middle section of the microstructure in figure 4.6b. The line passes through soft-hard grain-pairs that see large gradients in the stress and GND values across the microstructure, with concentrations close to grain boundaries. In the soft grain X, the highest Schmid factor for basal slip systems is 0.4287, while that for the $\langle c + a \rangle$ slip systems is 0.2991. Consequently basal slip dominates plastic deformation in the soft grain X, resulting in lower stresses than in other grains. In contrast, in the hard grain Y the highest Schmid factor for basal slip systems is 0.1493, while that for the $\langle c + a \rangle$ slip systems is 0.4864. This causes dominant $\langle c + a \rangle$ slip and high local stresses due to high yield stress and hardening rate of the $\langle c + a \rangle$ systems. The large differences in slip-system flow rates between adjacent grains also cause crystal lattice curvature due to plastic incompatibility near the X-Y grain boundary leading to GND accumulation in figure 4.7(b). For a soft-hard grain pair, GNDs concentrate in the soft grain (figure 4.7(b)), while the peak stresses occur in the hard grain (figure 4.7(a)). The Schmid factor of the last two grains along A-A' are similar and hence the stresses and GNDs do not exhibit concentration at their boundary. The stress concentrations at the soft-hard grain boundaries are responsible for twin nucleation,

studied next.

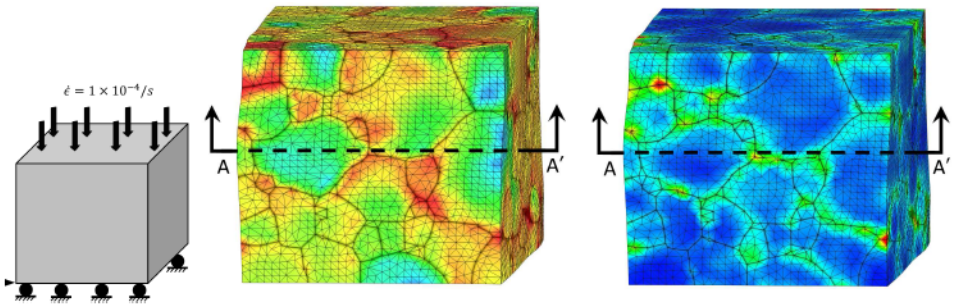

Figure 4.6: (a) Schematic of boundary and loading conditions; and distribution of (b) local stress and (c) geometrically necessary dislocation (GND) density in deformed polycrystalline AZ31 at 6% strain.

4.3 Conclusion

The CPFE model developed in Chapter 2 and 3 is calibrated from pure Mg single crystal experimental data under various loading conditions. The 3D CPFE simulation is conducted on polycrystalline microstructures that have equivalent statistics of morphological and crystallographic characteristics of experimental specimens. The CPFE constitutive model incorporates phenomena from a variety of experimental observations. The model predicts strong material anisotropy and deformation heterogeneity in polycrystalline alloy AZ31. It is able to predict the macroscopic stress-strain evolution as well as the microstructural stress and GND distribution that are consistent with experimental results.

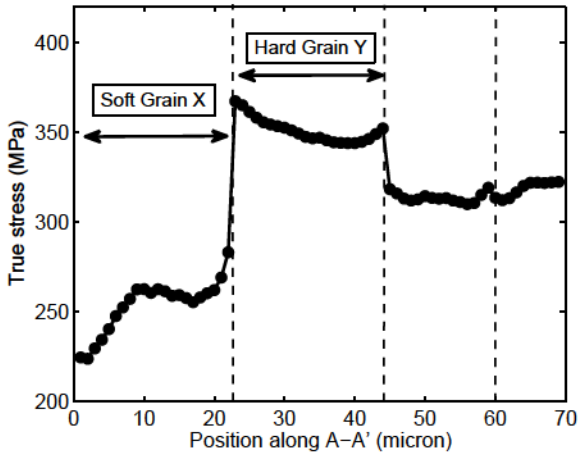

(a)

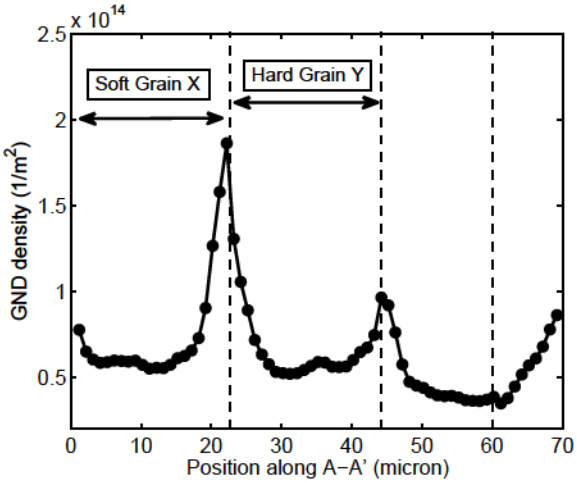

(b)

Figure 4.7: Distribution of (a) true stress in the loading direction and (b) total GND density along a line A-A' passing through a soft-hard grain boundary.

Chapter 5

Micro-Twin Nucleation in CPFE Analysis of Polycrystalline Mg-AZ31

As the first step of a systematic modeling toward the failure prediction of magnesium, this chapter focuses on the modeling the nucleation of $\{10\bar{1}2\}$ type twins which most commonly occurring twins in magnesium. The $\{10\bar{1}2\}$ type twins usually occupy much higher volume fraction than other type twins and has an apparent impact on the mechanical behavior, e.g. changing the hardening rate and improving the ductility. A dislocation-assisted mechanism is assumed for the heterogeneous nucleation of $\{10\bar{1}2\}$ type twins. It involves non-planar dissociation of a sessile $\langle c+a \rangle$ lattice dislocation into n layers of glissile twinning dislocations, leaving behind a residual sessile stair-rod partial dislocation for conserving the Burgers vector. Analytical studies based on elastic dislocation theory and atomistic simulations using molecular dynamic in [40] have shown that such a dissociation process can occur under a sufficiently large applied shear stress on a 2nd order pyramidal $\langle c+a \rangle$ dislocation system $\{\bar{1}2\bar{1}3\}\left\langle 1\bar{2}12 \right\rangle$, schematically showed in figure 5.1. A twin nucleation criterion is constructed based on the energy analysis of dislocation dissociation process in the followings.

5.1 Modeling Micro-twin Nucleation in Polycrystalline Microstructures

The dislocation reaction of a $\{\bar{1}2\bar{1}3\}\left\langle 1\bar{2}12\right\rangle$ sessile dislocation dissociate into twin partial dislocation and stair-rod residual partial dislocation can be expressed as:

$$\mathbf{b}_{ini} \rightarrow \mathbf{b}_{tw} + \mathbf{b}_{r} \tag{5.1}$$

where $\mathbf{b}_{ini} = \frac{1}{3}\left\langle \bar{1}2\bar{1}3\right\rangle$ is the Burgers vector of the initial $\langle c+a\rangle$ dislocation that dissociates into a twin partial dislocation with a net Burgers vector $\mathbf{b}_{tw}$ and a stair-rod dislocation with a Burgers vector $\mathbf{b}_{r}$. The twin partial dislocation is $\mathbf{b}_{tw} = ns\left\langle 10\bar{1}1\right\rangle$ where s is the magnitude of shear on each layer and n is the number of twin layers. DFT calculations and atomistic simulations in [40] have shown that n must be larger than 6 to be stable, and a value $n = 8$ is taken in this study .

Following [38, 40], the present work extends the energetics framework using 3D elastic theory of dislocation to propose a twin nucleation criterion. Prior to dissociation, the initial energy of the system is given by the self-energy of the sessile $\langle c+a\rangle$ dislocation as:

$$E_{ini} = \frac{L}{4\pi}\left[K^{e}_{ini}(b^{e}_{ini})^2 + K^{s}_{ini}(b^{s}_{ini})^2\right] ln\frac{R}{r_0} \tag{5.2}$$

K_{ini} is the elastic energy prefactor for dislocation, which is calculated using the integral method in [42]. The superscript e and s refer to variables related to edge and screw

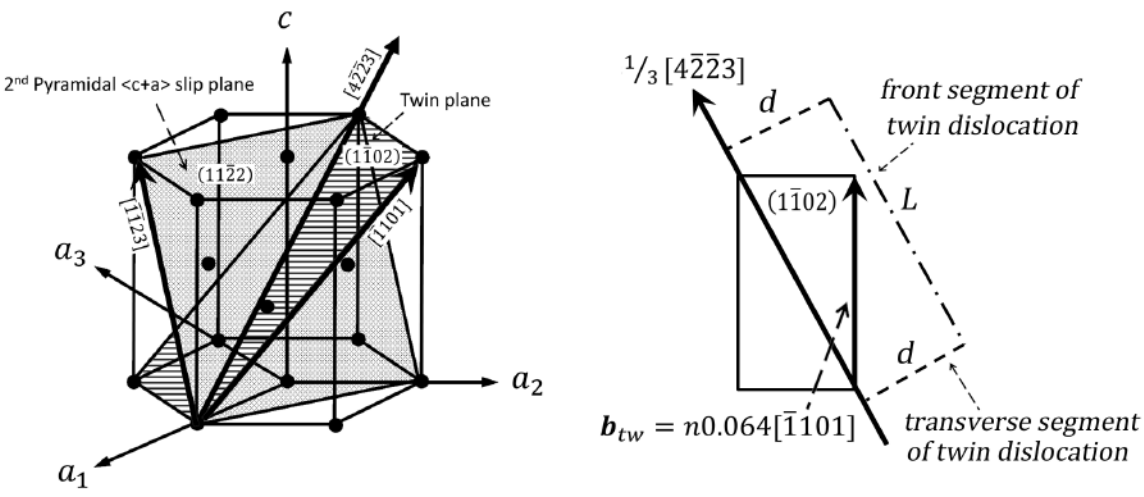

Figure 5.1: Crystallographic lattice systems for $10\bar{1}2$ twin nucleation: (a) $\langle c+a \rangle$ dislocation on $(11\bar{2}\bar{2})$ plane with line direction along $[4\bar{2}\bar{2}3]$ dissociating onto $(1\bar{1}02)$ plane, (b) $\langle c+a \rangle$ dislocation dissociation scheme on $10\bar{1}2$ twin plane.

dislocations respectively. Values of all energy prefactor are listed in table 5.1. The scalar b denotes the magnitude of the Burgers vector, i.e. $b = \|\mathbf{b}\| = \sqrt{(b^e)^2 + (b^s)^2}$. R is the outer radius of the dislocation core taken as 1 μm, while r_0 is the inner radius taken as the atomic distance on basal plane, i.e. $r_0 = 3.196\text{Å}$. L is the initial length of$\langle c + a \rangle$ dislocation and is assumed to be $100nm$. The post dissociation energy of the system is given as:

$$E_F = E_{tw} + E_r + E_{int} + E_{fault} - W_{ex} \tag{5.3}$$

where E_{tw} is the self-energy of the twinning dislocation loop, E_r is the self-energy of the stair-rod dislocation, E_{int} is the interaction energy between the twinning dislocation and stair-rod dislocation, E_{fault} is the stacking fault created by the twinning dislocation, and W_{ex} is the applied external work.

Following the dissociation scheme in figure 5.1 (b), the self-energy of twin partial dislocation E_{tw} is evaluated by summing the line energy of front segment, transverse segment and interaction energy between transverse segments as:

$$\begin{aligned} E_{tw} =& \frac{1}{4\pi}\left\{L\left[K_{tw}^{s,ft}(b_{tw}^{s,ft})^2 + K_{tw}^{e,ft}(b_{tw}^{e,ft})^2\right] + 2d\left[K_{tw}^{s,tr}(b_{tw}^{s,tr})^2\right.\right. \\ &\left.\left. + K_{tw}^{e,tr}(b_{tw}^{e,tr})^2\right]\right\} ln\frac{R}{r_0} - d\left\{K_{tw}^{e,tr}\left[\frac{(\mathbf{b}_{tw}^{e,tr}\otimes\boldsymbol{\xi}^{tr})\cdot(\mathbf{b}_{tw}^{e,tr}\otimes\boldsymbol{\xi}^{tr})}{2\pi} ln\frac{L}{r_0}\right.\right. \\ &\left.\left. + \frac{[(\mathbf{b}_{tw}^{e,tr}\otimes\boldsymbol{\xi}^{tr})\cdot\mathbf{L}][(\mathbf{b}_{tw}^{e,tr}\otimes\boldsymbol{\xi}^{tr})\cdot\mathbf{L}]}{2\pi L^2}\right]\right\} - d\left\{K_{tw}^{s,tr}\frac{(b_{tw}^{s,tr})^2}{2\pi} ln\frac{L}{r_0}\right\} \end{aligned} \tag{5.4}$$

The superscripts ft and tr refer to the front and transverse segments of the twin partial dislocation loop. The length of the front segment of the twin partial dislocation is assumed

to be the same length L as the initial $\langle c+a \rangle$ dislocation. $\mathbf{L}$ is the vector representation of the initial $\langle c+a \rangle$ dislocation line. The length of transverse segment of twinning dislocation is taken as the dissociation distance d. $\boldsymbol{\xi}^{tr}$ is the unit vector of the transverse segment of twin partial dislocation. The first part of equation (5.4) corresponds to the dislocation line energy of twin partial dislocation, while the second part corresponds to the interaction energy between its two transverse segments. No transverse segments are considered for the sessile stair-rod dislocation, and its self-energy is given as:

$$E_r = \frac{L}{4\pi}\left[K_r^e (b_r^e)^2 + K_r^s (b_r^s)^2\right] ln\frac{R}{r_0} \tag{5.5}$$

The formation of the twin partial dislocation and stair-rod dislocation is assumed to govern the twin nucleation criterion:

$$E_{ini} \geq E_{tw} + E_r \tag{5.6}$$

At $d = 0$ and conditions of isotropy, this condition reduce to the classic Frank's rule for dislocation dissociation: $b_{ini}^2 \geq b_{tw}^2 + b_r^2$. However actual dissociation requires a minimum energy at a finite d, i.e. the reaction products must be spatially separated as a result of

internal repulsive forces. The interaction energy E_{int} is given as:

$$E_{int} = -L\,K_{tw}^{s,ft}\frac{(\mathbf{b}_{tw}^{s,ft}\cdot\boldsymbol{\xi}^{ft})(\mathbf{b}_{r}^{s}\cdot\boldsymbol{\xi}^{r})}{2\pi}ln\frac{d}{r_0} - L\,K_{tw}^{e,ft}\left\{\frac{(\mathbf{b}_{tw}^{e,ft}\otimes\boldsymbol{\xi}^{ft})\cdot(\mathbf{b}_{r}^{e}\otimes\boldsymbol{\xi}^{r})}{2\pi}ln\frac{d}{r_0} + \frac{\left[(\mathbf{b}_{tw}^{e,ft}\otimes\boldsymbol{\xi}^{ft})\cdot\mathbf{d}\right]\left[(\mathbf{b}_{r}^{e}\otimes\boldsymbol{\xi}^{r})\cdot\mathbf{d}\right]}{2\pi d^2}\right\} \tag{5.7}$$

where $\boldsymbol{\xi}^{ft}$ is the unit vector of the twin partial front segment and $\boldsymbol{\xi}^{r}$ is the unit vector of the stair-rod dislocation. The first part of equation (5.7) corresponds to the interaction between stair-rod dislocation with the screw component of the twin partial front segment, while the interaction with the edge component is accommodated in the second part.

The formation of twin lamella introduces a stacking fault energy E_{fault}, which has a counter effect to the interaction energy and tends to have the two dissociation products stay close to each other. This is expressed as:

$$E_{fault} = \nu_{tw}dL \tag{5.8}$$

where $\nu_{tw} = 189\,\mathrm{mJ/mm^2}$ is the $\{10\bar{1}2\}$ twin boundary energy. The external work done on twins under a given shear stress τ_{tw} is:

$$W_{ext} = \tau_{tw}b_{tw}dL \tag{5.9}$$

After dissociation, a stable configuration can be reached at a separation distance d_s, when the final energy E_F has reached a saddle point under an applied stress, as shown in figure 5.2.

The equilibrium separation distance d_s can be analytically evaluated from the conditions:

$$\frac{\partial E_F}{\partial d} = 0, \quad \frac{\partial^2 E_F}{\partial d^2} \geq 0, \quad d = d_s \tag{5.10}$$

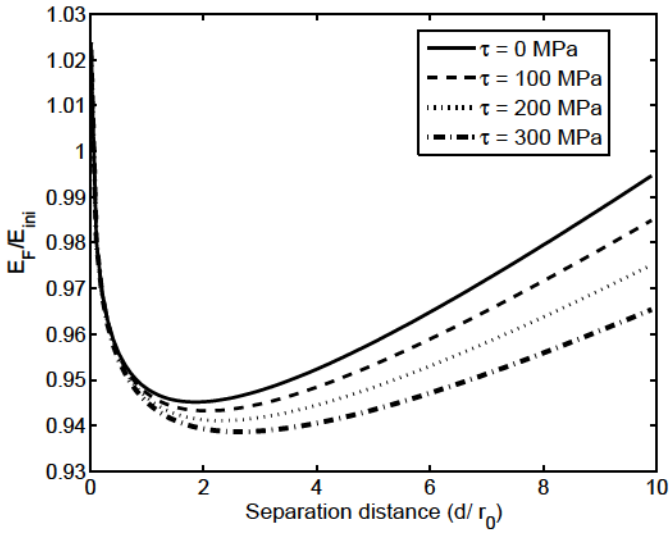

Figure 5.2: Energy associated with twin nucleation event as a function of applied resolved stress and separation distance d between twin partial and stair-rod dislocations.

Stability of the dissociated components needs to satisfy the condition:

$$E_{ini} > E_F\,(d = d_s, \tau_{tw}) \tag{5.11}$$

such that the equilibrium separation is energetically favorable and the process is irreversible.

[38] have argued that there should be a minimum separation distance requirement on d_s, below which the elastic calculation of the dislocation self-energies are not reliable. Also, below this the cores of the initial dislocation, stair rod, and twinning partial dislocations are

not distinguishable. Thus the minimum stable separation distance is assumed to be:

$$d_s > 2r_0 \tag{5.12}$$

Upon satisfying this criterion, it is considered that the dissociation has successfully created the twin partials and faulted areas, and thus a twin nucleus is formed.

Table 5.1: Energy prefactors for Mg (Unit: $\mathtt{mJ/mm^2}$)

$K_{tw}^{e,ft}$	$K_{tw}^{s,ft}$	$K_{tw}^{e,tr}$	$K_{tw}^{s,tr}$	K_{ini}^{e}	K_{ini}^{s}	K_{r}^{e}	K_{r}^{s}
24.7	17.3	24.7	17.3	24.2	17.7	24.5	17.3

5.2 Implementation of Micro-Twin Nucleation Model

The three equations (5.6), (5.11) and (5.12) contributing to the twin nucleation criterion are examined for each of the six $\{10\bar{1}2\}$ twin variant planes. The dissociation energy components are evaluated from equations (5.3), (5.4), (5.5), (5.7), (5.8) and (5.9) For estimating the energy terms, it is necessary to know characteristics of each dislocation segment, viz. the dislocation line length L, the screw and edge components of the initial dislocation line, stair-rod dislocation and twin partial loop. These are estimated from known initial dislocation line direction and dissociation configuration, shown in figure 5.1. For a dislocation with unit line vector $\boldsymbol{\xi}$ and Burgers vector $\mathbf{b}$, the edge and screw components of its Burgers vector can be found as:

$$b^e = (\mathbf{b} \otimes \mathbf{n}) \cdot \boldsymbol{\xi} \quad \text{and} \quad b^s = \sqrt{\|\mathbf{b}\|^2 - b^{e2}} \tag{5.13}$$

where **n** is the slip plane normal. Equation (5.13) is used to compute the screw and edge components of the $\langle c+a \rangle$ dislocation, twin partial and stair-rod dislocations in the energy equations. The stable separation distance d_s in equation (5.10) is derived to be:

$$d_s = \frac{L\left[\frac{K_{tw}^{s,ft}\left(\mathbf{b}_{tw}^{s,ft}\cdot\boldsymbol{\xi}^{ft}\right)\left(\mathbf{b}_r^s\cdot\boldsymbol{\xi}^r\right)}{2\pi} + \frac{K_{tw}^{e,ft}\left(\mathbf{b}_{tw}^{e,ft}\otimes\boldsymbol{\xi}^{ft}\right)\cdot\left(\mathbf{b}_r^e\otimes\boldsymbol{\xi}^r\right)}{2\pi}\right]}{\frac{1}{2\pi}\left[K_{tw}^{s,tr}\left(b_{tw}^{s,tr}\right)^2 + K_{tw}^{e,tr}\left(b_{tw}^{e,tr}\right)^2\right] ln(\frac{R}{r_0}) - F_{tr} + \nu_{tw}L - \tau_{tw}b_{tw}L} \tag{5.14}$$

where

$$\begin{aligned} F_{tr} = \quad & K_{tw}^{e,tr}\left\{\frac{1}{2\pi}(\mathbf{b}_{tw}^{e,tr}\otimes\boldsymbol{\xi}^{tr})\cdot(\mathbf{b}_{tw}^{e,tr}\otimes\boldsymbol{\xi}^{tr})ln\frac{L}{r_0} + \frac{1}{2\pi L^2}[(\mathbf{b}_{tw}^{e,tr}\otimes\boldsymbol{\xi}^{tr})\cdot\mathbf{L}]\right. \\ & \left.[(\mathbf{b}_{tw}^{e,tr}\otimes\boldsymbol{\xi}^{tr})\cdot\mathbf{L}]\right\} + K_{tw}^{s,tr}\left[\frac{1}{2\pi}(b_{tw}^{s,tr})^2 ln\frac{L}{r_0}\right] \end{aligned}$$

For each twin variant, the probability of dissociation from six $\{\bar{1}2\bar{1}3\}\left\langle 1\bar{2}12\right\rangle\langle c+a\rangle$ lattice dislocations is considered. Using equations (5.6), (5.11) and (5.12), the criteria governing the formation of a twin nucleus on any twin variant is given as:

$$\begin{aligned} E_{ini} &\geq E_{tw}(d=0) + E_r \quad \text{and} \\ E_{ini} &> E_F(d_s, \tau_{tw}) \;\; \forall \; d_s > 2r_0 \end{aligned} \tag{5.15}$$

5.3 Accurate Modeling of Micro-Twin Nucleation with Locking-Free elements

Simulations of polycrystalline microstructures with the CPFE model with *a-posteriori* evaluation of the micro-twin nucleation criteria is conducted in this section. The effect of element-locking on twin-nucleation twin is examined by comparing the simulation results by linear TET4 elements and locking-free elements, in the aim of emphasizing the role of stabilized CPFE analysis in accurate modeling of material failure.

The CPFE simulation of micro-twin nucleation is conducted on a statistically-equivalent $40\mu m \times 40\mu m \times 40\mu m$ virtual microstructure of the polycrystalline Mg alloy AZ31, as shown in figure 5.4. A test virtual microstructure is constructed using the DREAM.3D software [94] following methods described in [101, 102]. It contains 103 grains with an average grain size of $10\mu m$, and matches morphological and crystallographic statistics with electron back-scattered diffraction (EBSD) data obtained from experiments in [100, 103]. The microstructure is discretized into 113425 tetrahedral elements with 21463 nodes. Displacement boundary conditions at a rate of $0.004\mu m/s$ are applied on the two surfaces in Y-direction, which tend to bend the microstructure about X-axis on Y-Z plane.

CPFE simulations using TET4 element (simulation A), F-bar patch element with a patch size of 8 tetrahedrons (FP8) (simulation B) and LIB element (simulation C) reveal the difference when locking is removed. The predicted twin nucleation is plotted in figure

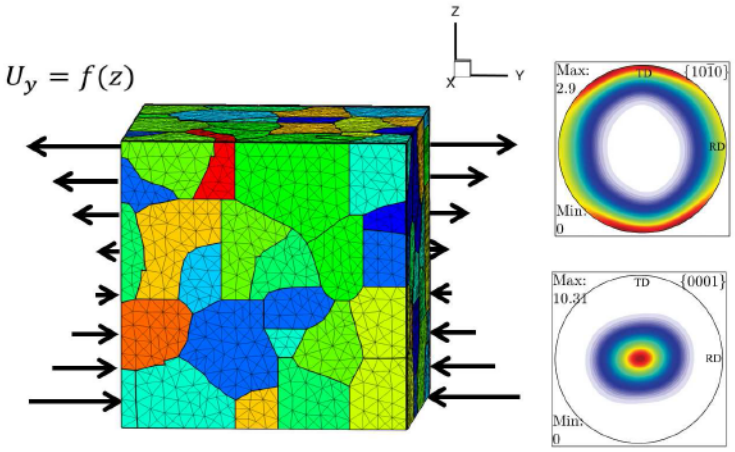

Figure 5.3: Schematic of the applied bending boundary condition to polycrystalline Mg alloy AZ31, and the {0001} and $\{10\bar{1}0\}$ pole figures showing the texture of the polycrystalline microstructure.

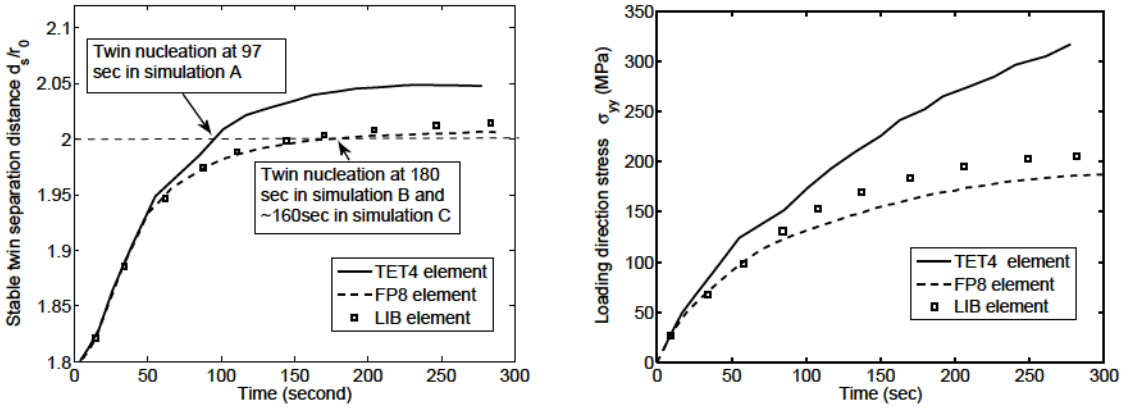

(a) (b)

Figure 5.4: (a) Stable micro-twin dissociation distance as a function of loading time, and (b) loading direction stress at a material point in the center with loading time.

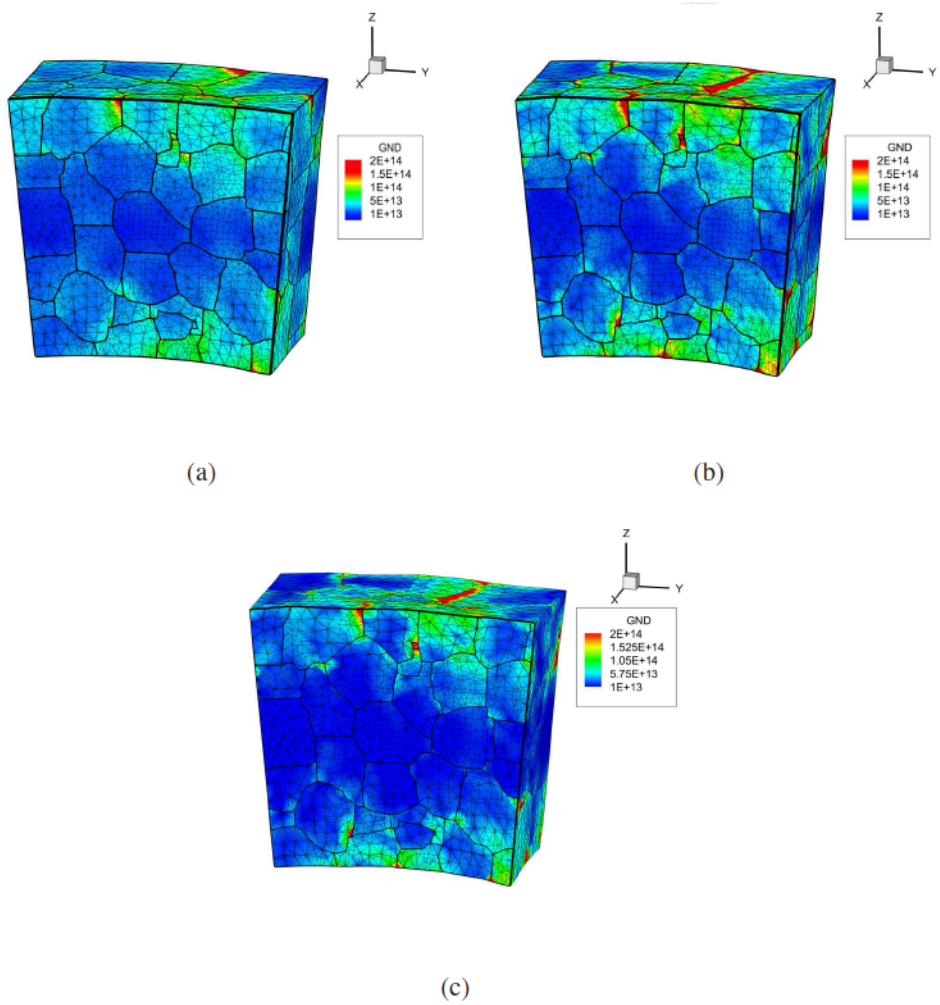

Figure 5.5: GND densities distribution at the middle section after 500s using: (a) TET4 elements and (b) FP8 elements. (c) LIB element

5.4a. The simulation using TET4 elements shows a much earlier twin nucleation time (97 seconds) than that using the LIB element (160 seconds) and FP8 element (180 seconds). This difference is due to the difference in stress states predicted by the two element formulations. For the same level of displacement on the two surfaces, the conventional TET4 element shows a much stiffer response with much higher stresses. This is shown in figure 5.4b where the loading direction stresses at the material point from which twin nucleates are plotted. The non-physical stresses leads to a unrealistic external work in the TET4 elements to separate twin partials from stair-rod dislocations and result in an early twin nucleation prediction. Thus it inaccurately predicts material failure in polycrystalline microstructures. This is clearly remedied with the locking-free elements. It is noticed that the FP8 element shows a slightly higher level of locking removal than LIB elements, due to a better constraint ratio. Comparison of the GND densities in figure 5.5 reveals that the simulation using LIB elements and FP8 elements shows highest GND concentrations close to grain boundaries. Volumetric locking in TET4 elements predicts a stiffer response to bending and constrained lattice distortion, which results in lower GND density.

5.4 Validation of CPFE Twin-Nucleation Model and Study of Microstructural Sensitivity on Twin-Nucleation

Simulations of micro-twin nucleation in polycrystalline microstructures are conducted in this section to validate the model and for insights on the underlying mechanisms. Comprehensive studies on the effects of microstructural statistics on micro-twin nucleation in

Mg alloys have been performed in [1, 104]. Their statistical analysis involves large experimental data sets (approximately 2340 grains) collected from 42 EBSD scans at different locations of the sample using an FEI XL30 field emission gun scanning electron microscope (FEG-SEM) at 20kV with a 1 μm step size. The data is analyzed using an automated twin characterization method [105]. In the present study, the DREAM.3D code [94] is used to generate two statistically equivalent virtual microstructures (SEVM) with the same distribution of grain size, grain orientation and grain boundary misorientations as in [1]. The two SEVMs contain 255 and 273 grains respectively, for which the grain size, highest twin Schmid factor and misorientation distributions and compared with the experimental set in figures 5.6(a,b,c) respectively. The pole figure of 255 grains SEVM is also provided in figure 5.6(d) to show the initial texture. For CPFEM simulations, the two SEVMs are discretized into 149023 and 150881 four node tetrahedrons, respectively. While the statistics of the SEVMs are generally consistent with that of the experimental data, a small difference is observed due to the relatively small number of grains represented. The two virtual microstructures are used to check the effect of slightly varying statistics on the convergence of simulation results with respect to deformation and twins.

The SEVMs are subjected to compression loading in the transverse direction to the extrusion sheet plane direction (TD). For this direction, nucleation of $\{10\bar{1}2\}$ extension twins are observed in experiments. The response is expected to be significantly different for this and other (e.g. ND) directions due to plastic anisotropy in the *hcp* alloys. A constant strain rate $\dot{\epsilon} = 0.001/s$ is applied at a constant temperature $T = 300K$. The CPFEM

simulations are aimed at predicting the twin nucleation sites and studying their distribution in the polycrystalline microstructure, e.g. the characteristics of grain size, orientation, grain boundary misorientation etc.. Only early stages of deformation, upto 3% strain are considered in these studies, for which experimental data is available.

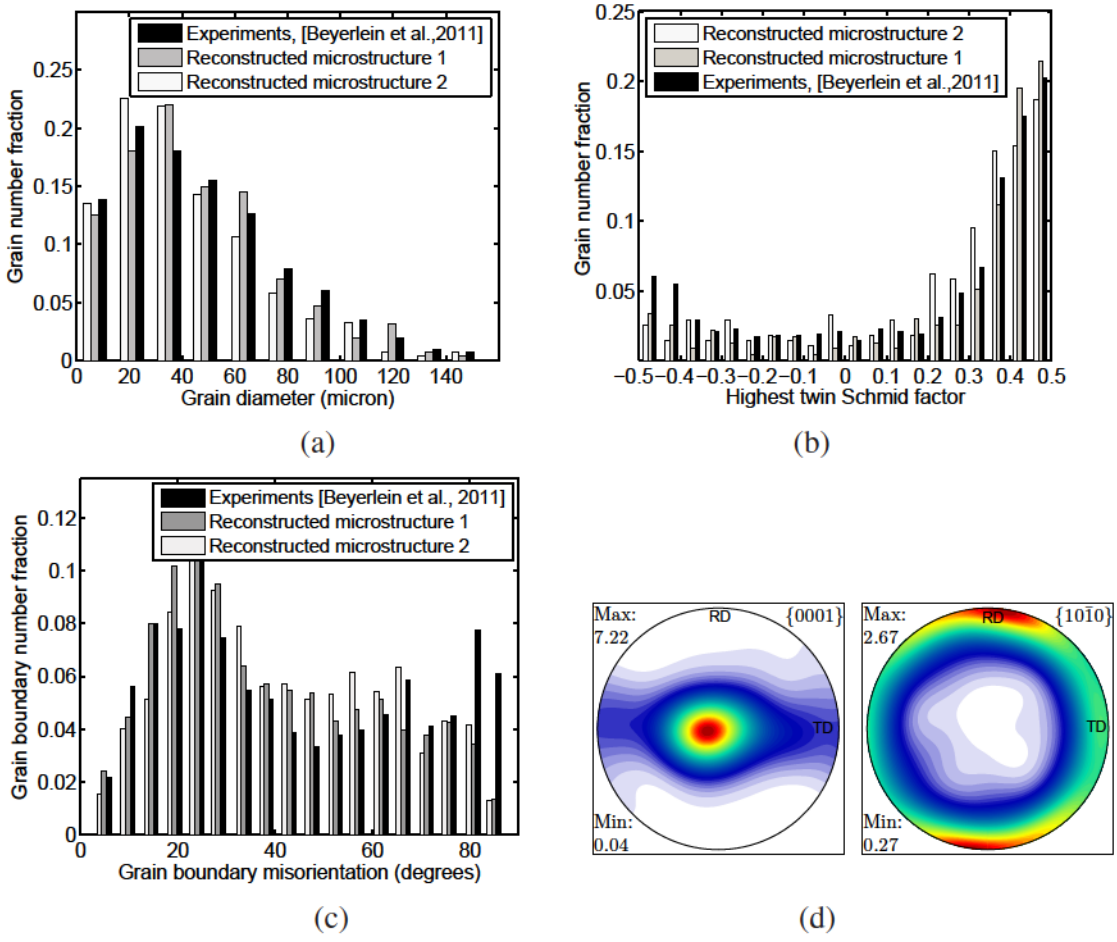

Figure 5.6: Comparing statistical distributions of characteristics of the two statistically equivalent virtual microstructures (SEVMs) with experimental EBSD data-set in [1] for polycrystalline Mg.: (a) grain size distributions, (b) highest twin Schmid factor distributions and (c) grain boundary misorientation distributions. (d) pole figure showing initial texture of 255 grains virtual microstructure.

5.4.1 Identification of twin nucleation sites in polycrystalline microstructures

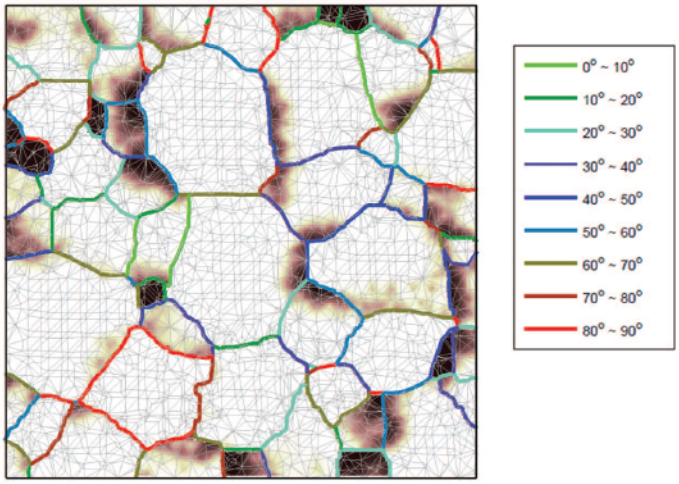

Figure 5.7: A section of the virtual microstructure with a contour map of twin nucleation regions at 3% strain. Grain boundaries are color-mapped according to misorientation angles.

Figure 5.7 shows a SEVM section with a map of twin nucleation site distribution at 3.0% strain . Dark regions correspond to those that meet the twin nucleation criteria in equations (5.15). Grain boundaries are characterized in CPFE by the misorientation angle that is calculated using equation (5.16) between each adjacent grain pairs [96, 102] as:

$$\theta = min \left| cos^{-1} \left\{ \frac{tr(\mathbf{g_B g_A^{-1} O}) - 1}{2} \right\} \right| \tag{5.16}$$

Here $\mathbf{g}_A$ and $\mathbf{g}_B$ are the orientation matrices of adjacent grains A and B respectively and $\mathbf{O}$ corresponds to a crystal symmetry operator for *hcp* crystals. Details of this method are given

in [96]. It is possible to characterize twin nucleation sites within each grain relative to different grain boundaries, enabling direct comparison with experiments. Results of CPFEM simulations show that the primary nucleation sites are generally close to grain boundaries and triple grain boundary junctions. This observation is consistent with experimental and simulation results reported in [1, 33]. Atomic scale simulations in [13] have suggested that grain boundaries are most susceptible to twin nucleation for polycrystalline Mg alloys due to dislocation pile-up induced stress concentration and existence of defect structures. Even with a uniform initial defect distribution, the constitutive model in the CPFEM simulations predicts twin nucleation sites that are observed in experiments. This suggests that twin nucleation depends on such factors as high local stress and local defect structures like grain boundaries defects (GBDs) discussed in [1, 13] and sessile $\langle c + a \rangle$ dislocation in this work. The latter defects may dissociate into twin partials under local high stresses, leading to twinning. Without such defects the stress levels required to trigger homogeneous twins are extremely high, close to the theoretical yield stress level. The simulation results show some diffused twin-nucleation regions due to the fact that twin propagation is suppressed in this work.

5.4.2 Effect of grain size

Figure 5.8(a) plots the histogram of twinned grain number fraction as a function of grain size at 3% strain. A grain that contains at least one element where the twin nucleation criteria (5.15) are satisfied is categorized as a twinned grain. The number fraction is

calculated as the ratio of number of twinned grains to the total number of grains in a size range. The simulated results for both the SEVMs are in good agreement with experimental results in [1]. Smaller grains show a lower population of nucleated micro-twins. [106] have suggested as possible reason, a larger critical stress is necessary for twin activation in smaller grains (similar to the Hall-Petch effect for dislocation slip). However size effect is not explicitly included in the present twin nucleation model. [33] have discussed an alternative reason by correlating grain sizes with the number of adjacent grains. Bigger grains have larger grain boundaries and hence more adjacent neighbors. An increase in the number of neighbors raises the probability of finding soft-hard grain boundaries, on which stress concentrations are likely to trigger twin nucleation. Also the probability of finding triple junctions on the grain boundary increases with additional neighboring grains. From this study it can be inferred that for smaller grains, crystallographic orientation has a major influence on twinning, while for bigger grains the soft-hard grain boundaries dominate the twin nucleation process. Grain size does not have a direct effect on twin nucleation. Subsequent studies on crystallographic orientations and grain boundary are performed to investigate this conjecture.

5.4.3 Effect of crystallographic orientation

The Schmid factor of each slip or twin system may be used to represent how favorable is a grain orientation for accommodating plastic shear. The twin variant with a high Schmid factor will have high resolved shear stress and is easier to activate. The histogram of the

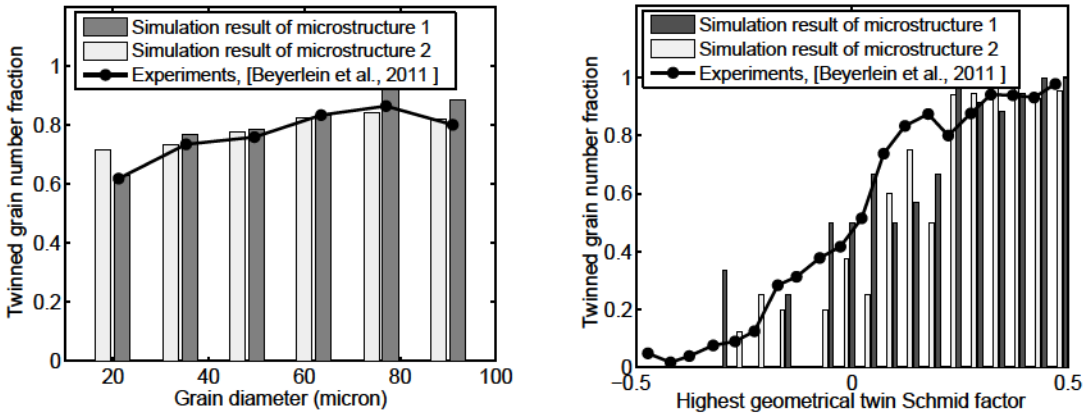

Figure 5.8: Histograms of: (a) number fraction of twinned grains as a function of average grain size, and (b) number fraction of twinned grains as a function of highest geometric twin Schmid factor.

number fraction of twinned grains at 3% strain as a function of the highest Schmid factor is plotted in figure 5.8(b). The highest twin Schmid factor in the x-axis of figure 5.8(b) is defined as the maximum Schmid factor among the six $\left\{10\bar{1}2\right\}$ twin variants. Following [33], this is computed as:

$$SF^{\alpha} = \frac{\mathbf{s}^{\alpha} : \boldsymbol{\sigma}}{||\boldsymbol{\sigma}||} \tag{5.17}$$

where $\mathbf{s}^{\alpha} = \mathbf{m}^{\alpha} \otimes \mathbf{n}^{\alpha}$ represents the Schmid factor of a slip or twin system α and $\boldsymbol{\sigma}$ is the Cauchy stress tensor. Depending on whether $\boldsymbol{\sigma}$ is the local or far-field applied stress, SF^{α} can represent the local Schmid factor (LSF) or the geometric Schmid factor (GSF). The LSF represents the effect of local stresses for a region inside a grain to twin. The GSF, on the other hand, refers to the effect of average stress for a polycrystal aggregate to twin. The comparison experiments in [1] and consequently the simulations use GSF to interpret results in figure 5.8(b).

In general, good agreement is seen for both SEVM simulations with the experiments. The results show that grains with high GSF has a greater probability of nucleating a twin. However, even with a negative GSF, grains have a small probability of nucleating a twin due to locally high stress distributions. Even though some soft grains are not orientated for twin activation, the local stress state at a grain boundary with a hard grain can be favorable for twin nucleation. Consequently the local Schmid factor (LSF), computed using the local stress tensor at each integration point of an element, is plotted in figure 5.9. The results show a clear trend that points with a high LSF have a much higher twin nucleation probability, consistent with the Schmid law [107].

Two key observations may be made from figure 5.9(a). The first is that not all locations with ~ 0.5 LSF will twin, as the magnitude of twin system resolved shear stress may not be high enough for nucleation, especially for points located in the middle of a big grain. The second observation comes from comparing the distribution of GSF in figure 5.6(b) with that of LSF in figure 5.9(a). The number fraction of integration points with LSF ~ 0.5 is much higher than that of grains with GSF ~ 0.5. This is primarily due to grain boundary constraints arising from anisotropy of different slip systems in *hcp* polycrystals. Difference in the extent of basal slip (planes of low CRSS) in neighboring grains with large misorientation can give rise to high local stress near the grain boundary, thus triggering non-basal deformation modes such as twinning and $\langle c + a \rangle$ slip. The evolution of LSF on twin systems and basal systems are plotted in figure 5.9(b) and 5.9(c) respectively. At 0.1% strain the material is in the elastic range and no dislocation slip or twin system is activated. Since

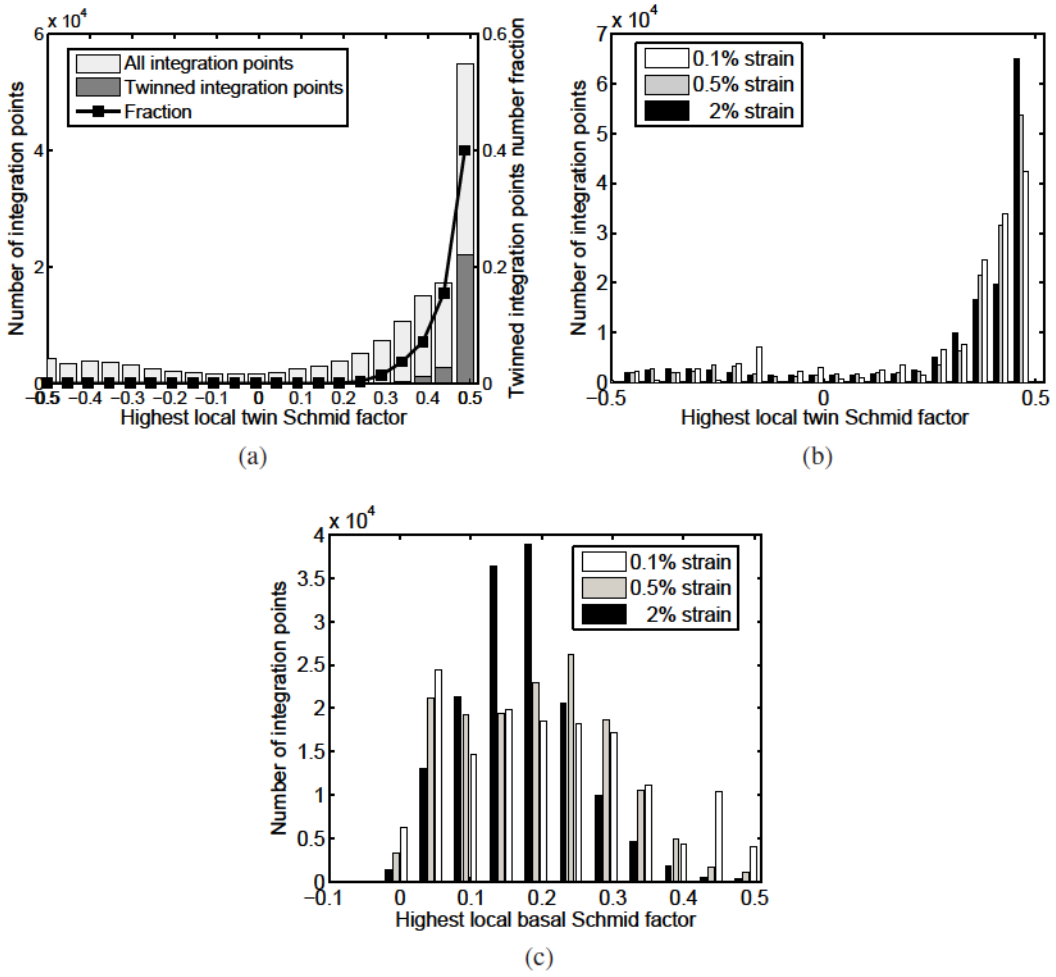

Figure 5.9: Distribution of: (a) all grain/twinned grain as a function of highest local twin Schmid factor, (b) highest local twin system Schmid factor at different strains, and (c) highest local basal slip system Schmid factor at different strains.

elastic anisotropy of Mg alloys is relatively small in comparison with plastic anisotropy, the stress state in each grain at 0.1% strain is close to the macroscopically averaged stress and hence, the distribution of LSF is similar to that of GSF in figure 5.6(b). At 0.5% strain however, basal slip is activated in several grains. The local stress state near grain boundaries start to deviate from the macroscopic stress due to the grain boundary effect, which leads to preferred deformation along the c-axis. This increases the high LSF for twin systems in figure 5.9(b) and decreases the high LSF for basal slips in figure 5.9(c). At 2% strain, when basal slip is activated in most grains, the trend is more pronounced as shown in figures 5.9(b,c). The strong influence of grain orientation on twin nucleation is established in this example. Grains with high geometric twin Schmid factor have a propensity to twin, where locally the twin activation follows Schmid law.

5.4.4 Effect of grain boundary

Element pairs interfacing at the same grain boundary are grouped with a misorientation measure calculated using eqn.(5.16), as depicted in figure 5.7. When an element associated with a grain boundary group has twinned, it is counted as a twinned boundary. The simulation results are shown in figure 5.10. To be consistent with experimental results in [1], the c-axis misorientation angle between two adjacent grains is used for comparison. The simulations show the same trend as experiments, viz. the probability of twin nucleation decreases with increasing c-axis misorientation. However, as observed with simulations in [1, 33], the present CPFE simulations predict a higher probability of twin nucleation

than the experiment. In [1] it has been suggested that the discrepancy may be due to the fact that the experimental data statistics is derived from 2D EBSD sections that are not exactly equivalent to the statistics of 3D grain boundary structure. Also the lack of twin band propagation in the present model leads to diffusive twin nucleation behavior due to over-prediction of other nucleation sites in the same grain with deformation. This adds to the higher values of the number fraction.

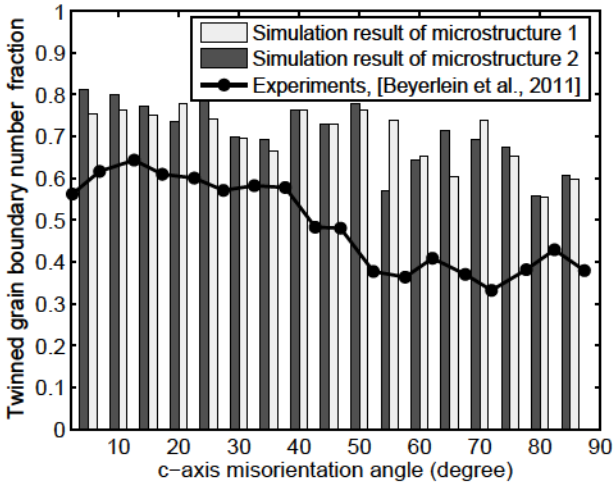

Figure 5.10: Variation of twinned grain boundary number fractions with c-axis misorientation angle.

In general the misorientation angle alone is insufficient for characterizing the influence of grain boundary on response, since it does not include the effect of the loading direction. Without this information, it is not feasible to identify soft-hard grain boundary in *hcp* crystals. As proposed in [108, 109], a Schmid factor based indicator is proposed to

characterize the soft-hard grain boundary (soft-hard grain boundary indicator), defined as:

$$SH(i,j) = \left|SF_{max}^{basal}(j)\right| - \left|SF_{max}^{basal}(i)\right| \tag{5.18}$$

Here $SF_{max}^{basal}(i)$ is the maximum Schmid factor among the three basal slip systems in grain i for a given loading direction. Since soft and hard grains are characterized by high and low basal Schmid factors respectively, a high positive $SH(i,j) > 0$ represents a hard grain i neighboring a soft grain j at a hard-soft grain boundary. Conversely a high negative $SH(i,j) < 0$ value indicates a soft-hard grain boundary on the soft grain side. Figure 5.11(a) plots the distribution of twinned grain boundaries as a function of the $SH(i,j)$ indicator. The number fraction of twinned to total grains shows a monotonic increase with the $SH(i,j)$ indicator, from negative to positive values. Clearly, most twins tend to initiate from the hard grain side of a soft-hard grain boundary. This is because at a soft-hard grain boundary, dislocations tend to accumulate at the soft grain side causing stress concentration on the hard grain side of the grain boundary [56]. Thus for two hard grains with similar orientations, a higher local stress evolves for a softer neighboring grain, with a higher probability of twin nucleation. Introducing the Schmid factor-based $SH(i,j)$ indicator in figure 5.11(a) allows for accounting the side of a hard-soft grain boundary in characterizing twin nucleation, as opposed to figure 5.10 where the misorientation does not discriminate between sides of the grain-boundary.

In figure 5.11(b) the number of soft-hard grain boundaries that have $SH(i,j) \geq 0.2$

is plotted as a function of the c-axis misorientation angle. The majority of soft-hard grain boundaries lie in the misorientation range $10^o - 50^o$. This distribution corroborates observations made in figure 5.10 on a greater propensity of nucleation in the $10^o - 50^o$ misorientation range. It is interesting to note that even a low misorientation angle can constitute a soft-hard grain boundary. For example in figure 4.5(b), even for a 20 degree c-axis misorientation, the basal Schmid factor is higher than 0.3 and extensive basal slip can be activated. Therefore this c-axis misorientation can contribute to a hard-soft grain pair. The basal Schmid factor reaches a maximum at 45 degree c-axis misorientation in figure 4.5(b). In the experimental samples, most grains have their c-axis aligned with the ND direction, for which a high c-axis misorientation angle ($\geq$ 60 degree) exists between two soft grains with the c-axis rotated in opposite directions. These grain boundaries belongs to soft-soft grain boundaries and are unlikely to nucleate twins. This explains the trend of twin nucleation at low angle grain boundaries, observed in simulation and experiments.

5.5 Conclusion

A micro-twin nucleation model that predicts the nucleation of $\left\{10\bar{1}2\right\}$ tensile micro-twins is developed in this chapter. When subject to large applied stresses, twin nucleation is assumed to take place under conditions of dissociation of a sessile $\langle c+a\rangle$ dislocation into a twin partial dislocation and a stair-rod dislocation. The nucleation criteria are governed by the following:

- Initial energy of the system, given as the self-energy of the sessile $\langle c+a\rangle$ dislocation,

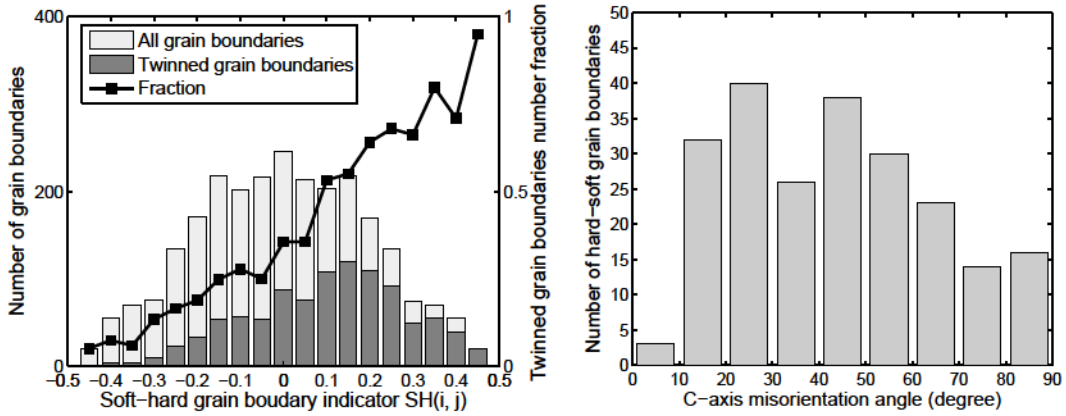

(a) (b)

Figure 5.11: Distribution of: (a) grain boundary number and twinned grain boundary fractions with soft-hard grain boundary indicator $SH(i,j)$ (each grain boundary is considered twice from the soft grain side and hard grain side), and (b) soft-hard grain boundaries ($SH(i,j) \geq 0.2$) with c-axis grain boundary misorientation angle.

exceeds the sum of the self-energies of the twin partial and stair-rod dislocation;

- Initial energy should be greater than the energy required to achieve a stable equilibrium configuration after dissociation, for an irreversible process;

- The dissociation distance should exceed a minimum stable separation distance.

Various CPFEM simulations are conducted to understand the effect of microstructure on twin nucleation. Specifically, the effect of three important microstructural descriptors viz. grain size, crystallographic orientation and grain boundary misorientation is investigated through simulations and validated with experiments. It is found that crystallographic orientation has a strong influence on twin nucleation. Grains with high twin Schmid factor have a much higher chance of twinning, and locally twin activation follows the Schmid law. The CPFEM results, in general, agree well with experiments. The interaction between

neighboring grains and grain boundaries are critical in triggering twins, which tends to nucleate from the hard grain side of a soft-hard grain pair. In conclusion, the CPFEM model is found to be adequate for capturing heterogeneous deformation in the Mg family and for identifying local $\left\{10\bar{1}2\right\}$ tensile micro-twin nucleation.

Chapter 6

Micro-Twin Propagation Model for CPFE Analysis

The rapid micro-twin propagation in hexagonal close packed materials is responsible for the mechanical behavior of tension-compression asymmetry and early brittle-like failure at room temperature. At grain scale, the micro-twin propagation reorients the crystallographic lattice and causes the dislocation slip to occur in twin bands at a different rate from the matrix. The fast twin gliding on twin systems, e.g. $\left\{10\bar{1}2\right\}$ tensile twin in Mg alloys, and the basal slip in an appropriate reoriented twined lattice lead to strain localization inside twin bands and stress concentration close to twin boundaries, which causes crack initiation at twin-grain-boundary and twin-twin intersections [14]. A candidate crystal plasticity law for the propagation of micro-twin is presented in the following. The constitutive law is then numerically implemented into finite element framework to explicitly model the formation of twin bands and deformation heterogeneity.

6.1 Constitutive Model of Micro-Twin Propagation

After a stable micro-twin nucleate, it glides rapidly on twin planes and forms a twin band. The twin band boundaries migrate from one twin plane to the adjacent twin planes and cause an increase in twin thickness[13]. The motion of twin gliding on twin planes is a mixed shear-shuffle process[35]. The shear process causes plastic flows similarly to dislocation slip and is characterized by a Burgers vector b_{tw} on a twin system. After shearing, the twin partial dislocations can not proceed due the high energy barriers. Such a configuration is called pseudo-twin configuration. The corrective non-uni-directional atomic shuffling or re-ordering is then required to place atoms into low-energy symmetric positions, and the allows the twin partial dislocations to glide further. A model based on thermal activation law is derived in [59] to account for the atomic shear-shuffle process. Assume a simple scenario that the process of shear and shuffle are both irreversible, the velocity of twin partial dislocation gliding on a twin plane is expressed as:

$$v_{glide} = f_{shuffle}\lambda_{shear}\left[\exp\left(-\frac{\triangle F - \tau A_P b_{tw}}{K_B T}\right)\right] \tag{6.1}$$

where $f_{shuffle}$ is the frequency of shuffling, λ_{shear} is the shear distance, the term $exp\left(-\frac{\triangle F-\tau A_P b_{tw}}{K_B T}\right)$ is the probability of gliding against the energy barrier. $\triangle F$ is the internal energy barrier, τ is the effective resolved shear stress on twin plane. A_p is the shearing area during the plastic deformation.

The twin increases in thickness when a twin partial dislocation glides on the adjacent twin plane. The growth velocity perpendicular to twin plane can be obtained from a stimulated slip model [110]. The model assumes that there exist dislocation poles in the material which acts as the promoter to transfer twin-partial dislocation from current twin plane to the adjacent twin planes. Let the total dislocation density to be ρ_{tot}, and a small fraction $P_{promoter}$ of dislocations penetrate the twin planes and can act as promoters. For a moving twin partial dislocation with velocity v_{glide} and length l_{tw}, the rate of encountering a promoter is expressed as:

$$R = P_{promoter}\rho_{tot}v_{glide}l_{tw} \tag{6.2}$$

The average time required to meet one promoter is inversely related to the rate as $\triangle t_{tw} = \frac{1}{R}$. Let d_{tw} denote the distance between twin planes, then the velocity of twin partial dislocation crossing twin planes is the distance over time interval, expressed as:

$$v_{grow} = \frac{d_{tw}}{\triangle t_{tw}} = d_{tw}P_{promoter}\rho_{tot}l_{tw}v_{glide} \tag{6.3}$$

In the scenario of stimulated slip model, the twin continuously glides on adjacent planes, and the time-average plastic shear rate due to micro-twinning can be obtained from the Orowan equation. It is expressed in terms of the gliding velocity v_{glide}, the density of twin partial dislocation ρ_{tw} and its Burgers vector as $\dot{\gamma}_{tw} = \rho_{tw}b_{tw}v_{glide}$. Substituting equation (6.1) into Owowan equation, the twin system shear rate in equation (6.9) is obtained:

$$\dot{\gamma}_{tw} = \dot{\gamma}_0 \exp\left(-\frac{\triangle F - \tau A_P b_{tw}}{K_B T}\right) \tag{6.4}$$

where $\dot{\gamma}_0 = \rho_{tw} b_{tw} f_{shuffle} \lambda_{shuffle}$.

Compare to dislocation slip, deformation twinning causes shear in an analogous but difference way which needs to be accounted in the model. In both slip and deformation twinning, the lattice is sheared. In slip, the lattice configuration is not altered, and many dislocations can glide on the same lattice plane. The shear associated with slip may be many times of Burgers vector b depends on the number of dislocations involved, as illustrated in figure 6.1a. On the other hand, the deformation twinning reorientates the lattice into a mirror symmetric configuration , and no subsequent twin can glide on a twinned lattice plane. The shear associated with deformation twinning is uniformly distributed over a volume, as illustrated in figure 6.1b. The maximum shear γ_{tw}^{max} that deformation twinning can contribute in a volume varies with twin types, e.g. for $\left\{10\bar{1}2\right\}$ twin in Mg, $\gamma_{tw}^{max} = 0.1289$.

In addition, the shear associated with slip can be positive or negative, depends on the direction of dislocation slip and the local stress. The deformation twinning can only provide shear in one direction which leads to mirror symmetric lattice configuration. Thus, shear associated with deformation twinning needs to satisfy the constraint $0 \leq \gamma_{tw} \leq \gamma_{tw}^{max}$.

The shear resistance of twinning partial dislocation changes when it interacts with dislocations, precipitates and other twin variants. This may be caused by the interaction of

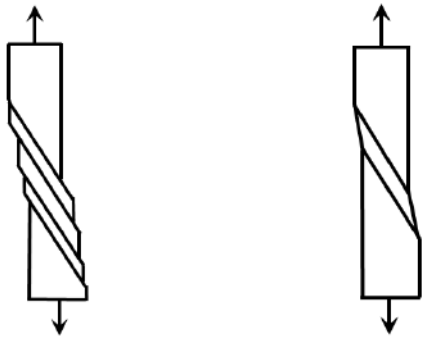

Figure 6.1: Figure illustrating the shear deformation contributed by (a) dislocation slip and (b) deformation twinning

mobile dislocations which can impact the twin boundary and create local surface steps [44], or by interaction with immobile forest dislocations, precipitates and existing twins which hinder the twin gliding or growth. Though equation (6.4) does not contain the shear resistance term explicitly and can not be directly adopted for modeling the hardening of twin systems, it can be modified into a conventional shear-resistance-based power-law model based on the arguments in [111]. This derivation is presented in the followings.

At $0K$ temperature, no thermal activation process is feasible. Any local obstacle with an internal energy barrier $\triangle F$ has be to overcame before further twin gliding by the applied stress $\tau(T = 0)$, i.e., $\triangle F = \tau(T = 0)V^*$, where $V^* = A_p * b_t w$ is the activation volume. Substitute this relation into equation (6.4), the twin shear rate at the temperature T can be rewrite as:

$$\dot{\gamma}_{tw} = \dot{\gamma}_0 \exp\left[-\frac{\triangle F}{K_B T}\left(1 - \frac{\tau(T)}{\tau(T=0)}\right)\right] \tag{6.5}$$

For moderate rates of plastic deformation, the factor $\frac{\tau(T)}{\tau(0)}$ is of the order O(1), and the exponential term $\exp\left(\frac{\tau(T)}{\tau(0)} - 1\right)$ can be expanded in a series and retain only the linear term $\frac{\tau(T)}{\tau(0)}$ by approximation. With this approximation and the relation $\exp(ab) = \exp(a)^b$, equation (6.5) can be rewritten in a power-law form as:

$$\dot{\gamma}_{tw} = \dot{\gamma}_0 \left|\frac{\tau(T)}{\tau(T=0)}\right|^{\frac{\triangle F}{K_B T}} sign\left(\tau(T)\right) \tag{6.6}$$

Finally, at 0K temperature the twin shear resistance s_{tw} equals to the required resolved shear stress $\tau(T = 0)$ in magnitude. Replace $\tau(T = 0)$ with s_{tw} in equation (6.6), the conventional power-law type plastic shear rate model is obtained for deformation twinning. The phenomenological hardening law is adopted in this work for the changes of s_{tw} due to interactions with dislocations and other twins, for simplicity. For a twin system α, the changes in shear resistance can be caused by the interaction with any dislocation system β or twin system ζ, expressed as:

$$\dot{s}^{\alpha}_{tw} = \sum_{\beta=1}^{N_{slip}} h^{\alpha\beta}\left|\dot{\gamma}^{\beta}\right| + \sum_{=1}^{N_{tw}} h^{\alpha\zeta}\left|\dot{\gamma}^{\zeta}_{tw}\right| \tag{6.7}$$

where the hardening matrix $h^{\alpha\beta}$ and $h^{\alpha\zeta}$ defines the hardening from dislocation systems and twin systems, respectively. In this work, the values in $h^{\alpha\beta}$ and $h^{\alpha\zeta}$ are all taken as 1 for simplicity.

6.2 Flow Rules of Deformation in Micro-Twins and Matrix

The evolution of plastic deformation in the untwinned matrix region is solely dominated by dislocation slip and is expressed in terms of the plastic velocity gradient $\mathbf{L}^p$ as:

$$\mathbf{L}^p = \dot{\mathbf{F}}^p \mathbf{F}^{p-1} = \sum_{\alpha=1}^{N_{slip}} \dot{\gamma}^\alpha \mathbf{s}_{0,slip}^\alpha \tag{6.8}$$

where $\dot{\gamma}^\alpha$ is the slip rate on a slip system α given by equation (2.12) and N_{slip} is the total number of slip systems. The Schmid tensor associated with α-th slip system $\mathbf{s}_{0,slip}^\alpha$ is expressed in terms of the slip direction $\mathbf{m}_{0,slip}^\alpha$ and slip plane normal $\mathbf{n}_{0,slip}^\alpha$ in the reference configuration, i.e. $\mathbf{s}_{0,slip}^\alpha = \mathbf{m}_{0,slip}^\alpha \otimes \mathbf{n}_{0,slip}^\alpha$. When a twin boundary propagates, it introduces shear on the twin plane. The plastic flow in the twinned region is caused by the twin shear and the dislocation slip. The plastic velocity gradient in twinned region is expressed as:

$$\mathbf{L}^p = \dot{\mathbf{F}}^p \mathbf{F}^{p-1} = \sum_{\beta=1}^{N_{twin}} \dot{\gamma}^\beta \mathbf{s}_{0,tw}^\beta + \sum_{\alpha=1}^{N_{slip}} \dot{\tilde{\gamma}}^\alpha \tilde{\mathbf{s}}_{0,slip}^\alpha \tag{6.9}$$

where $\dot{\gamma}^\beta$ is the shearing rate on a twin system β and N_{twin} is the total number of twin systems. The Schmid tensor $\mathbf{s}_{0,tw}^\beta$ of a twin system β is expressed in terms of the twin shearing direction vector $\mathbf{m}_{0,tw}^\beta$ and twin plane normal $\mathbf{n}_{0,tw}^\beta$ in the reference configuration, i.e. $\mathbf{s}_{0,slip}^\beta = \mathbf{m}_{0,tw}^\beta \otimes \mathbf{n}_{0,tw}^\beta$. When a twin propagate through a matrix region, the crystal lattice is reorientated into a symmetric configuration. The slip direction $\tilde{\mathbf{m}}_{0,slip}^\alpha$ and slip plane normal $\tilde{\mathbf{n}}_{0,slip}^\alpha$ in a twinned region is related to the original $\mathbf{n}_{0,slip}^\alpha$ and $\mathbf{m}_{0,slip}^\alpha$ in the matrix region by the following relations:

$$\tilde{\mathbf{m}}^{\alpha}_{0,slip} = \mathbf{C}^{\beta}\mathbf{m}^{\alpha}_{\mathbf{0,slip}} \qquad \widetilde{\mathbf{n}}^{\alpha}_{0,slip} = \mathbf{C}^{\beta^{-T}}\mathbf{n}^{\alpha}_{0,slip} \tag{6.10}$$

where $\mathbf{C}^{\beta}$ is the re-orientation matrix of the twin system β. The formulation of $\mathbf{C}^{\beta}$ is given in Niewczas [112]. In equation (6.9) the Schmid factor of the re-orientated slip system α in the twinned region is expressed as $\tilde{\mathbf{s}}^{\alpha}_{0,slip} = \tilde{\mathbf{m}}^{\alpha}_{0,slip} \otimes \tilde{\mathbf{n}}^{\alpha}_{0,slip}$, and $\dot{\tilde{\gamma}}^{\alpha}$ is the slip rate in the re-orientated system α.

6.3 Numerical Implementation of Twinning Propagation Model in CPFE Analysis

The micro-twin nucleation, propagation, and growth is explicitly implemented into CPFE analysis, rather than being represented using the pseudo-slip approach which tends to predict non-physical diffusive twined microstructures. The implementation scheme is shown in figure 6.2. At stage 1, the twin nucleation criteria in equation (5.15) are check for all elements at the end of each time increment. Once an element satisfies the nucleation criteria, this element is identified as the twin nucleation site. The stage 2 starts once a twin nucleates in any grain. In the subsequent time steps, any elements in the same grain of the twin nucleation will be checked for criteria of twin propagation and growth, which are developed in the followings.

For a twin partial dislocation to glide to a vicinity point X on the same plane of the twin nucleus, the propagation velocity must be higher than the critical value, expressed as:

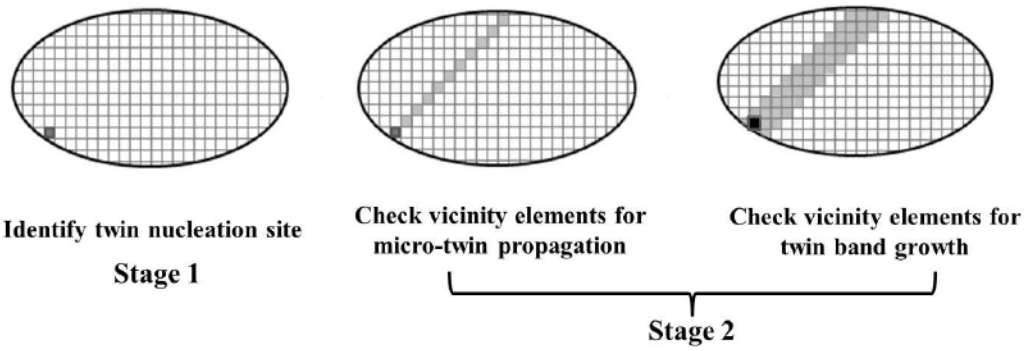

Figure 6.2: Illustration of implementing twin nucleation and propagation model into CPFE models .

$$v_{glide} \geq \frac{l_{glide}}{\Delta t_{twin}} \tag{6.11}$$

where l_{glide} is the distance between the vicinity point X and nucleation site, Δt_{twin} is the time interval from the time of twin nucleation $t_{nucleation}$ to current time t. Substituting equation (6.1) into equation (6.11), the criteria for micro-twin to propagate to a vicinity point X is established as:

$$\tau_{crit} \geq \frac{\ln\left(\frac{l_{growth}}{\Delta t_{twin} f_{shuffle} \lambda_{shear}}\right) K_B T + \Delta F}{A_p b_{tw}} \tag{6.12}$$

The growth of micro-twin is implemented by considering twin partial dislocation to move to a vicinity point that locates outside the twin plane of nucleation. A twin needs to move both normal to the twin plane with velocity v_{grow} and along the twin plane with velocity v_{glide} to propagate to the given point, as illustrated in figure 6.3. Let l_{growth} denote the distance from the given point normal to the twin plane, in addition to equation (6.11),

another requirement for twin velocity is:

$$v_{grow} \geq \frac{l_{growth}}{\Delta t_{twin}} \tag{6.13}$$

and the additional critical stress requirement for twin propagation is expressed as:

$$\tau_{crit} \geq \frac{\ln\left(\frac{l_{glide}}{\Delta t_{twin} f_{shuffle} \lambda_{shear} d_{tw} P_{promoter} \rho_{tot} l_{tw}}\right) K_B T + \Delta F}{A_p b_{tw}} \tag{6.14}$$

Equations 6.12 and 6.14 propagate a twin to neighboring material points in longitudinal direction and through-thickness direction, respectively. They construct the numerical criteria for twin propagation in finite element analysis. This is done explicitly at the end of each time increments. The temporal integration algorithm to update all deformation dependent variables, including twins, is presented in the next section.

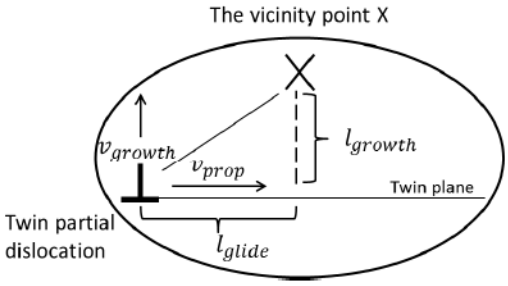

Figure 6.3: Illustration of twin partial dislocation propagation to a vicinity point X by growth normal to twin plane and glide on twin plane.

6.4 Temporal Integration Algorithm with Deformation Twinning

The crystal plasticity twin constitutive model requires non-local calculation of variables related to twin and GNDs from neighboring elements in a FE analysis. An algorithm is presented in this section to numerical integrate the coupled differential equation sets of the non-local constitutive model. The algorithm extends the time integration algorithm for CPFE model with only slips, as given in section 2.3. The extended numerical integration procedure can be divided into the following three steps: step (A), at each gauss point, with known values of deformation variables at time t, as well as a given deformation gradient $\mathbf{F}(t + \triangle t)$ at time $t + \triangle t$, updates stresses, plastic strains and all deformation state variables with the GND density and twin variables held fixed; step (B), after completing first step, update the GND densities and their rate of hardening by evaluating the curl of $\mathbf{F}^p$ with the adjacent elements; step (C), check all available gauss points for new twin nucleations, and propagate the existing twins. Note that step (A) is performed locally at each gauss point, whereas step (B) and the second part of step (C) both requires obtaining the variables from neighboring elements. The proposed algorithm adopts an implicit update algorithm proposed in [113] and extended in chapter 2 for step (A), and update step (B) and (C) explicitly. Step (C) updates twin domains by nucleating new twins and propagating existing twins. The most straightforward scheme to update twin may be by using an explicit staggered update algorithm. In such algorithm, the twin domains are updated at the end of

each time increment explicitly, and the simulation starts the next time increment with twin domain being holding fixed. However, the explicit stagger algorithm inevitably suffers from a critical time step constraint when the rate of twin nucleation and evolution is higher the rate of deformation. Exceeding this critical time step, the simulation will predict inaccurate twin configurations and deformation patterns. This is discussed in details in section 7.1.2 of chapter 7. An implicit subcycling algorithm to overcome the fine time constraint with excellent accuracy is proposed in section 7.2. The flow chart summarizing the sequence of computational procedures to integrate the non-local crystal plasticity twin constitutive models numerically is shown in table 6.1.

6.5 Conclusion

A non-local model for crystal plasticity finite element simulation of explicit micro-twin propagation is developed in this chapter. The velocity of micro-twin gliding is modeled using a thermal activation law which describes the atomic shear-shuffle motions on twin planes. The growth of twin band in thickness is interpolated by a stimulated slip model. The interactions among dislocation slips and twinning are taken into account implicitly by the evolution of twin system shear resistance. The twin propagation model is implemented into finite element framework by computing explicit twin band formation in elements using stress-based criterion. The time integration algorithm is summarized in the end of this

Table 6.1: Flowchart of computational operations in constitutive update procedure with deformation twinning.

Step **A**	Update local stress and deformation variables from t to $t+\triangle t$, with known $\mathbf{F}\,(t+\triangle t)$ and other variables at time t
i	Calculate trial second Piola-Kirchhoff stress $\mathbf{S}^{tr}$ from equation (2.34), and update slip rates $\triangle\gamma^{\alpha}$ using equations (2.12).
ii	Obtain the starting iterate $\mathbf{S}^{I}(t+\triangle t)$ from equation (2.32)
iii	For the i-th iteration step in the Newton-Raphson algorithm:
	(a) Compute residual $\mathbf{G}$ from equations (2.33)
	(a) Update $\mathbf{S}^{i+1}(t+\triangle t)$ from equations (2.35)
	(c) Check for convergence: if no, go back to step (a); if yes, proceed to step iv.
iv	Update slip system shear resistance with SSDs hardening using equations (2.26), (2.15)
v	Check for convergence of SSDs: if no, go back to step iii and compute stress with updated slip system shear resistance; if yes, proceed to step vi
vi	Evaluate $\mathbf{F}^{p}(t+\triangle t)$, Calculate $\mathbf{F}^{e}(t+\triangle t)=\mathbf{F}(t+\triangle t)\mathbf{F}^{p^{-1}}(t+\triangle t)$, Cauchy stress $\boldsymbol{\sigma}(t+\triangle t)=\frac{1}{det(\mathbf{F}^{e}(t+\triangle t))}\mathbf{F}^{eT}(t+\triangle t)\mathbf{S}(t+\triangle t)\mathbf{F}^{e}(t+\triangle t)$ and elasto-plastic stiffness matrix $\mathbf{C}=\frac{\partial\boldsymbol{\sigma}}{\partial\boldsymbol{\varepsilon}}$.
vii	Execute step **B**
Step **B**	Update non-local deformation variables related to GNDs
i	Compute nodal value of $\mathbf{F}^{p}(t+\triangle t)$ with SPR method and obtain $\boldsymbol{\nabla}_{X}\times\mathbf{F}^{p^{T}}$
ii	Compute Nye's tensor $\boldsymbol{\Lambda}$ and obtain GND density from equation (2.23)
iii	Update slip system shear resistance with GND hardening using equations (2.24) and (2.26).
iv	Execute step **C**
Step **C**	Update new twin nucleations and evolve existing twin bands
i	Identify new twin nulceation sites by checking all elements that have not nucleated or propagated a micro-twin with nucleation criteria equation (5.15).
ii	Evolve the existing twin bands by checking all elements at the vicinity of twin nucleation site with twin propogation criteria (6.12) and growth criteria (6.14).

chapter. However, the multi-time-scale method is required to improve the efficiency and accuracy of the twin propagation calculation, as discussed in chapter 7.

Chapter 7

Multi-Time-Domain Integration of CPFE Twin Nucleation Propagation Model

The proposed CPFE twin models may suffer low computation efficiency when simulating a high-resolution virtual microstructure. The issue comes from the mismatch of high evolution rate of twins and low deformation rate of the matrix. Mainly, the localized deformation rate inside twin bands causes numerical instability of the very stiff power-law type constitutive equations, which can only be solved by adopting a very fine simulation time step. The high-resolution mesh of the polycrystalline microstructure with very fine time steps causes the large deformation simulation of Mg alloys to be infeasible. Furthermore, the explicit staggered algorithm of updating twins predicts inaccurate twin configurations. These instabilities are explained in details in the first part of this chapter. A novel multi-time scale method is then developed to integrate the CPFE model with twinning and deformation localization. Three numerical tests with twin formations are conducted to examine the accuracy and efficiency of the proposed multi-time-domain method. With the enhancement of multi-time-domain method, the simulation of the micro-twin microstructures and twin-induced heterogeneous deformation are studied in details at the end of this chapter.

7.1 Instability of CPFE Simulation with Deformation Twinning

The power-law type crystal plasticity constitutive models are often reported to be exceedingly stiff [114–117]. The cause is the low strain-rate sensitivity of metals at room temperature, which leads to a very small value of the rate sensitivity parameter m in the slip rate equation, e.g. m is taken as 0.02 for magnesium alloys at room temperature in equation (2.12) for Mg alloys. The fact that the stress state is not very sensitive to applied strain-rates inversely leads to the consequence that small variation in resolved shear stress causes a large change in calculated slip rates. As observed from equation (2.12), unless the ratio of $\tau^{\alpha}_{eff}/s^{\alpha}_{*}$ is less than or very close to unity, the dislocation slip rate $\dot{\gamma}$ readily attain very high values even if the effective resolved shear stress τ^{α}_{eff} is only slightly greater than the slip resistance s^{α}_{*}. The slope of this highly non-linear equation is also rapidly increasing for regime $\tau^{\alpha}_{eff} > s^{\alpha}_{*}$. This difficulty leads to instabilities of the overall system. Even the Newton-Raphson method can not overcome the convergence issue. In practice, instability is detected when

$$\dot{\gamma}^{\alpha}\Delta t \geq \Delta\gamma_{crit} \tag{7.1}$$

where $\Delta\gamma_{crit}$ is a critical slip increment for slip system α. An alternative criteria is proposed based on the ratio of $\tau^{\alpha}_{eff}/s^{\alpha}_{a}$ in [113], expressed as:

$$\tau^{\alpha}_{eff}/s^{\alpha}_{a} \leq r_{crit} \tag{7.2}$$

where the critical ratio r_{crit} is taken the value of 2.0 [113]. The above stability criteria establish a critical time step Δt_{crit} for the temporal integration algorithm of crystal plasticity model in section 6.4. Notice that the slip rate $\Delta\gamma_{crit}$ and effectively resolved shear stress τ^{α}_{eff} are implicitly dependent on time step Δt in a backward Euler update algorithm, thus Δt_{crit} can be expressed as:

$$\Delta t_{crit} = \Delta t(m, \gamma_0, \mathbf{C}^e, s^{\alpha}_a, s^{\alpha}_*, \tau^{\alpha}, \Delta\gamma_{crit}, r_{crit}) \tag{7.3}$$

which depends on material properties m, γ^0, $\mathbf{C^e}$, the evolving internal state variable s^{α}_a, s^{α}_*, τ^{α}, and the criteria value $\Delta\gamma_{crit}$ or r_{crit}. Thus, the critical time step evolves with the evolution of internal state variables. Several numerical methods have been proposed to alleviate this critical time step constraint, e.g., by delicately choosing an appropriate initial value to start the Newton-Raphson iteration for equation (2.32) [117], or adding a linear search technique to Newton-Raphson method [115]. These methods relieve the critical time step and accelerate crystal plasticity finite element analysis; however, none of them can remove the critical time step constraint.

When simulating the large deformation of polycrystalline microstructure with deformation twinning, a power-law model for shearing on twin systems is introduced in equation (6.6). This model imposes an even stricter instability issue than dislocation slips as that twinning is reported to be even less rate sensitive than dislocation slips at room temperature [118]. Furthermore, the lattice misorientation across grain boundaries and twin boundaries

render the deformation to be heterogeneous. The stress concentrates inside twin bands, at grain boundary-twin, and twin boundary -twin boundary intersections. As a consequence, the distribution of critical time steps inside the twinned microstructure is not uniform. Besides, the heterogeneity is adamant in Mg alloys because that the shear resistances of $\{10\bar{1}2\}$ tensile twin systems are much less than the competing $\langle c+a \rangle$ slip systems, which causes the deformation rates across twin boundaries varies significantly. As the strain localizes inside twin bands, a crack can initiate and propagate along twin boundaries [14]. This is known as the major cause of twin-induced failure in Mg alloys. Figure 7.1a shows the strain rate distributions at 2% strain in an AZ31 alloy polycrystalline microstructure containing 152 grains. As can be seen, the strain rate inside twin bands is, in general, $5-10$ times higher than matrix region. This leads to an apparent difference in determining the critical time step distribution, as shown in figure 7.1b. The elements of twin bands, especially those close to twin boundaries and grain boundaries, requires much smaller critical time steps to proceed the simulation than the bulk of the model. A quantitative comparison of the critical time step size is presented in table 7.1. As illustrated in table 7.1, 99% elements can proceed with a time step $t = 5s$, but the entire CPFE simulation has to proceed with a 2 order smaller time step $t = 0.0391s$ due to 3 elements in the region of extreme deformation localization. The CPFE simulation is wasting computing efforts by forcing all elements to adopt the lowest critical time step associated with very a few the extreme deformation localization region. In a high-resolution microstructure, e.g., the number of elements is over one million, the simulation can be enormously slow

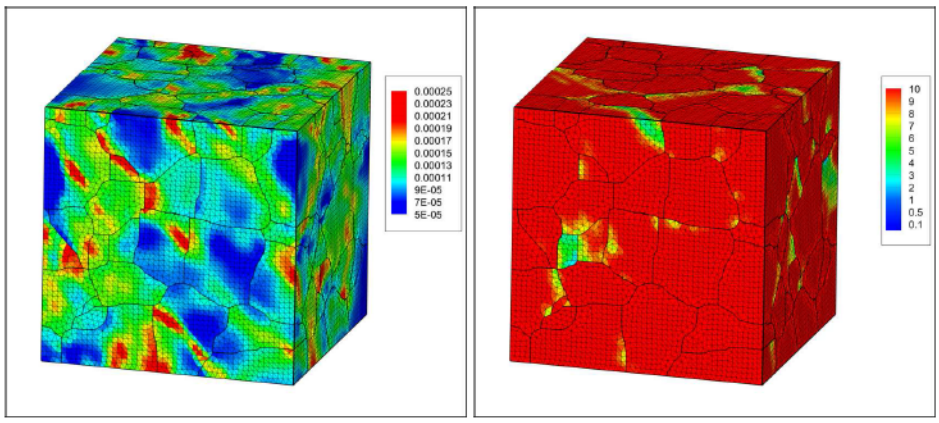

(a) (b)

Figure 7.1: (a)Strain rate distribution at 2% strain in a crystal plasticity finite element simulation of AZ31 polycrystal microstructure. (b) distribution of critical time step.

Δt_{crit} (seconds)	10	5	2.5	1.25	0.625	0.313	0.156	0.0781	0.0391
# of elements	672868	15693	7593	2171	535	183	61	23	3

Table 7.1: Distribution of critical time step size to the number of elements.

7.1.1 Evaluation of critical time step distribution

It is worth mentioning that the explicit expression of critical time step in equation (7.3) may be too difficult to obtain as it depends on the iterative value of second Piola-Kirchhoff stress and shear resistances in a Newton-Raphson algorithm as well as other numerical treatments, e.g., linear search technique. An empirical method is presented next to avoid the complexity. It evaluates the distribution of critical time step in FE simulation regardless of the algorithm used in the constitutive update.

Suppose the RVE is at equilibrium and every variable is known at time t. The applied boundary condition after an time increment Δt is represented by the applied external load

vector $\mathbf{f}^{ext}_{t+\Delta t}$. The CPFE simulation starts the increment $t \rightarrow t + \Delta t$ by obtaining a trial displacement increment vector:

$$\Delta \mathbf{u}^{trial}_{t \rightarrow t+\Delta t} = \mathbf{K}_t^{-1} \left(\mathbf{f}^{ext}_{t+\Delta t} - \mathbf{f}^{int}_{t} \right) = \mathbf{K}_t^{-1} \Delta \mathbf{f}^{ext}_{t \rightarrow t+\Delta t} \tag{7.4}$$

where $\mathbf{f}^{int}_t$ is the internal force vector and at equilibrium state $\mathbf{f}^{int} = \mathbf{f}^{ext}$. $\mathbf{K}$ is the tangent stiffness matrix for the system. Next, the internal stress and deformation-dependent variables are updated with the trial displacement increment vector $\mathbf{u}^{trial}_{t+\Delta t}$ at all element Gauss points. If an element fails to update the constitutive model variables due to numerical instability, the CPFE simulation has to reduce time step and the critical time step Δt_{crit} for this element is smaller than the attempted time increment Δt. Based on this simple idea, the minimum required time increment for all elements can be approximated by attempting different time increment Δt.

The above approach may be clumsy for practice. Further improvements are presented here to reduce the computing efforts dramatically. Firstly in many tests the boundary conditions $\Delta \mathbf{f}^{ext}$ can be expressed as a function with single dependent variable Δt, e.g. in a simple constant strain rate loading simulation $\mathbf{f}^{ext}_{t \rightarrow t+\Delta t} = \dot{\mathbf{f}}^{ext} \Delta t$ where $\dot{\mathbf{f}}^{ext}$ is a vector contains constant values. In such cases, if the desired time increment is is reduced to $\Delta t/a$, with $a > 1$ being a arbitrary positive number , one can directly interpolate the new trial displacement increment $\Delta \mathbf{u}^{trial}_{t->t+\Delta t/a}$ from $\Delta \mathbf{u}^{trial}_{t->t+\Delta t}$, which is expressed as:

$$\Delta \mathbf{u}^{trial}_{t \to t+\frac{\Delta t}{a}} = \frac{\left\| \Delta \mathbf{f}^{ext}_{t \to t+\Delta t/a} \right\|}{\left\| \Delta \mathbf{f}^{ext}_{t \to t+\Delta t} \right\|} \Delta \mathbf{u}^{trial}_{t \to t+\Delta t} \tag{7.5}$$

This is illustrated in a simple one degree of freedom system in figure 7.2. The time-consuming re-solving of linear system of equation (7.4) for attempted reduced time increments can be therefore avoid.

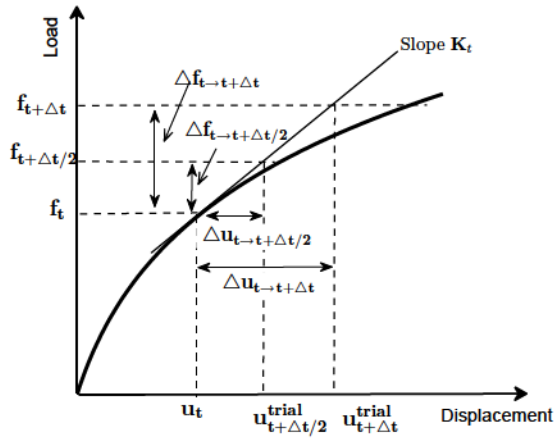

Figure 7.2: Illustration of obtaining trial displacement in a simple one degree of free system.

Secondly, the elements which successes in updating state variables with a significant time increment Δt need not be to re-calculated for the reduced time increments $\Delta t/a$. With above preliminaries, the algorithm to numerically evaluate the critical time step for entire RVE is presented in the table 7.2. This algorithm runs once at the beginning of each time step in a CPFE simulation.

Table 7.2: Flowchart of computational operations in evaluating critical time step

Step 1	For element i = 1, total number of elements
i	Obtain trial displacement increment $\Delta\mathbf{u}^{trial}_{t\to t+\Delta t}$ from equation (7.4)
ii	Compute trial deformation gradient $\mathbf{F}^{trial}_{t+\Delta t} = \mathbf{I} + \partial(\mathbf{u}_t + \Delta\mathbf{u}^{trial}_{t\to t+\Delta t})/\partial\mathbf{X}$
iii	Perform crystal plasticity constitutive update with $\mathbf{F}^{trial}_{t+\Delta t}$
iv	If step 1-iii converge, the critical time step of element i is determined as Δt
	If step 1-iii fail to converge, element i belongs to element set $\{N1\}$
v	Reduce time step increment to $\frac{\Delta t}{a}$;
Step 2	For element i = 1, all element in $\{N1\}$
i	Obtain trial displacement increment $\Delta\mathbf{u}^{trial}_{t\to t+\Delta t/a}$
ii	Compute trial deformation gradient $\mathbf{F}^{trial}_{t+\Delta t/a} = \mathbf{I}+\partial(\mathbf{u}_t+\Delta\mathbf{u}^{trial}_{t\to t+\Delta t/a})/\partial\mathbf{X}$
iii	Perform crystal plasticity constitutive update with $\mathbf{F}^{trial}_{t+\Delta t/a}$
iv	If step 2-iii converge, the critical time step of element i is determined as $\Delta t/a$
	If step 2-iii fail to converge, element i belongs to element set $\{N2\}$
v	Reduce time step increment to $\frac{\Delta t}{a^2}$;
Step 3	For element i = 1, all element in $\{N2\}$
	.
	.
	.
Step N	Repeat until the critical time step for all elements have been estimated.

7.1.2 Critical time step due to updating deformation twinning

The explicit staggered algorithm of updating deformation twinning introduces another time step constraint when the rate of twin nucleation and propagation is higher than the rate of deformation. Figure 7.3 demonstrates this issue. The proposed CPFE model is adopted to simulate the deformation process of a single crystal from time $t1$ to time $t2$, and a micro-twin nucleate at an intermediate time $t3$, as illustrated in figure 7.3a. The deformation can be considered as two stages: before twin nucleation the deformation is homogeneous and after twin nucleation the deformation is heterogeneous due to the different strain rates in twin bands and matrix. If the simulation time step is sufficiently small, e.g. a time increment $\triangle\tau$ smaller than the characteristic time scale for twin nucleation and evolution is adopted, the result of CPFE simulation using explicit staggered algorithm converges to the twin-induced heterogeneous deformation accurately, as demonstrated in figure 7.3b. However, if the time step increment is large, e.g., $\triangle t = \frac{t2-t1}{2}$ as shown in figure 7.3c, the simulation fails to capture the nucleation of the twin at $t3$. The simulated twin nucleation time is $t4 = t1 + \triangle t$ and propagation of the twin nucleus into a twin band is computed at time $t2$. Therefore, the twined material microstructure is not correctly captured, and simulations fail to predict the heterogeneous deformation. This error accumulates in a history-dependent CPFE model and leads to the divergence of the simulation results.

A pure Mg single crystal test illustrated this problem, as shown in figure 7.4a. The single crystal has a dimension of $20mm \times 10mm \times 20mm$, which is discretized into 67418 four node

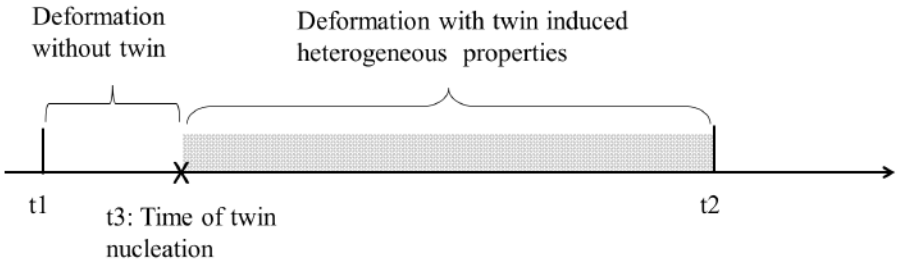

(a)

Explicit staggered algorithm of twin: with a fine time step $\Delta\tau$

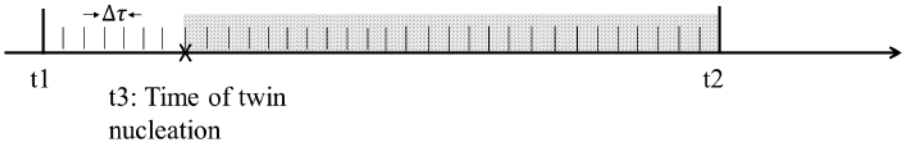

(b)

Explicit staggered algorithm of twin: with a coarse time step Δt

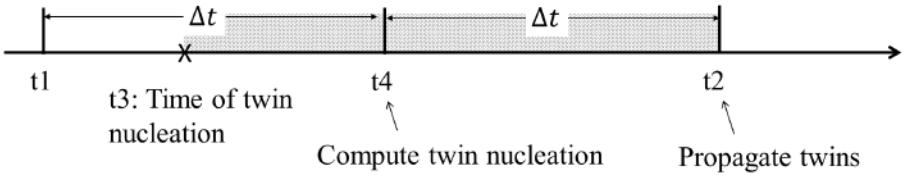

(c)

Figure 7.3: (a)Illustration of cause of critical time step associated with explicit staggered twin update algorithm

tetrahedrons and 13021 nodes. A uniaxial loading with applied constant strain rate 1×10^{-4} is applied on the top surface along the x-axis, and minimum displacement boundary condition is applied to the bottom surface. The single crystal has a crystal orientation specified by Euler angle $[0^o, 7^o, 0^o]$ in ZXZ convention. The loading direction leads to the formation of $\left\{10\bar{1}2\right\}$ tension twins. The 5 degree slight tilting of the crystal orientation is to make the Schmid factor of twin variant 1 to be highest among all 6 twin variants. Thus, only twin variant 1 will be formed during the test. Without this tilting, both the twin variant 1 and 4 have the highest Schmid factor and the interaction between them must be considered. To allow the heterogeneous formation of twin bands, a perturbation is applied to the initial twin system energy in all elements which is obtained from uniform distribution function. Six groups of simulation using a time step of $1s$,$2s$,$4s$,$6s$,$8s$ respectively and $10s$ are conducted. Figure 7.4 shows the simulation results of the fraction of twinned elements at 1% strain as a function of simulation time step sizes. It clearly illustrates that with large time steps $\triangle t > 2s$ the simulation results diverges. This example demonstrated that simple explicit staggered twin model implementation fails to predict the highly heterogeneous and history dependent material response.

7.2 Adaptive Subcycling Algorithm for Accelerating CPFE simulation

Section 7.1 posts a major difficulty for CPFE twin analysis in the polycrystalline microstructure, which is that a large portion of computing efforts is wasted by enforcing the simulation

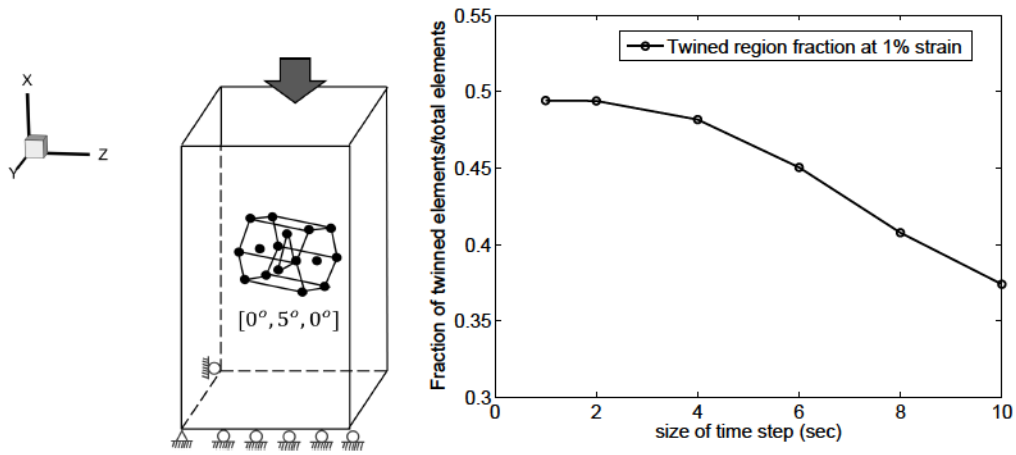

Figure 7.4: (a) Simulation setup of Mg single crystal under constant strain rate uniaxial loading (b)Fraction of twinned elements with different simulation time step

to adopt the finest critical time step determined by the extreme deformation localization region and matching the rate of twinning. To work around the minimum critical time step constraints, a novel subcycling algorithm is proposed in the section. This section is divided into two parts: firstly the basic subcycling framework is proposed for any power-law type crystal plasticity constitutive models without considering twins; secondly, a particular subsection is devoted to implementation of the subcycling algorithm into modeling deformation twins. The goal is to demonstrate that the proposed subcycling algorithm is capable of accelerating any power-law type CPFE models, and it is essential for efficient and accurate modeling of deformation twinning.

The proposed subcycling algorithm allows each region of the model to adopt a different time step to perform the crystal plasticity constitutive update. The bulk region of the model adopts a coarse time step and the major computational resources can be spent on

computing the extreme deformation localization region using fine time steps. Figure 7.5 illustrates the concept of subcycling algorithm. The spatial domain of simulation is divided into two regions, namely the deformation localization region with fine critical time step and the rest bulk region with coarse time step. It is emphasized that proposed subcycling algorithm is straightforward to extend into multiple domain partitions. Instead of solving the entire system with one uniform time step, the local equilibrium in deformation localization region is solved along using a very fine time step $\triangle\tau$ from time t to $t + \triangle t$, with the boundary conditions being interpolated from a displacement predictor. In the rest low deformation rate region, a coarse time step $\triangle t$ is adopted to perform the constitutive update. At time $t + \triangle t$, the displacement corrector of the system is obtained by equilibrating the two regions. The proposed subcycling algorithm has the following properties compared to explicit subcycling algorithm in dynamic FE simulation [115] . 1, the subcycling algorithm preserve a fully implicit temporal integration scheme for crystal plasticity constitutive laws. 2, the subcycling algorithm ensures global stress equilibrium and the accuracy of FE solution is not affected. 3, the subcycling algorithm is independent of the constitutive model and can be applied universally.

7.2.1 Formulation of subcycling algorithm

The CPFE analysis solves for the equilibrium state of material undergoes large deformation from time t to $t + \triangle t$. The system of non-linear equations in CPFE analysis is derived in section 3.1 as:

$$\mathbf{K}_t \triangle \mathbf{u}_{t \to t+\triangle t} = \mathbf{f}^{ext}_{t+\triangle t} - \mathbf{f}^{int}_t \tag{7.6}$$

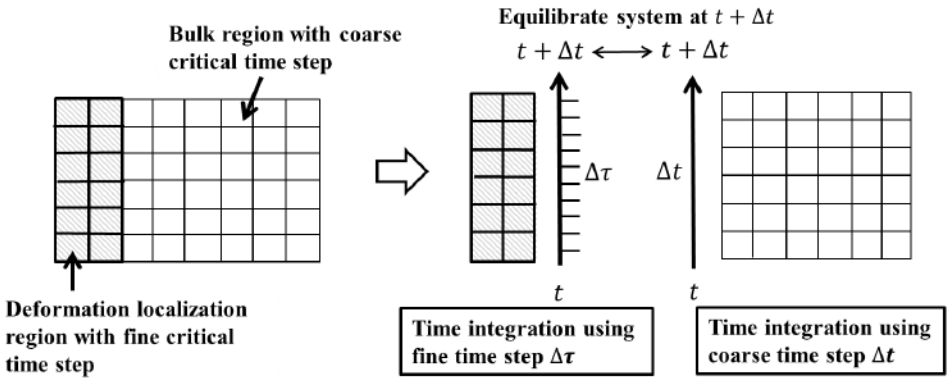

Figure 7.5: Illustration of subcycling algorithm

where $\mathbf{K}_t$ is the tangent global stiffness matrix at time t. $\mathbf{f}_{t+\Delta t}^{ext}$ and $\mathbf{f}_t^{int}$ are respectively the prescribed applied external force vectors at time $t + \Delta t$ and internal force vector at time t, expressed as:

$$\mathbf{f}_t^{int} = \int_{\Omega_t} \mathbf{B}_t^T \boldsymbol{\sigma}_t d\Omega_t \tag{7.7a}$$

$$\mathbf{f}_{t+\Delta t}^{ext} = \int_{\Omega_{t+\Delta t}} \mathbf{N}_{t+\Delta t}^T \mathbf{b}_{t+\Delta t}\, d\Omega_{t+\Delta t} + \int_{\Gamma_{t+\Delta t}^{\bar{\mathbf{t}}}} \mathbf{N}_{t+\Delta t}^T \bar{\mathbf{t}}_{t+\Delta t}\, d\Gamma_{t+\Delta t}^{\bar{\mathbf{t}}} \tag{7.7b}$$

where σ is Cauchy stress, $\mathbf{b}$ is the body force, $\bar{\mathbf{t}}$ is the applied traction. $\mathbf{B}$ is the strain-displacement matrix, bfN is the shape function matrix. For a four node tetrahedron element, $\mathbf{B}$ and $\mathbf{N}$ has a dimension 6×12 and 3×12 respectively. Ω denotes the volume of the deforming body, $\Gamma^{\bar{\mathbf{t}}}$ is the surface where traction is applied.

The spatial domain of virtual microstructure represented by finite elements is divided into sub-domains in the subcycling algorithm. Each domain has a characteristic time step.

For simplicity only two domains are considered in this work, namely a fine domain for the elements with a very fine critical time step $\triangle t$, and the rest elements assemble a coarse domain. This two-domain-division is appropriate for the example illustrated in figure 7.1a and quantified in table 7.1. The tangent stiffness matrix $\mathbf{K}$ and internal force vectors $\mathbf{f}$ can thus be written as:

$$\mathbf{K} = \mathbf{K}^C + \mathbf{K}^F \tag{7.8a}$$

$$\mathbf{f}^{int} = \mathbf{f}^{int,C} + \mathbf{f}^{int,F} \tag{7.8b}$$

where $\mathbf{K}^C$ is the tangent stiffness matrix assembled from the coarse domain elements only, and similarly $\mathbf{K}^F$ is the tangent stiffness matrix assembled from fine domain elements only. $\mathbf{f}^{int,C}$ is the internal force vector assembled from coarse domain elements only and $\mathbf{f}^{int,F}$ is the force vector assembled from fine domain elements only. The subcycling algorithm avoids using the small time step to update the internal variables of coarse group elements. This is done by solving a series of local equilibrium problem within the fine domain along, followed by seeking the global equilibrium of the entire system in an iterative scheme. The following steps describes the details of the algorithm:

1. Compute trial displacement increment $\triangle \mathbf{u}^{trial}_{t \to t+\Delta t}$ from equation (7.4).
2. Using the trial displacement increment $\triangle \mathbf{u}^{trial}_{t \to t+\Delta t}$ and the scheme in section 6.4,

integrate the crystal plasticity constitutive models only for the elements in coarse group from time t to $t + \Delta t$. Obtain $\mathbf{K}^C_{t+\Delta t}$ and $\mathbf{f}^C_{t+\Delta t}$.

3. Use the trial displacement increment at the interface as the displacement boundary condition, solve the local equilibrium problem of the fine domain from time t to $t + \Delta t$ with small time increments $\Delta\tau$. The simulation in fine domain can be done using explicitly FE method with a fixed very small $\Delta\tau$, or implicit FE method with an adaptive $\Delta\tau$, depends on the particular problem. The displacement boundary condition at the interface for a sub-step $\tau \rightarrow \tau + \Delta\tau$ is obtained using a linear interpolated from $\Delta\mathbf{u}^{trial}_{t\rightarrow t+\Delta t}$, as followings:

$$\mathbf{u}^I_{\tau+\Delta\tau} = \mathbf{u}^I_\tau + \frac{\Delta\tau}{\Delta t}\Delta\mathbf{u}^{I,trial}_{t\rightarrow t+\Delta t} \tag{7.9}$$

where $\mathbf{u}^I_{\tau+\Delta\tau}$ and $\mathbf{u}^I_\tau$ are the displacement at coarse domain-fine domain interface at time $\tau + \Delta\tau$ and τ, respectively. $\frac{\Delta\tau}{\Delta t}\Delta\mathbf{u}^{I,trial}_{t\rightarrow t+\Delta t}$ is the components of $\frac{\Delta\tau}{\Delta t}\Delta\mathbf{u}^{trial}_{t\rightarrow t+\Delta t}$ at the interface between coarse domain and fine domain. Upon the completion of step 3, the following variables are obtained:

The tangent stiffness matrix of fine group elements at time $t + \Delta t$: $\widetilde{\mathbf{K}}^F_{t+\Delta t}$

The internal force vector of fine group elements at time $t + \Delta t$: $\widetilde{\mathbf{f}}^{int,F}_{t+\Delta t}$

The displacement increments for nodes in the interior of the fine domain, obtained by solving a sequence of fine time step FE problem: $\Delta\widetilde{\mathbf{u}}^F$

The symbol $\widetilde{}$ indicates that they are obtained by solving the local equilibrium problem

in fine domain with very fine time steps.

4. Check if the global equilibrium $\left\|\mathbf{f}_{t+\Delta t}^{ext} - \widetilde{\mathbf{f}}_{t+\Delta t}^{int,F} - \mathbf{f}_{t+\Delta t}^{int,C}\right\| \leq R_{crit}$ is satisfied, where R_{crit} is a scalar convergence criterion.

   - if yes, exit iteration. $\left\{\Delta\widetilde{\mathbf{u}}_{t\to t+\Delta t}^{F}, \Delta\mathbf{u}_{t\to t+\Delta t}^{I,trial}, \Delta\mathbf{u}_{t\to t+\Delta t}^{C,trial}\right\}^{T}$ is the solution to equation (7.6).

   - if no, calculate the corrector to the trial displacement as:

$$\Delta\mathbf{u} = \left(\widetilde{\mathbf{K}}_{t+\Delta t}^{F} + \mathbf{K}_{t+\Delta t}^{C}\right)^{-1}\left\{\mathbf{f}_{t+\Delta t}^{ext} - \widetilde{\mathbf{f}}_{t+\Delta t}^{int,F} - \mathbf{f}_{t+\Delta t}^{int,C}\right\} \tag{7.10a}$$

$$\Delta\mathbf{u}_{t\to t+\Delta t}^{corrector} = \Delta\mathbf{u}_{t\to t+\Delta t}^{trial} + \Delta\tilde{\mathbf{u}}^{F} + \Delta\mathbf{u} \tag{7.10b}$$

   Replace trial displacement increment vector with $\mathbf{u}_{t\to t+\Delta t}^{corrector}$, repeat step 2-4.

7.2.2 Implementation of deformation twinning models into the proposed subcycling algorithm

The subcycling algorithm provides a unique partition technique in both spatial domain and time domain. It deems to be an efficient way to model the twin nucleation and evolution. The twin bands undergo a fast shear which makes it inherently to be selected as the subcycling fine time scale domain. Based on this idea, a novel implicit subcycling algorithm to accurately capture the fine time scale twin nucleation and evolution is presented, as in the followings.

Figure 7.6 demonstrates the simulation process of deformation twinning with subcycling algorithm. For a large time increment $\triangle t = t2 - t1$ with potential twin nucleation at $t3$, the simulation first computes deformation without considering twins. At the end of this increment, twin nucleation is checked for all elements. If twin nucleations are detected at $t2$, as shown in figure 7.7a, simulation assigns elements that lie within the potential twin bands to the fine time-scale domain (figure 7.7b) and restore all deformation variables to the state in $t1$. The simulation of time increment from $t1$ to $t2$ is now being restarted with subcycling spatial and temporal domain partitions which allow the twin to nucleate and evolve within fine simulation steps. The time increment for subcycling fine time-scale domain is $\triangle\tau$ which is smaller than the characteristic time scale of twin nucleation and evolution. This ensures the accurate prediction of twin-induced deformation.

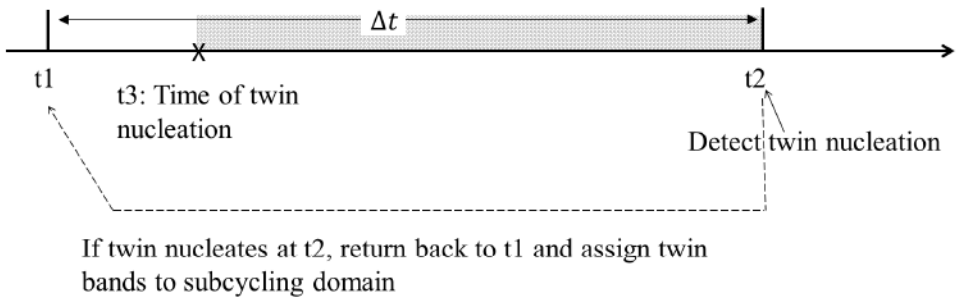

Figure 7.6: Illustration of applying subcycling algorithm in twin model

The following steps describe the details of the algorithm for a general simulation with deformation twinning:

1. With a fixed twin configuration, use a coarse time step $\triangle t$ to solve CPFE problem,

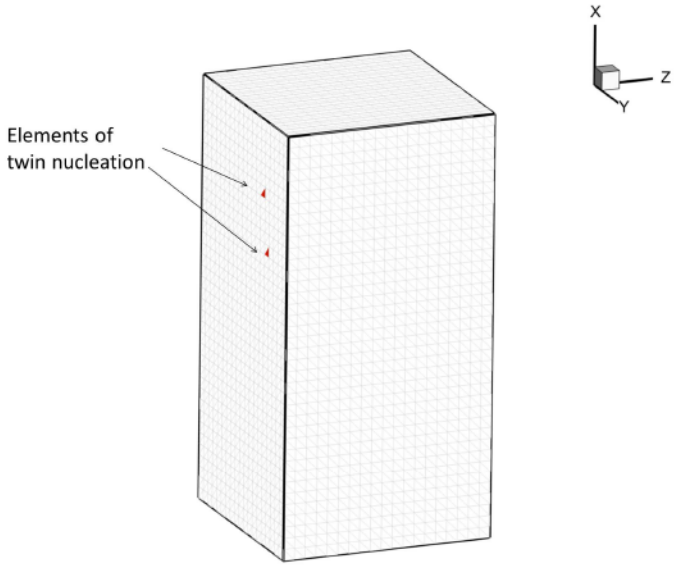

(a)

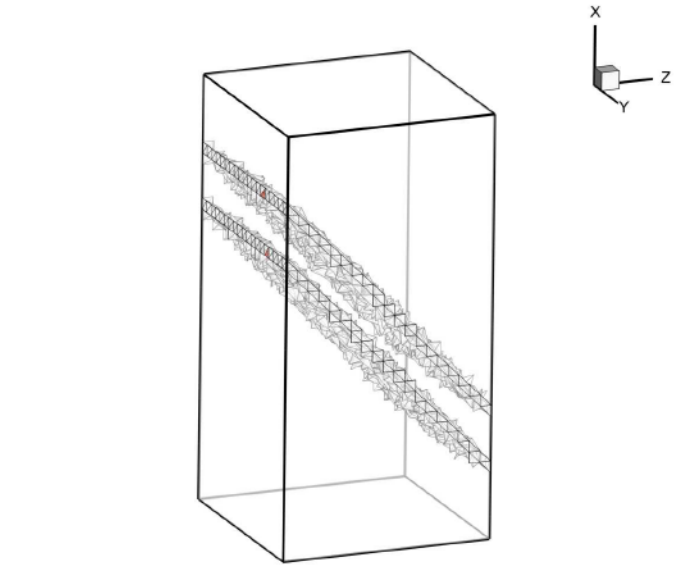

(b)

Figure 7.7: Illustration of applying subcycling algorithm in twin model (a) detecting twin nucleation (b) assigning elements in potential twin bands to subcycling fine time scale domain.

update stress and deformation dependent variables. Use subcycling algorithm without considering new twin nucleations for the deformation localization region. Obtain the displacement increment vector $\triangle \mathbf{u}^{trial}$ and the stress $\boldsymbol{\sigma}^{trial}$

2. Check for twin nucleation at all un-twinned integration points.
3. If new twin nucleation is detected, estimate the region of the new twin bands using the trial stress $\boldsymbol{\sigma}^{trial}$ obtained from step 1.
4. Construct the fine scale domain by adding the elements in the potential twin bands.
5. Revert stress and other deformation dependent variables to the store value at $t1$, and perform CPFE simulation from $t1$ to $t2$ with subcycling algorithm described in section 7.2.1. Nucleate and evolve twins in fine time scale domain after each fine time increment $\triangle \tau$.

7.3 Validation of the Subcycling Algorithm and the CPFE Twin Model

In this section, the accuracy, efficiency and robustness of the subcycling algorithm are verified by several numerical tests. A polycrystal SERVE microstructure is simulated with Mg CPFE model without taking into account of twinning, with the goal of checking the efficiency and reliability of the subcycling model for general CPFE problems. Next, the subcycling algorithm is validated by simulation with micro-twin formations by applying to a single crystal and poly crystalline SERVE microstructure in section 7.4 and 7.5.

7.3.1 Reliability of the subcycling algorithm

A primary requirement for subcycling algorithm is that it predicts converged results to conventional CPFE simulations. To verify the reliability of the algorithm, a polycrystal microstructure RVE under uniaxial loading is simulated with and without the subcycling algorithm for comparison. The virtual microstructure is constructed using the DREAM.3D software [94] following methods described in [101, 102]. The dimension of the RVE is $25\mu m \times 25\mu m \times 25\mu m$, which is discretized into 16371 tetrahedrons consisting of 3270 nodes. It contains 24 grains with an average grain size of $10\mu m$. Constant strain rate loading of $0.0001/s$ is imposed on the top surface, and minimum displacement boundary conditions are imposed on other surfaces to remove the rigid body modes, as illustrated in figure 7.8b. The model parameters for dislocation slip in magnesium alloy AZ31 is calibrated in chapter 4 and applied in this test. The simple test in this sub-section aims to show the proposed algorithm can be used universally to CPFE models without compromising the accuracy. For this propose, the features of deformation twinning is not turned on, and the case of twinning is discussed in detail in section 7.4.

The simulation results of macroscopic stress-strain responses with and without subcycling acceleration are plotted in figure 7.8b. Both simulations output simulation results every 10 time increments. No obvious mismatch is found in macroscopic mechanical responses between the two results. However, the results clearly show that less number of

time steps are required for the simulation with subcycling algorithm, which leads to an acceleration of computation. To further examine the difference at local material points, the distribution of stress in the microstructure is plotted in figure 7.9a for CPFE simulation with subcycling algorithm, compared to the results of conventional CPFE simulation plotted in 7.9b. The quantitative examination is performed by plotting the local stress component σ_{xx} at 3% strain along a line passing through the interior of the microstructure. The Very slight difference are observed for local stress from figure7.10 and the two results with and without subcycling algorithm seems almost identical. This is due to the subcycling algorithm seeks for the equilibrium of the system, and converges according to the same criteria of conventional CPFE model in an implicit iterative way. It does not apply any change to the constitutive model and convergence criteria. The reliability of the algorithm is confirmed.

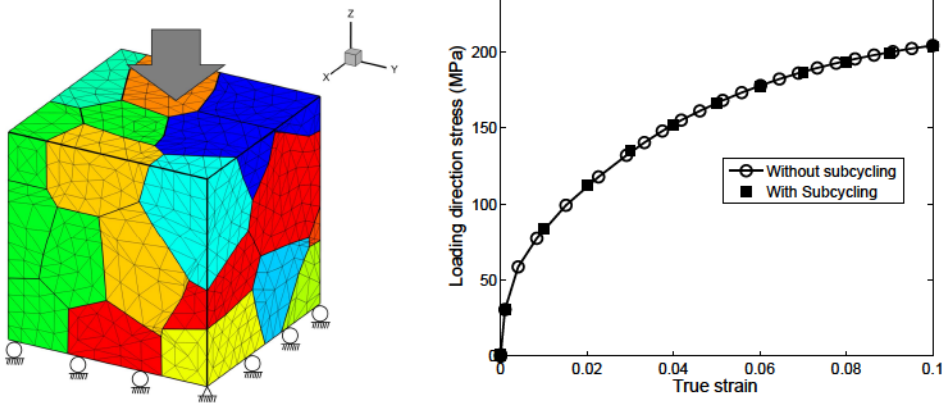

(a) (b)

Figure 7.8: (a) Figure showing loading and boundary condition of the polycrystal compression test (b)Macroscopic stress-strain response of microstructure containing 24 grains under constant strain rate loading

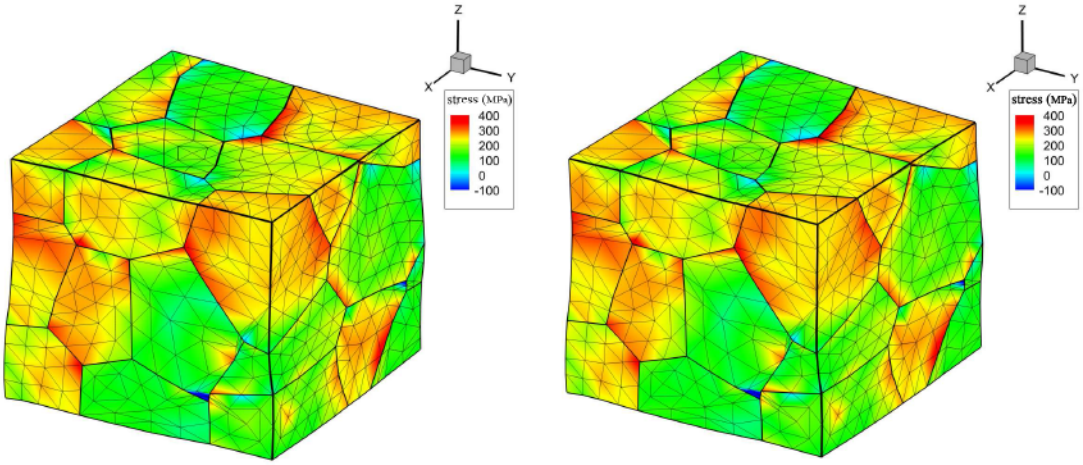

(a) (b)

Figure 7.9: (a)Loading direction stress σ_{xx} distribution in the polycrystalline microstructure of a 24 grain test problem. The simulation is done with subcycling accelaration algorithm, compared to (b) results of conventional CPFE analysis without subcycling.

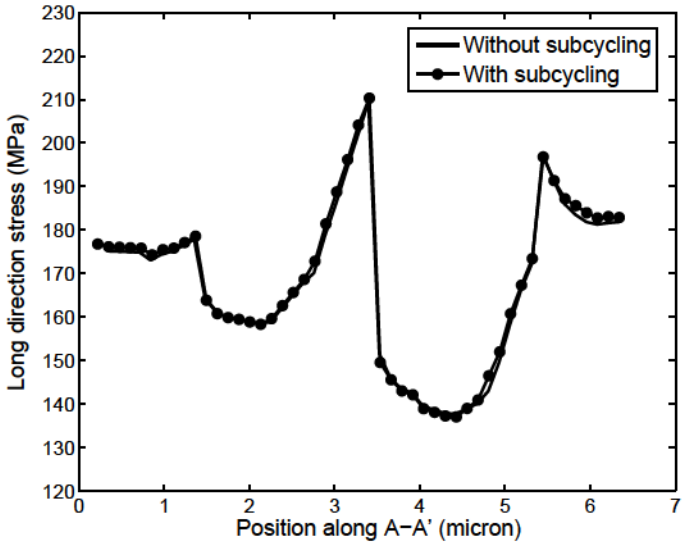

Figure 7.10: Comparing local stress σ_{zz} along a line in a middle section of the microstructure. The simulation using subcycling algorithm and without using algorithm predicts almost identical results.

7.3.2 Computational efficiency of the subcycling algorithm

First the computational efficiency of the subcycling algorithm in the previous tests in section 7.3.1 is analyzed. To establish a fair estimation of the computational cost, the tests are re-done on a single processor without outputting the results. To simulate to deformation of 10% strain, the test without subcycling acceleration takes 285 time steps and a total CPU time of 2125 seconds, whereas the test with subcycling acceleration takes only 109 steps and a total CPU time of 10182 seconds. Nearly 2 times acceleration is observed by applying subcycling algorithm. To further understand the acceleration effect, the distribution of time step lengths are shown in the histogram in figure 7.11. Both tests have a small fraction of less than 1 second time steps which are used to start the simulations in the very beginning. The test without subcycling has most time steps at a range of $2-4$ seconds, which is constraint by the critical time step of the elements in extreme deformation region, i.e. in this case is close to grain boundary junctions. Figure 7.12 plotted the number of Newton-Raphson iterations required for solving the non-linear FEM system equations in each time step. It shows that subcycling algorithm does not dramatically increases the Newton-Raphson iteration steps required to solve a large time increment for this case study. This is due to that in each Newton-Raphson iteration the local equilibrium in fine time scale region is always pursued by step 3 of subcycling algorithm, which is also the region of the highest non-linearity.

Factors of acceleration

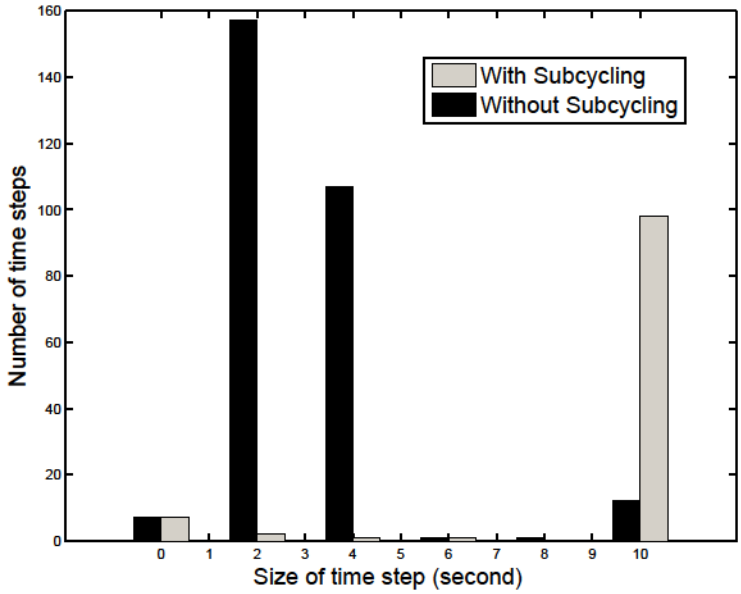

Figure 7.11: Distribution of time steps in the simulation with and without subcycling algorithm

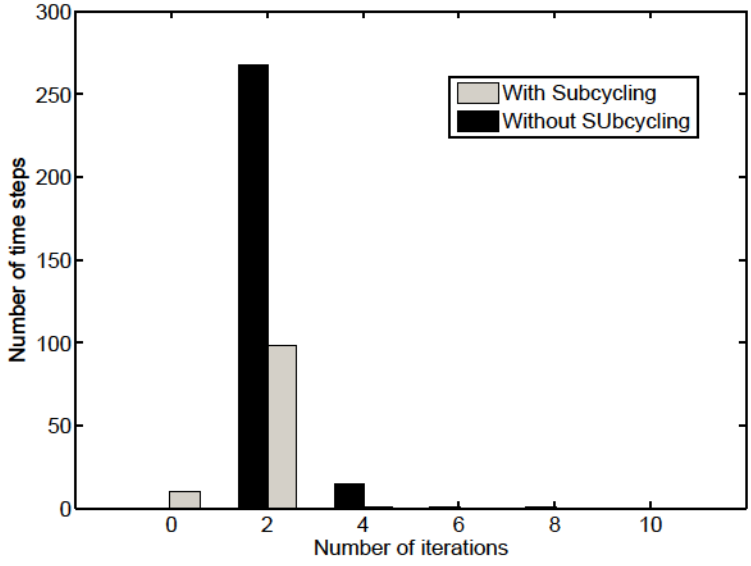

Figure 7.12: Distribution of number of Newton-Raphson iterations required for each time step

The factors which dominate the level of acceleration in subcycling algorithm is discussed in this section. The major computation time is limited by the number of operations for solving the non-linear FEM system equations in a serial CPFE simulation on a single processor. For the case study of small polycrystal, the nonlinear FEM system equation set is solved by a Newton-Raphson iterative method with LU decomposition as the direct solver. To solve the non-linear system from time t to $t + \Delta t$, the number of operations in the conventional CPFE simulation is $O\left(\left(N^F + N^C\right)^3 \frac{\Delta t}{\Delta \tau} m\right)$, where N^F and N^C are the number of degree of freedoms (DoFs) associated with the fine time-scale domain and coarse time scale domain respectively, and m is the number of Newton-Raphson iterations. Using subcycling algorithm, the number of operations is $O\left(\left(N^F\right)^3 \frac{\Delta t}{\Delta \tau} m^{sc} + \left(N^F + N^C\right)^3 m^{sc}\right)$, where m^{sc} is the number of Newton-Raphson iterations required when subcycling algorithm is applied. When a quasi-Newton method is adopted instead of full Newton-Raphson method, the LU decomposition only needs to be done once at the beginning of the time increment and both m m^{sc} can be omitted. Then the level of acceleration depends on $\frac{\Delta t}{\Delta \tau}$ and the ratio $\frac{N^C}{N^f}$. With larger $\frac{\Delta t}{\Delta \tau}$ and $\frac{N^C}{N^F}$, the level of acceleration is higher.

Parallel computing of CPFE model with subcycling algorithm

The subcycling algorithm is efficient for parallel computing. To demonstrate, the step 3 of subcycling algorithm which solves the local equilibrium of the fine time scale region

is performed on multiple threads. This established another advantage of the subcycling algorithm over the explicit substepping method [115]. The parallelization of substepping method is usually based on domain partition. The elements with localized deformation are distributed only in a few processors. In such situation, the substepping method only utilizes these processors to perform fine time step constitutive update while other processors wait in idle. The subcycling algorithm distributed the workload evenly on all processors and enhanced the parallelization efficiency. The polycrystal test in section 7.3.1 is performed on 2, 4, 8 and 16 processors with and without subcycling algorithm to verify the parallelization efficiency. The in-house parallel FE code is based on OpenMPI-1.4.3. The consumed CPU time is plotted in figure 7.13. When less number of processors are used, most of the computing time are spent on FE calculation and updating the constitutive laws; with the increase of processor numbers, the time consumed by MPI communication between processors increases. For this small polycrystal study, the optimum processor number is 8 for conventional CPFE simulation without subcycling. Exceeding 8 processors, the time spends on MPI communication overshoot the total computation time. For the CPFE simulation with subcycling, the optimum number of processors is also 8. Below 8 processors, the CPU time are reduced to nearly half of the cost of the conventional method. Above 8 processors, the time spent on communications dominates the total simulation time, and the increase of computation efficiency is not obvious. The CPFE studies of statistically equivalent representative volume element (SERVE) often requires large grain numbers and $10^5 - 10^6$ DoFs. The optimum number of processors for CPFE simulation of SERVEs is usually diffi-

cult to reach, and subcycling algorithm is expected to optimize the computational efficiency.

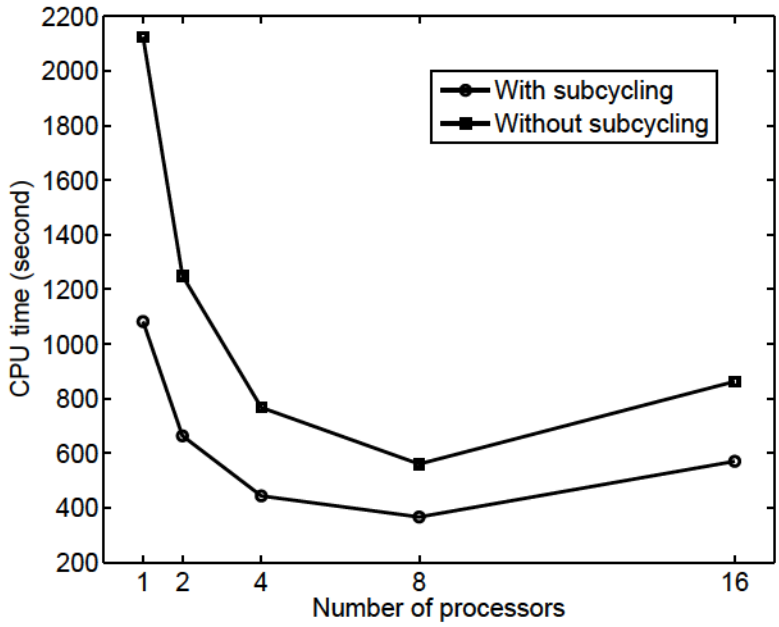

Figure 7.13: Computational CPU time for simulation with and without subcycling algorithm

7.4 Multi-time-domain CPFE Simulation of Mg Single Crystal with Micro-Twin Formation

The Mg single crystal tests with twin formations are performed in this section using implicit subcycling algorithm and explicit staggered update algorithm. The simulation aims to: 1, validate the accuracy and efficiency of subcycling algorithm when twin formations are activated; 2, verify the CPFE twin model. The applied load, boundary condition, crystal geometry and crystallography orientation is depicted in section 7.1.2 and figure 7.4a. The model parameter for twin propagation requires calibration with experiments. However,

this section aims to demonstrate the efficiency and accuracy of the subcycling algorithm and the capability of twin model, instead of comparing with experiments which remain a future work. The implicit subcycling algorithm follows the steps in section 7.2.2. The evolution of twin volume fraction, defined as the total volume of twinned elements over the volume of the model, is plotted up to 5% strain in figure 7.14 for three simulations, i.e. the simulation using explicit staggered algorithm with a fine time step of 1 second, a coarse time step of 10 seconds and with implicit subcycling algorithm with a time step of 10 second. Figure 7.4b demonstrates for this test time increment $\triangle t = 1$ predicts a converged result, thus serves as a reference solution. The simulation using explicit staggered twin update algorithm with coarse time step shows considerable deviation from the reference solution while the implicit subcycling algorithm shows very close results to the reference solution. Figure 7.15a plots the macroscopic stress-strain responses of the three simulations up to 10% strain. The macroscopic stress state remains as low as close to 100 MPa when deformation is dominated by the shearing from twin nucleations and propagations. At close to 5% strain twins almost occupy all volumes and start to saturate, as a result the dominated deformation mechanism switches to the $\langle c + a \rangle$ dislocation-slips and hardening rate increases rapidly due to the high shear resistance rates of slips. The typical "S" shape stress-strain curve for Mg alloys thus occurs. All three simulations predicted the change in deformation mechanisms and the "S" shape stress-strain curve. However, the simulation with explicit staggered twin update algorithm and coarse time step predicts higher stress before twin saturates. The simulation with implicit subcycling algorithm predicts identical

results to reference solution. Furthermore, a simulation with tensile loading applied along the x-axis is performed with subcycling algorithm, and the stress-strain curve is compared to the compression test results in figure 7.15b. The tensile loading along x-axis causes contraction in [0001] crystallographic direction which prohibits the formation of $\{10\bar{1}2\}$ twin and leads to a stress-strain response similar to the face-centered-cubic (fcc) materials. This is known as the tension-compression asymmetry caused by deformation twinning and is predicted by the proposed CPFE twin model.

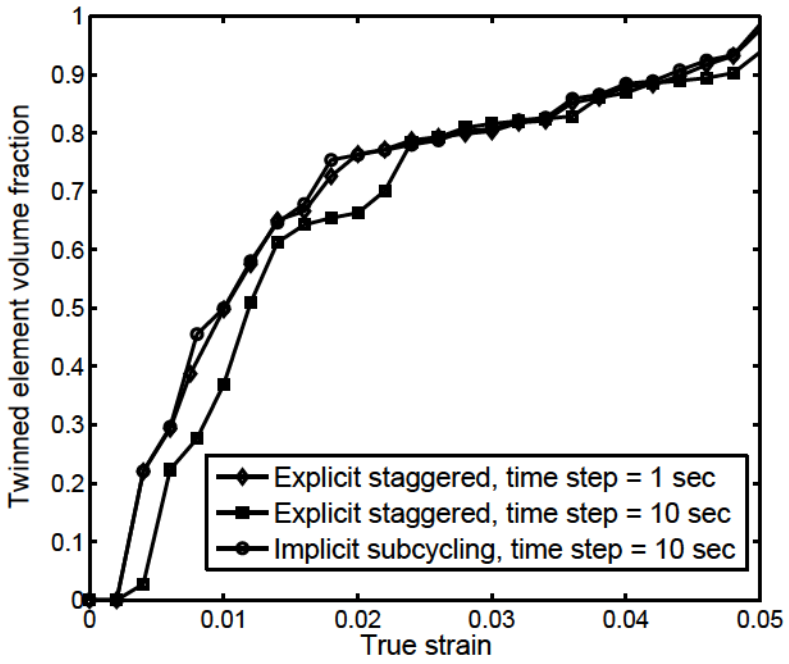

Figure 7.14: Evolution twinned volume fraction in simulations with explicit staggered twin update algorithm and implicit subcycling twin update algorithm

Figure 7.16 shows the twinned microstructure at 1% strain. Again the simulation with a fine time step $\triangle t = 1s$ and explicit staggered twin update algorithm is taken as reference solution, as shown in figure 7.16a. The Euler angle $[0^o, 7^o, 0^o]$ orientation of the

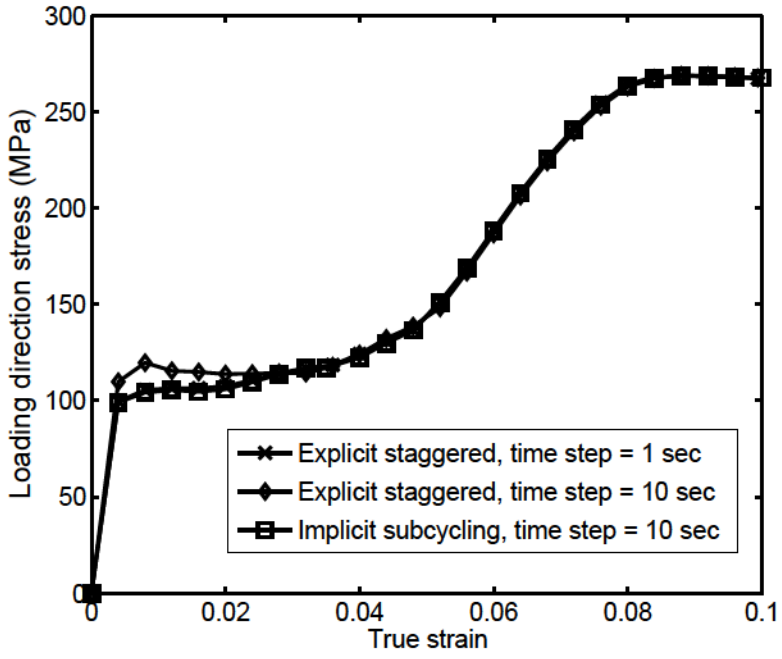

(a)

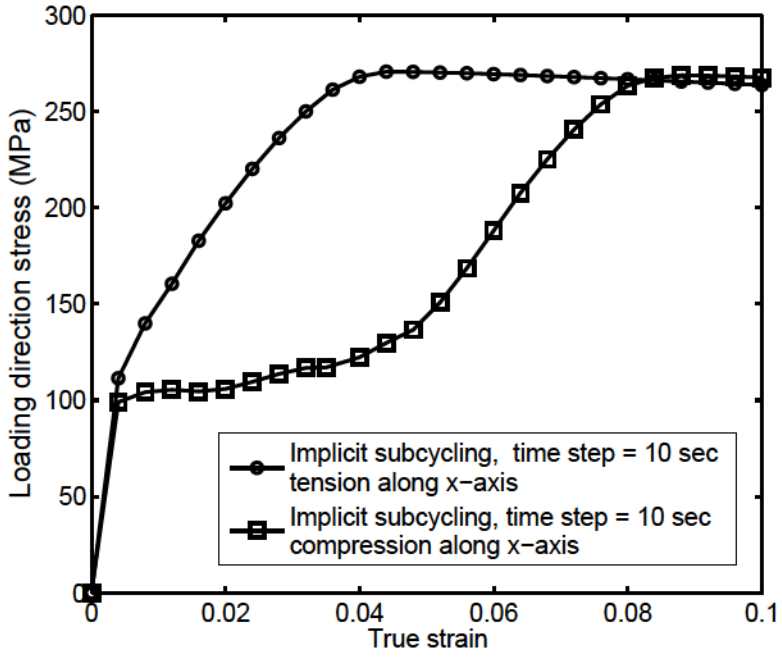

(b)

Figure 7.15: Simulation results of (a) stress and strain responses in single crystal test using explicit staggered twin update algorithm and implicit subcycling twin update algorithm (b) tension-compression asymmetry.

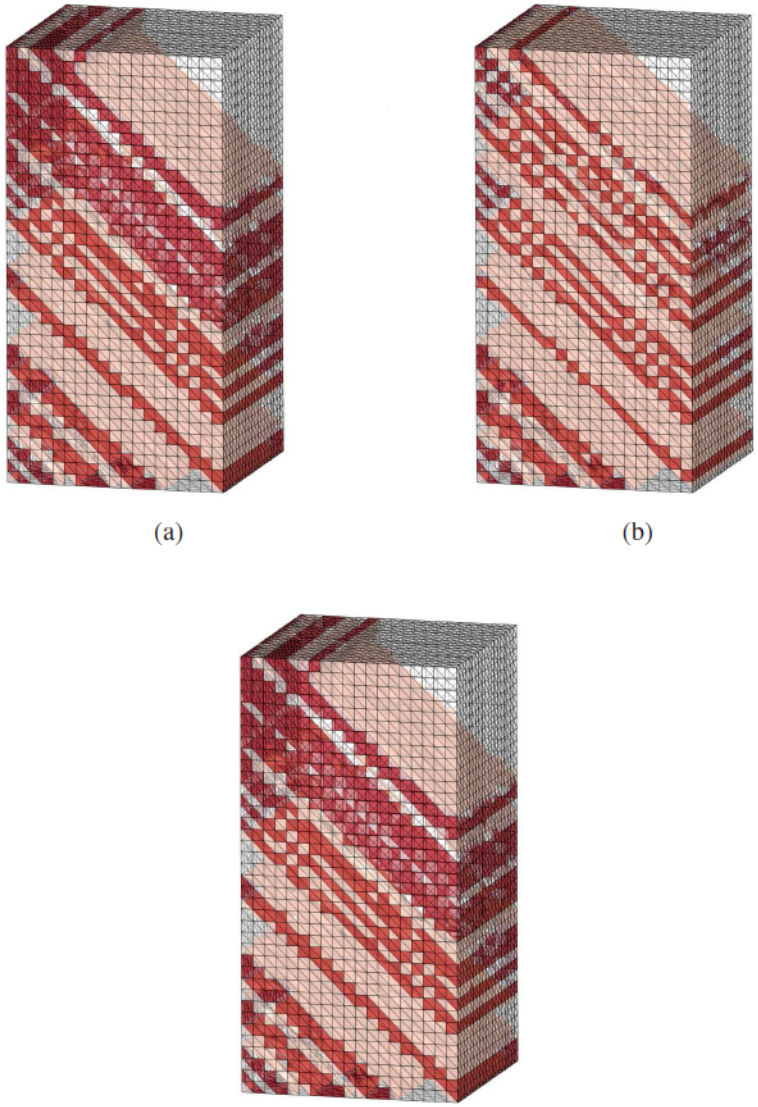

Figure 7.16: (a) Simulation result of twinned microstructure at 1% strain, using explicit staggered twin update algorithm with a fine time step $\Delta t = 1s$, (b) using explicit staggered twin update algorithm with a coarse time step $\Delta t = 10s$ (c) (a) using implicit subcycling twin update algorithm with a fine time step $\Delta t = 1s$

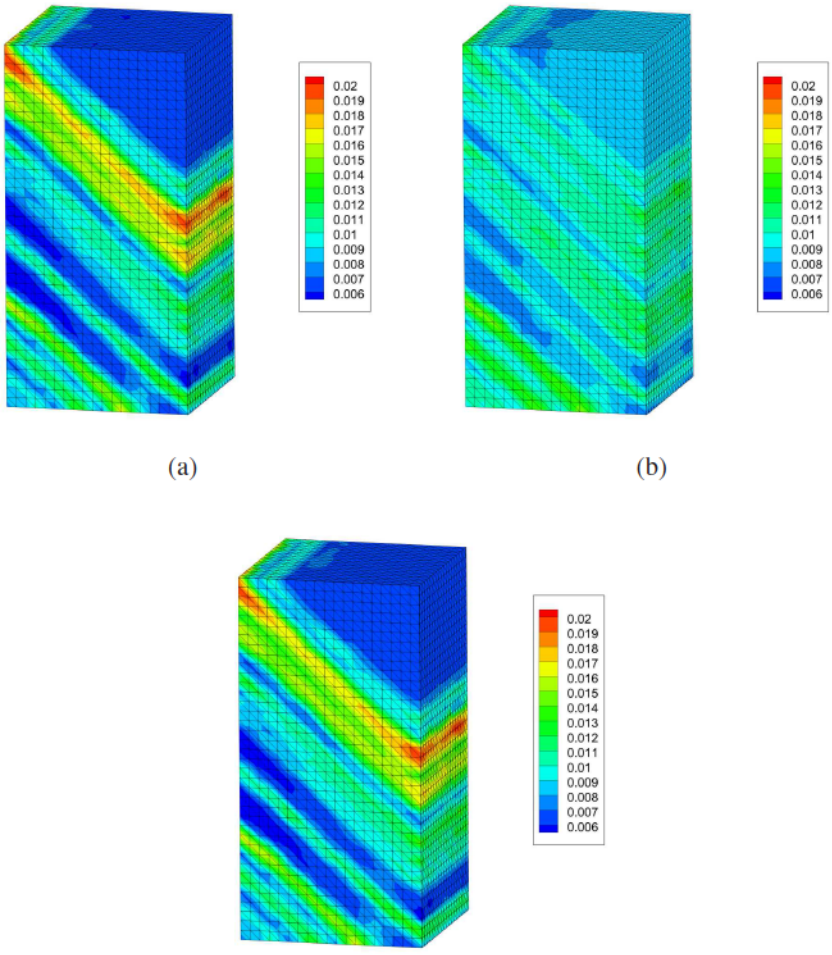

Figure 7.17: (a) Simulation result of local strain distribution at 1% strain, using explicit staggered twin update algorithm with a fine time step $\Delta t = 1s$, (b) using explicit staggered twin update algorithm with a coarse time step $\Delta t = 10s$ (c) (a) using implicit subcycling twin update algorithm with a fine time step $\Delta t = 1s$

single crystal causes the $\left(\bar{1}102\right)\left[1\bar{1}01\right]$ twin variant to have the highest Schmid factor than other tension twin variants which nucleates mostly. The only exception is that one $\left(10\bar{1}2\right)\left[\bar{1}011\right]$ twin variant occurs at the upper left corner of the model due to local stress state, as shown in reference solution (figure 7.16a) and subcycling accelerated simulation result (figure 7.16c). The simulation result with explicit staggered twin update algorithm and coarse time step $\triangle t = 10s$ in figure 7.16b does not capture this variant 4 twin formation. It also predicts a smaller twinned volume fraction than reference solution and subcycling solution. The simulation using implicit subcycling algorithm predicts almost the same twinned microstructures to the reference solution. The distributions of Green-Lagrangian strain component C_{11} at 1% strain are plotted in figure 7.17. The deformation localization is predicted within twin bands in the reference solution and the simulation using implicit subcycling twin update algorithm, but much weaker in the simulation using explicit staggered twin update algorithm. The plastic deformation requires gliding on twin systems or dislocation slips in $\langle c + a \rangle$ slip systems to compress the single crystal along the x-axis. The localized strain distribution is caused by the easy gliding of micro-twins in the twin region in contrast to the hard $\langle c + a \rangle$ dislocation slips with high resistance in the matrix region. The simulation with explicit staggered twin update algorithm predicts less heterogeneous deformation at 1% strain because it predicts late twin formations as explained in section 7.1.2. Table 7.3 tabulates the nucleation time of some twins in the three simulations. Again, the simulation with implicit subcycling twin update algorithm predicts much more accurate results than the simulation using explicit stagger twin update algorithm with coarse time step.

Explicit	$\Delta t = 1s$	Explicit	$\Delta t = 10s$	Implicit	$\Delta t = 10s$
twin ID	nucleation time	twin ID	nucleation time	twin ID	nucleation time
1	20s	1	20s	1	19.69s
2	20s	2	20s	2	19.69s
3	22s	3	30s	3	21.56s
4	23s	4	30s	4	22.81s
5	24s	5	30s	5	23.43s
6	26s	6	30s	6	25.18s
7	28s	7	30s	7	25.18s
8	28s	8	30s	8	27.06s
9	31s	9	40s	9	27.06s
10	37s	10	40s	10	36.56s

Table 7.3: Nucleation time of some twins in the three simulations in single crystal test.

In term of computation efficiency, the simulation using explicit staggered twin update algorithm and a fine time step of $\Delta t = 1s$ takes 4576 seconds to compute to 10% strain, while the simulation using implicit subcycling twin update algorithm takes 1273 seconds. 3.6 times acceleration is achieved using implicit subcycling algorithm without sacrificing accuracy. It is noted that the interactions between twins and grain boundaries are not accounted in this single crystal test, as well as the interactions between different twin variants. In polycrystal simulations, these intersections are important mechanisms for deformation localization and further aggravate the instabilities of CPFE calculation. As a result, the conventional CPFE twin simulation of the polycrystal microstructure suffers from even lower computation efficiency than single crystal tests. The test in next section demonstrates this phenomenon and shows the acceleration effect of subcycling algorithm in the CPFE twin simulations of polyrcrystal SERVE microstructure.

7.5 Multi-time-domain CPFE Simulation of AZ31 SERVE with Micro-Twin Formation

Micro-twin formation causes heterogeneous deformation and induces short crack initiation in the Mg alloy AZ31 polycrystalline microstructure [14]. This section examines the model efficiency using subcycling algorithm, as well as the model capability of features associated with twin-formation in the microstructure. The simulation is conducted in a high-resolution SERVE of AZ31, which contains 152 grains discretized into 699133 four node tetrahedrons consisting of 173512 nodes. The dimension of the SERVE is $50\mu m \times 50\mu m \times 50\mu m$. The average grain size is $10\mu m$. The SERVE is generated by matching morphological and crystallographic statistics with electron back-scattered diffraction (EBSD) data obtained from focused ion beam or FIB-based serial sectioning experiments on the AZ31 alloy in [100, 103]. The texture of the virtual microstructure is represented by the pole figures as shown in figure 7.18b. Uni-axial compressive loading with a constraint strain rate 1×10^{-4} is applied along y axis which is normal to transverse direction (TD) surface of the virtual microstructure. The minimum displacement boundary condition is applied to the opposite surface, as shown in figure 7.18a. The macroscopic stress-strain response from conventional CPFE simulations and the accelerated CPFE simulation with subcycling algorithm are compared in figure 7.18c. Almost identical results are observed between the two simulations. The conventional CPFE simulation takes 172832 seconds to compute the deformation up to 2% strain while the CPFE simulation with subcycling algorithm takes 29844 seconds to

compute to the same strain. 6 times acceleration are achieved for CPFE simulation with subcycling algorithm. This test demonstrates that the subcycling algorithm is essential to perform both accurate and efficient CPFE simulation with deformation twinning in high fidelity microstructure.

The twinned microstructure at 1% strain is shown in figure 7.19a. The distribution of Green-Lagrangian strain component C_{yy} and loading direction Cauchy stress σ_{yy} are plotted in figure 7.19b and figure 7.19c, respectively. Strain localization is clearly observed at the location of twin bands. The stress distribution has shown patterns related to twins. To exclude the effect of free surface, the simulation results are further examined at a slice on $y-z$ plane at position $x = 27\mu m$, as shown in figure 7.20. The first observation is that stress inside twin bands are lower than matrix region even with strain localization. This is due to that the plastic deformation in twins is dominated by shearing on twin system, which has a much lower resistance than slip on $\langle c+a \rangle$ system that dominates the deformation in matrix region. Important observation is that if a twin band intersects grain boundary the stress concentration is observed at the adjoining grain side close to the grain boundary-twin intersection, e.g. as circled by the dashed line in figure 7.20a and figure 7.20c. The examining the adjoining grain, a local strain concentration is observed at the same location in figure 7.20b. This is presumed to be the accommodation strain required for the continuous propagation of twin band as discussed in[119]. When the twin band propagations and increases in thickness, it carries a localized shear strain to the grain boundary, which needs to be accommodated by the deformation systems on the other grain side. If the twin systems

on the adjoining grain side are well aligned to the propagating twins, the shear strain can be accommodated by nucleating another twin and form a adjoining-twin-pair (ATP) [1]. Otherwise, the twin-induced shear strain must be accommodated by either easy basal slip systems or hard $\langle c + a \rangle$ slip systems, and the latter causes local stress concentrations. Such stress concentration can be responsible for the crack initiation at twin-grain boundary intersections observed in [14]. Stress concentration has also been observed at grain boundary triple junctions as shown in figure 7.20c.

7.6 Conclusion

In this chapter, the subcycling numerical time integration method is developed for multi-time-domain CPFE simulation of the twin formation and the heterogeneous deformation in the single crystal and polycrystalline microstructure. The subcycling method subdivides the simulation spatial domain into the deformation localized region which requires very fine numerical integration time steps, e.g. into the twins, and the rest bulk regions. Using a displacement predictor, separate FE simulations are conducted in the localized region with very fine time steps and on the rest bulk regions with coarse time steps, followed by coupling the residual forces and computing the displacement corrector every coarse time increment. The subcycling method accelerates the CPFE simulation of a small twin-free polycrystalline microstructure to 2 times faster. With the formation of twins taken into account, 3 times acceleration is observed in pure Mg single crystal and 6 times acceleration is observed in

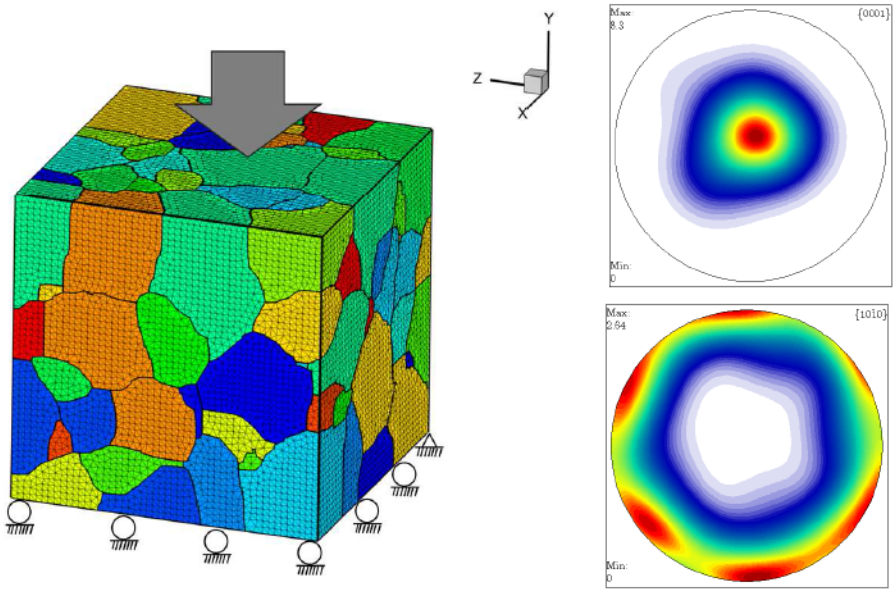

(a) (b)

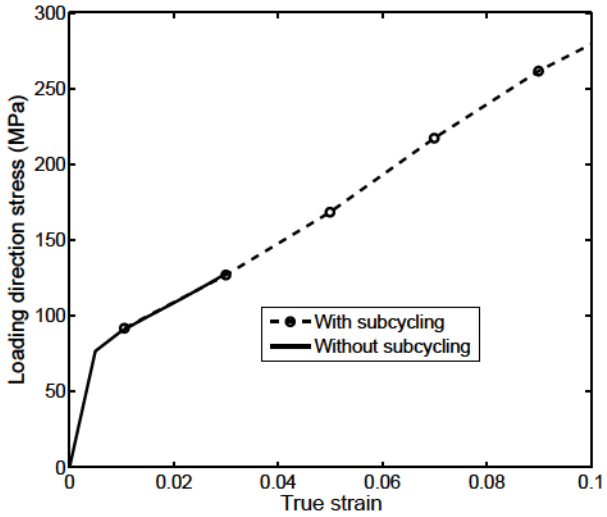

(c)

Figure 7.18: (a) Figure illustrating loading and boundary condition for the polycrystalline AZ31 RVE test. (b) Pole figures showing the texture of the AZ31 RVE (c) the stress-strain responses from simulations (d) microstructure with deformation twins at 1% strain

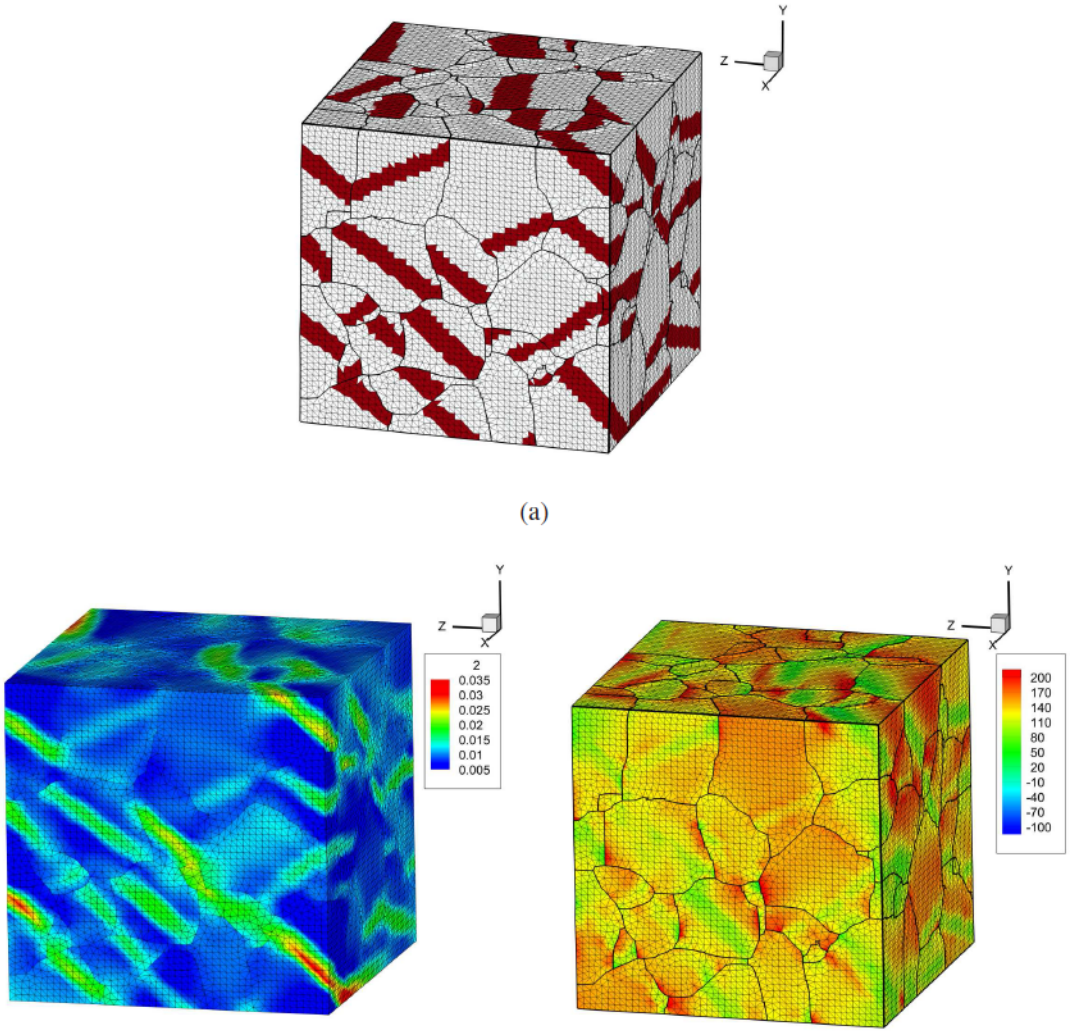

Figure 7.19: (a) Polycrystalline microstructure with twins at 1% strain predicted by CPFE twin simulation (b) distribution of loading direction stress σ_{yy} at 1% strain in the microstructure (d) distribution of loading direction Green-Lagrangian strain C_{yy} at 1% strain in the microstructure.

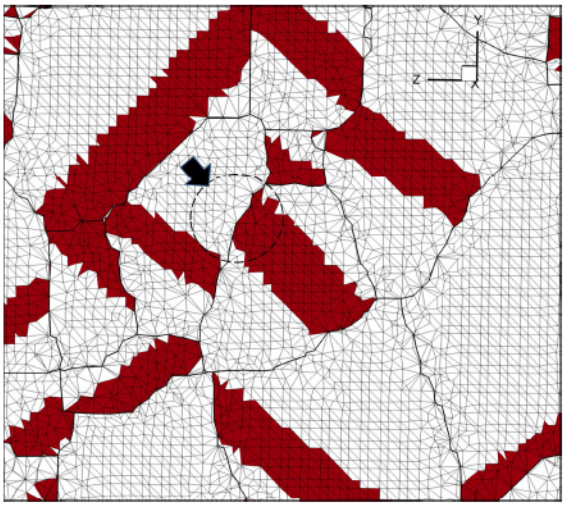

(a)

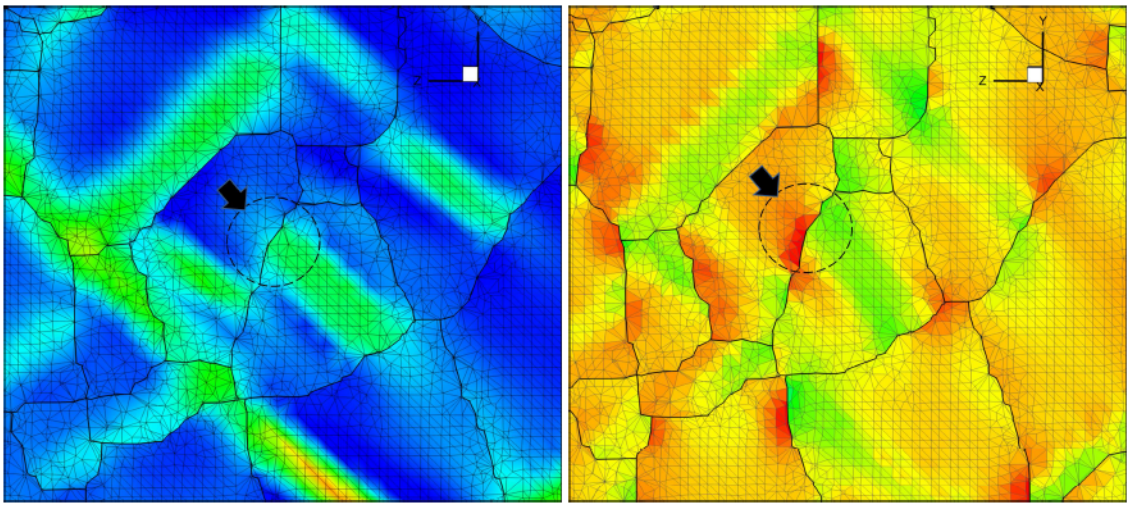

(b) (c)

Figure 7.20: (a) Microstructure with twins at 1% strain in a the slice in middle of RVE, predicted by CPFE twin simulation (b) distribution of loading direction stress $\sigma_Y Y$ at 1% strain in a the slice in middle of RVE (d) distribution of loading direction strain $\epsilon_Y Y$ at 1% strain in a the slice in middle of RVE

Mg alloy AZ31 polycrystalline microstructure. The simulation results with the subcycling method all match the reference solutions. The simulation in the Mg single crystal predicts the twin-induced "S" shape stress-strain curve and the tension-compression asymmetric response. Heterogeneous twin formations are predicted in the simulation of Mg alloy AZ31 polycrystalline SERVE microstructure and strain localization is observed in twin bands. The stress concentrates at twin-grain boundary intersections due to the accommodated strain at the untwinned grain side, which can be potentially responsible for micro-crack initiation at such locations observed in experiments.

Chapter 8

Conclusions and Future Work

In the present work, a physics-based modeling framework for deformation and micro-twin formation in the polycrystalline magnesium alloys has been developed by combining advanced computational mechanics and computational material science expertise. The crystal plasticity constitutive laws for crystallographic slip incorporate both the hardening effect from the evolution of statistically stored dislocations and geometrically necessary dislocations. The model predicts accumulation of dislocations and local stress concentrations at soft-hard grain boundaries, which sets the stage of modeling micro-twins nucleations. When subjected to large local stresses, the twin nucleation is assumed to take place under conditions of dissociation of a sessile $\langle c + a \rangle$ dislocation into a twin partial dislocation and a stair-rod dislocation. The nucleation criteria for CPFE simulation is governed by the energy of a stable equilibrium configuration after the dissociation, which should be smaller than the initial energy of the system at a large equilibrium dissociation distance. After a stable micro-twin nucleates, it forms a thin twin band microstructure by the gliding of partial twin dislocations on twin planes and migration from one twin plane to the adjacent twin planes. Criteria for twin propagation are derived from thermal activation laws describing the rate

of twin gliding assuming a shear-shuffle mechanism, as well as a stimulated slip model describing twin boundary migration. The plastic flow associated with twin propagation are described by modifying the crystal plasticity flow rule to incorporate rate of twinning and slip in the twin-reorientated lattice. These models are implemented into finite element analysis for simulating the explicit twin formation and the heterogeneous deformation in the twinned microstructure. It predicts heterogeneous twin formations that are sensitive to the underlying polycrystalline microstructures and are consistent with experimental observations.

Severe volumetric locking in 3D constant strain tetrahedral elements causes spurious large stress concentration and overestimates the formation of micro-twins. Two locally locking-free elements, i.e. locally integrated B-bar element, and the F-bar patch element, are developed based on the selectively integration of the constitutive relations to stabilize the CPFE simulation. Comprehension numerical tests are conducted to verify and validate the stabilized element formulation, including patch test, single crystal, bi-crystal and polycrystal with bending and constant strain rate loads. The F-bar patch element is preferred over locally integrated B-bar element for higher computation efficiency.

Strong deformation localization is observed in twin bands. In the simulation, locally high strain rate in the thin twin bands intensifies the time steps for the numerical integration of CPFE model and leads to enormously computation cost. A subcycling method is innovated for multi-time-scale integration of the CPFE twin model. The subcycling method splits the spatial domain into deformation localized regions that require very fine time steps and

regions with the loose requirement on time steps. Using a displacement predictor, separate FE simulations are conducted on the localized region with very fine time steps and on the rest bulk regions with coarse time steps, followed by coupling the residual forces and computing the displacement corrector every coarse time increment. $2to3$ times acceleration is observed by applying the subcycling algorithm to CPFE simulation of simple microstructures, and nearly 6 times acceleration is seen in the simulation of a realistic SERVE microstructure of Mg alloy AZ31.

The achievements in this dissertation are by no means an end but barely an advancement in the computational study of micro-twin formations and mechanical behavior of Mg alloys. Many sequels are required at this stage, including the further validation of the proposed twin propagation model with experiments, the model development for complex twin associated micro-mechanisms, and bridge between micro-twin formation model to the crack initiation in Mg alloys. The twin associated micro-mechanisms include twin-twin interaction, de-twinning, double-twinning, etc. New physics-based models are required when the mechanism of the twin nucleation under different conditions, alloy components, and microstructures are better characterized, and similar is on the twin boundary migrations mechanism due to dislocation-twin interactions. These works require novel model developments based on the close connection and cooperation between experiments, advance in computational material science knowledge and computational mechanics methods.

Bibliography

[1] I. J. Beyerlein, R. J. McCabe, and C. N. Tome. Effect of microstructure on the nucleation of deformation twins in polycrystalline high-purity magnesium: A multi-scale modeling study. *J. Mech. Phys. Solids*, 59:988–1003, 2011.

[2] C.J. Bettles and M.A. Gibson. Material rate dependence and localized deformation in crystalline solids. *Jour. Miner. Met. Mater. Soc.*, 57(5):46–49, 2005.

[3] K.U. Kainer. *Magnesium alloys and their applications*. Wiley-VCH, Weinheim, 2003.

[4] F. Kaiser, J. Bohlen, D. Letzig, K.U. Kainer, A. Styczynski, and C. Hartig. Influence of rolling conditions on the microstructure and mechanical properties of magnesium sheet az31. *Adv. Engng. Mater.*, 5(12):891–896, 2003.

[5] J. Bohlen, M. R. Nurnberg, J. W. Senn, D. Letzig, and S.R. Agnew. The texture and anisotropy of magnesium-zinc-rare-earth alloy sheets. *Acta Mater.*, 55:2101–2112, 2007.

[6] L.R. Barnett. Twinning and the ductility of magnesium alloys: Part i: Tension twins. *Mater. Sci. Engng.*, A464:1–7, 2007.

[7] L.R. Barnett. Twinning and the ductility of magnesium alloys: Part ii. contraction twins. *Mater. Sci. Engng.*, A464:8–16, 2007.

[8] D.W. Brown, A. Jain, S.R. Agnew, and B. Clausen. Twinning and detwinning during cyclic deformation of mg alloy az31b. *Materials Science Forum*, 539 - 543:3407–3413, 2007.

[9] Q. Ma, H. El Kadiri, A.L. Oppedal, J.C. Baird, M.F. Horstemeyera, and M. Cherkaouic. Twinning and double twinning upon compression of prismatic textures in an am30 magnesium alloy. *Scripta Mater.*, 64(9):813–816, 2011.

[10] H. El Kadiri, J. Kapil, A.L. Oppedal, L.G. Hector Jr., S.R. Agnew, M. Cherkaoui, and S.C. Vogel. The effect of twin-twin interactions on the nucleation and propagation of $\{10\bar{1}2\}$ twinning in magnesium. *Acta Mater.*, 61(10):3549–3563, 2013.

[11] J. Zhang and S. P. Joshi. Phenomenological crystal plasticity modeling and detailed micromechanical investigations of pure magnesium. *J. Mech. Phys. Solids*, 60:945–972, 2012.

[12] O. Duygulu and S.R. Agnew. Plastic anisotropy and the role of non-basal slip in magnesium alloy az31b. *Int. Jour. Plast.*, 21:1161–1193, 2005.

[13] J. Wang and C.N. Hirth, J.P.and TomÃť. $(\bar{1}012)$ twinning nucleation mechanisms in hexagonal-close-packed crystals. *Acta Mater.*, 57:5521–5530, 2009.

[14] Q. Yu, J. Zhang, and Y. Jiang. Fatigue damage development in pure polycrystalline

magnesium under cyclic tension-compression loading. *Materials Science and Engineering: A*, 528(25-26):7816 – 7826, 2011.

[15] J. W. Hutchinson. Bounds and self-consistent estimates for creep of polycrystalline materials. *Proc. R. Soc. Lond. A*, 348:101–127, 1976.

[16] A. Molinari, G. R. Canova, and S. Ahzi. A self consistent approach of the large deformation polycrystal viscoplasticity. *Acta Metall.*, 35:2983–2994, 1987.

[17] R. A. Lebensohn and C. N. Tome. A self-consistent anisotropic approach for the simulation of plastic deformation and texture development of polycrystals: Application to zirconium alloys. *Acta Metall. Mater.*, 41:2611–2624, 1993.

[18] R. A. Lebensohn and C. N. Tome. A self-consistent viscoplastic model: prediction of rolling textures of anisotropic polycrystals. *Mater. Sci. Eng. A*, 175:71–82, 1994.

[19] G. Proust, C.N. Tome, A. Jain, and S.R. Agnew. Modeling the effect of twinning and detwinning during strain-path changes of magnesium alloy {AZ31}. *Int. J. Plast.*, 25(5):861 – 880, 2009.

[20] H. Wang, P. D. Wu, C. N. Tome, and J. Wang. A constitutive model of twinning and detwinning for hexagonal close packed polycrystals. *Mater. Sci. Eng. A*, 555:93–98, 2012.

[21] B. Raeisinia and S.R. Agnew. Using polycrystal plasticity modeling to determine the

effects of grain size and solid solution additions on individual deformation mechanisms in cast mg alloys. *Scripta Mater.*, 58(4):613 – 624, 2010.

[22] H. El Kadiri and A.L. Oppedal. A crystal plasticity theory for latent hardening by glide twinning through dislocation transmutation and twin accommodation effects. *J. Mech. Phys. Solids*, 63(7):731–736, 2010.

[23] A.L. Oppedal, H. El Kadiri, C.N. Tome, G.C. Kaschner, S.C. Vogel, J.C. Baird, and M.F. Horstemeyer. Effect of dislocation transmutation on modeling hardening mechanisms by twinning in magnesium. *Int. J. Plast.*, 30-31(0):41 – 61, 2012.

[24] Milovan Zecevic, Marko Knezevic, Irene J. Beyerlein, and Carlos N. TomÃľ. An elasto-plastic self-consistent model with hardening based on dislocation density, twinning and de-twinning: Application to strain path changes in {HCP} metals. *Materials Science and Engineering: A*, 638:262 – 274, 2015.

[25] J.D. Clayton and J. Knap. A phase field model of deformation twinning: Nonlinear theory and numerical simulations. *Physica D: Nonlinear Phenomena*, 240(9-10):841 – 858, 2011.

[26] J.D. Clayton and J. Knap. Phase-field analysis of fracture-induced twinning in single crystals. *Acta Materialia*, 61(14):5341 – 5353, 2013.

[27] Vaibhav Agrawal and Kaushik Dayal. A dynamic phase-field model for structural transformations and twinning: Regularized interfaces with transparent prescription

of complex kinetics and nucleation. part i: Formulation and one-dimensional characterization. *Journal of the Mechanics and Physics of Solids*, 85:270 – 290, 2015.

[28] Vaibhav Agrawal and Kaushik Dayal. A dynamic phase-field model for structural transformations and twinning: Regularized interfaces with transparent prescription of complex kinetics and nucleation. part ii: Two-dimensional characterization and boundary kinetics. *Journal of the Mechanics and Physics of Solids*, 85:291 – 307, 2015.

[29] A. Staroselsky and L. Anand. A constitutive model for hcp materials deforming by slip and twinning: application to magnesium alloy {AZ31B}. *Int. J. Plast.*, 19(10):1843 – 1864, 2003.

[30] S. Graff, W. Brocks, and D. Steglich. Yielding of magnesium: From single crystal to polycrystalline aggregates. *Int. J. Plast.*, 23:1957–1978, 2007.

[31] A. Izadbakhsh, K. Inal, R. K. Mishra, and M. Niewczas. New crystal plasticity constitutive model for large strain deformation in single crystals of magnesium. *Model. Simul. Mater. Sci. Eng.*, 50:2185–2202, 2011.

[32] A Izadbakhsh, K. Inal, and R. K. Mishra. Crystal plasticity based finite element modelling of large strain deformation in am30 magnesium alloy. *Model. Simul. Mater. Sci. Eng.*, 20:035016, 2012.

[33] H. Abdolvand and M. R. Daymond. Multi-scale modeling and experimental study of

twin inception and propagation in hexagonal close-packed materials using a crystal plasticity finite element approach-part i: average behavior. *J. Mech. Phys. Solids*, 61:783–802, 2013.

[34] Milan Ardeljan, Rodney J. McCabe, Irene J. Beyerlein, and Marko Knezevic. Explicit incorporation of deformation twins into crystal plasticity finite element models. *Computer Methods in Applied Mechanics and Engineering*, 295:396 – 413, 2015.

[35] A. Serra, R. C. Pond, and D. J. Bacon. Computer simulation of the structure and mobility of twinning dislocations in hcp metals. *Acta Metll. Mater.*, 39:1469, 1991.

[36] J. S. Koehler, F. Seitz, W. T. JR. Read, W. Shockley, and E. Orowan. *Dislocations in Metals*. American Institute of Mining and Metallurgical Engineers. Institute of Metals Division, 1st edition, 1954.

[37] S Mendelson. Dislocation dissociation in hcp metals. *Jour. Appl. Phys*, 41(5):1893–1910, 1970.

[38] L. C. Capolungo and I. J. Beyerlein. Nucleation and stability of twins in hcp metals. *Phys. Rev. B*, 78:024117, 2008.

[39] I. J. Beyerlein and C. N. Tome. A probabilistic twin nucleation model for hcp polycrystalline metals. *Proc. R. Soc. A*, 466:2517–2544, 2010.

[40] M. Ghazisaeidi and W. A. Curtin. Analysis of dissociation of $< c >$ and $< c +$

a > dislocations to nucleate $\{10\bar{1}2\}$ twins in mg. *Model. Simul. Mater. Sci. Eng.*, 21:055007, 2013.

[41] N. Thompson and D. J. Millard. Twin formation, in cadmium. *Philos. Mag.*, 43:422–440, 1952.

[42] J. P. Hirth and J. Lothe. *Theory of Dislocations*. Wiley-Interscience, 2nd edition, 1982.

[43] Haitham El Kadiri, Christopher D. Barrett, Jian Wang, and Carlos N. TomÃĺ. Why are twins profuse in magnesium? *Acta Materialia*, 85:354 – 361, 2015.

[44] Fulin Wang and Sean Agnew. Dislocation-twin interactions in magnesium alloy az31. *Magnesium Technology 2015*, pages 139–144, 2015.

[45] Haidong Fan, Sylvie Aubry, Athanasios Arsenlis, and Jaafar A. El-Awady. The role of twinning deformation on the hardening response of polycrystalline magnesium from discrete dislocation dynamics simulations. *Acta Materialia*, 92:126 – 139, 2015.

[46] A. Staroselsky and L. Anand. A constitutive model for hcp materials deforming by slip and twinning: application to magnesium alloy az31b. *Int. J. Plast.*, 19:843–1864, 2003.

[47] E. Busso, F. Meissonier, and N. OâĂŹDowd. Gradient-dependent deformation of two-phase single crystals. *Jour. Mech. Phys. Solid.*, 48(11):2333–2361, 2000.

[48] C. Zambaldi, F. Roters, D. Raabe, and U. Glatzel. Modeling and experiments on the indentation deformation and recrystallization of a single-crystal nickel-base superalloy. *Mater. Sci. Engng. A*, 454-455:433–440, 2007.

[49] F. Roters, P. Eisenlohr, L. Hantcherli, D.D. Tjahjantoa, T.R. Bieler, and D. Raabe. Overview of constitutive laws, kinematics, homogenization and multiscale methods in crystal plasticity finite-element modeling: Theory, experiments, applications. *Acta Mater.*, 58(4):1152–1211, 2010.

[50] R.J. Asaro and A. Needleman. Texture development and strain hardening in rate dependent polycrystals. *Acta Mater.*, 33(6):923–953, 1985.

[51] U.F. Kocks, A.S. Argon, and M.F. Ashby. Thermodynamics and kinetics of slip. *Progress in materials science*, 19:141–145, 1975.

[52] V. Hasija, S. Ghosh, M. J. Mills, and D. S. Joseph. Modeling deformation and creep in Ti-6Al alloys with experimental validation. *Acta Mater.*, 51:4533–4549, 2003.

[53] D. Deka, D. S. Joseph, S. Ghosh, and M. J. Mills. Crystal plasticity modeling of deformation and creep in polycrystalline Ti-6242. *Metall. Trans. A.*, 37A(5):1371–1388, 2006.

[54] G. Venkataramani, S. Ghosh, and M. J. Mills. A size dependent crystal plasticity finite element model for creep and load-shedding in polycrystalline Titanium alloys. *Acta Mater.*, 55:3971–3986, 2007.

[55] G. Venkataramani, K. Kirane, and S. Ghosh. Microstructural parameters affecting creep induced load shedding in Ti-6242 by a size dependent crystal plasticity FE model. *Int. Jour. Plas.*, 24:428–454, 2008.

[56] M. Anahid, M. K. Samal, and S. Ghosh. Dwell fatigue crack nucleation model based on crystal plasticity finite element simulations of polycrystalline Titanium alloys. *Jour. Mech. Phys. Solids*, 59(10):2157–2176, 2011.

[57] S. Ghosh and P. Chakraborty. Microstructure and load sensitive fatigue crack nucleation in ti-6242 using accelerated crystal plasticity fem simulations. *Int. Jour. Fatigue*, 48:231 – 246, 2013.

[58] S. Sinha and S. Ghosh. Modeling cyclic ratcheting based fatigue life of hsla steels using crystal plasticity fem simulations and experiments. *Int. Jour. Fatig.*, 28:1690–1704, 2006.

[59] S. Keshavarz and S. Ghosh. Multi-scale crystal plasticity fem approach to modeling nickel based superalloys. *Acta Mater.*, 61:6549–6561, 2013.

[60] K.J. Bathe. *Finite element procedures*. Prentice-Hall, Inc, 1996.

[61] E. W. Kelley and W. F. Hosford. Plane-strain compression of magnesium and magnesium alloy crystals. *Trans. Metall. Soc. AIME*, 242:5–13, 1968.

[62] B. Li and E. Ma. Pyramidal slip in magnesium: Dislocations and stacking fault on the $\{10\bar{1}1\}$ plane. *Philos. Mag.*, 89:1223–1235, 2009.

[63] Q. Ma, H. El Kadiri, A.L. Oppedal, J.C. Baird, M.F. Horstemeyera, and S.C. Vogel. Twinning effects in a rod-textured am30 magnesium alloy. *Int. J. Plast.*, 29(0):60–76, 2012.

[64] U. F. Kock, A. S. Argon, and M. F. Ashby. Thermodynamics and kinetics of slip. *Prog. Mater Sci.*, 19, 1975.

[65] D. J. Kim, D. Y. Ryu, N. A. Bojarczuk, J. Karasinski, S. Guha, S. H. Lee, and J. H. Lee. Thermal activation energies of mg in gan: Mg measured by the hall effect and admittance spectroscopy. *J. Appl. Phys.*, 88:2564, 2000.

[66] M. F. Ashby. Deformation of plastically non-homogeneous maaterials. *Philos. Mag.*, 21:399–424, 1970.

[67] A. Ma, F. Roters, and D. Raabe. A dislocation density based constitutive model for crystal plasticity fem including geometrically necessary dislocations. *Acta Mater.*, 54:2169–2179, 2006.

[68] P. Castany, F. Pettinari-Sturmel, J. Douin, and A. Coujou. In situ transmission electron microscopy deformation of the titanium alloy ti-6al-4v: Interface behaviour. *Mater. Sci. Eng., A*, 483:719–722, 2008.

[69] A. Arsenlis. *Modeling Dislocation Density Evolution in Continuum Crystal Plasticity*. PhD thesis, Massachusetts Institute of Technology, 2001.

[70] A. Arsenlis and D. M. Parks. Crystallographic aspects of geometrically-necessary and statistically-stored dislocation density. *Acta Mater.*, 47:1597–1611, 1998.

[71] FT. Meissonnier, EP. Busso, and NP. O'Dowd. Finite element implementation of a generalised non-local rate-dependent crystallographic formulation for finite strains. *Int. J. Plast.*, 17:601 – 640, 2001.

[72] O. C. Zienkiewicz and J. Z. Zhu. The superconvergent patch recovery (spr) and adaptive finite element refinement. *Comput.Method Appl M*, 101:207 – 224, 1992.

[73] *Simmetrix*. http://www.simmetrix.com/, 2014.

[74] K. MatouÅą and A.M. Maniatty. Finite element formulation for modelling large deformations in elasto-viscoplastic polycrystals. *Int. J. Numer. Meth. Eng.*, 60:2313 – 2333, 2004.

[75] CR. Dohrmann, MW. Heinstein, J. Jung, SW. Key, and WR. Witkowski. Node-based uniform strain elements for three-node triangular and four-node tetrahedral meshes. *Int. J. Numer. Meth. Eng.*, 47:1549 – 1568, 2000.

[76] M.W. Gee, C.R. Dohrmann, S.W. Key, and W.A. Wall. A uniform nodal strain tetrahedron with isochoric stabilization. *Int. J. Numer. Meth. Eng.*, 78:429 – 443, 2009.

[77] E.A. de Souza Neto, F.M. Andrade Pires, and D.R.J. Owen. F-bar-based linear

triangles and tetrahedra for finite strain analysis of nearly incompressible solids. part i: formulation and benchmarking. *Int. J. Numer. Meth. Eng.*, 62:353 – 383, 2005.

[78] E.A. de Souza Neto, D. Peric, and D.R.J. Owen. *Computational methods for plasticity: theory and applications*. John Wiley and Sons Ltd., 2008.

[79] J. Bonet, H. Marriott, and O. Hassan. Stability and comparison of different linear tetrahedral formulations for nearly incompressible explicit dynamic applications. *Int. J. Numer. Meth. Eng.*, 50:119 – 133, 2001.

[80] M. A. Puso and J. Solberg. A stabilized nodally integrated tetrahedral. *Int. J. Numer. Meth. Eng.*, 67:841 – 867, 2006.

[81] G. Laschet, I. Caylak, S. Benke, and R. Mahnken. Locally integrated node-based formulations for four-node tetrahedral meshes. *Private communication*, 2015.

[82] G.R. Liu, T. Nguyen-Thoi, H. Nguyen-Xuan, and K.Y. Lam. A node-based smoothed finite element method (ns-fem) for upper bound solutions to solid mechanics problems. *Comput. struc.*, 87:14–26, 2009.

[83] H. Nguyen-Xuan and G.R. Liu. An edge-based smoothed finite element method softened with a bubble function (bes-fem) for solid mechanics. *Comput. struc.*, 128:14–30, 2013.

[84] G.R. Liu, T. Nguyen-Thoi, and Lam K.Y. An edge-based smoothed finite element

method (es-fem) for static, free and forced vibration analyses of solids. *J Sound Vib*, 320:1100–1130, 2009.

[85] T. Nguyen-Thoi, G.R. Liu, Lam K.Y., and Zhang G.Y. A face-based smoothed finite element method (fs-fem) for 3d linear and non-linear solid mechanics problems using 4-node tetrahedral elements. *Int. J. Numer. Meth. Eng.*, 78:324–353, 2009.

[86] E.A. de Souza Neto, D. Peric, M. Dutko, and D.R.J. Owen. Design of simple low order finite elements for large strain analysis of nearly incompressible solids. *Int. J. Solids Struct.*, 33:3277 – 3296, 1996.

[87] Wolff S. and Bucher C. A finite element method based on c0 continuous assumed gradients. *Int. J. Numer. Meth. Eng.*, 86:876–914, 2011.

[88] R. Mahnken and I. Caylak. Stabilization of bi-mixed finite elements for tetrahedral with enhanced interpolation using volume and area bubble functions. *Int. J. Numer. Meth. Eng.*, 75:377–413, 2008.

[89] R. Mahnken, I. Caylak, and G. Laschet. Two mixed finite element formulations with area bubble functions for tetrahedral elements. *Comput. Meth. in Appl. Mech. And Eng.*, 197:1147–1165, 2008.

[90] MA Crisfield. *nonlinear finite element analysis of solids and structures, Volume 1: Essentials*. John Wiley and Sons, Inc, 1997.

[91] T.J.R. Hughes. *The finite element method: linear Static and dynamic finite element analysis*. Prentice-Hall, Inc, 1987.

[92] J. Cheng and S. Ghosh. A crystal plasticity fe model for deformation with twin nucleation in magnesium alloys. *Int. J. Plast.*, 67(0):148 – 170, 2015.

[93] Xiaoye S. Li. An overview of superlu: Algorithms, implementation,and user interface. *Trans. Math. Soft.*, 31(3):302–325, 2005.

[94] M. A. Groeber and M. A. Jackson. Dream.3d: A digital representation environment for the analysis of microstructure in 3d. *Integrating Materials and Manufacturing Innovation*, 3:5, 2014.

[95] B. Bhattacharya. *Plastic deformation behavior of pure magnesium in the temperature range 4.2K-300K*. PhD thesis, McMaster University, 2006.

[96] C. L. Xie, S. Ghosh, and M. Groeber. Modeling cyclic deformation of hsla steels using crystal plasticity. *J. Eng. Mater. Technol.*, 126:339–352, 2004.

[97] T. Obara, H. Yoshinga, and S. Morozumi. $\{11\bar{2}2\}(\bar{1}\bar{1}23)$ slip system in magnesium. *Acta Metall.*, 21:845–853, 1973.

[98] S. Ando, M. Tsushida, and H. Kitahara. Deformation behavior of magnesium single crystal in c-axis compression and a-axis tension. *Mater. Sci. Forum*, 654-656:699–702, 2010.

[99] B. Bhattacharya and M. Niewczas. Work-hardening behaviour of mg single crystals oriented for basal slip. *Philos. Mag.*, 91:2227–2247, 2011.

[100] A. S. Khan, A. Pandey, T. Gnaupel-Herold, and R. K. Mishra. Mechanical response and texture evolution of az31 alloy at large strains for different strain rates and temperatures. *Int. J. Plast.*, 27:688–706, 2011.

[101] M. Groeber, S. Ghosh, M. D. Uchic, and D. M. Dimiduk. A framework for automated analysis and simulation of 3d polycrystalline microstructures.: Part 1: Statistical characterization. *Acta Mater.*, 56(6):1257–1273, 2008.

[102] M. Groeber, S. Ghosh, M. D. Uchic, and D. M. Dimiduk. A framework for automated analysis and simulation of 3d polycrystalline microstructures. part 2: Synthetic structure generation. *Acta Mater.*, 56(6):1274–1287, 2008.

[103] R. Mishra and K. Inal. Microstructure data. Unpublished work, 2013.

[104] I. J. Beyerlein, L. Capolungo, P. E. Marshall, R. J. McCabe, and C. N. Tome. Statistical analyses of deformation twinning in magnesium. *Philos. Mag.*, 90:2161–2190, 2010.

[105] P.E. Marshall, G. Proust, J.T. Rogers, and R. McCabe. Automatic twin statistics from electron backscattered diffraction data. *Jour. Microsc.*, 238(3):218–229, 2010.

[106] M. A. Meyers, O. Vohringer, and V. A. Lubarda. The onset of twinning in metals: a constitutive description. *Acta. Mater.*, 49:4025 – 4039, 2001.

[107] E. Schmid and W. Boas. *Plasticity of Crystals*. Hughes and Co., 1950.

[108] S. Ghosh and M. Anahid. Homogenized constitutive and fatigue nucleation models from crystal plasticity fe simulations of ti alloys, part 1: Macroscopic anisotropic yield function. *Int. Jour. Plast.*, 47:182–201, 2013.

[109] M. Anahid and S. Ghosh. Homogenized constitutive and fatigue nucleation models from crystal plasticity fe simulations of ti alloys, part 2: Macroscopic probabilistic crack nucleation model. *Int. Jour. Plast.*, 48:111–124, 2013.

[110] Niewczas M. Strong crystal size effect on deformation twinning. *Nature Letters.*, 463:08692, 2010.

[111] D. Hull and D. J. Bacon. *Introduction to Dislocations*. Butterworth-Heinemann, 4th edition, 2001.

[112] Niewczas M. Lattice correspondence during twinning in hexagonal close-packed crystals. *Acta Mater.*, 58:5848–5857, 2010.

[113] S. Balasubramanian. *Polycrystalline Plasticity: Application to Deformation Processing of Lightweight Metals*. PhD thesis, Massachusetts Institute of Technology, 1998.

[114] Zhang K., Hopperstad O. S., Holmedal B., and Dumoulin S. A robust and efficient substepping scheme for the explicit numerical integration of a rate-dependent crystal plasticity model. *Int. J. Numer. Meth. Eng.*, 99:239–262, 2014.

[115] Ling X., Horstemeyer M. F., and Potirniche G.P. On the numerical implementation

of 3d rate-dependent single crystal plasticity formulations. *Int. J. Numer. Meth. Eng.*, 63:548–568, 2005.

[116] Kuchnick S.N., Cuitino1 A. M., and Radovitzky R.A. Efficient and robust constitutive integrators for single-crystal plasticity modeling. *Int. J. Plasticity*, 22(10):1988 – 2011, 2006.

[117] Roters F., Eisenlohr P., and Bieler. T.R. *Crystal plasticity finite element methods in materials science and engineering*. Wiley-VCH Verlag GmbH, 2010.

[118] Majkut M. *A study of deformation twinning in magnesium alloy AZ31B*. PhD thesis, Queen's University, 2013.

[119] John J. Jonas, Sijia Mu, Talal Al-Samman, GÃijnter Gottstein, Lan Jiang, and ÄŰtienne Martin. The role of strain accommodation during the variant selection of primary twins in magnesium. *Acta Materialia*, 59(5):2046 – 2056, 2011.

Vita

1984 ..... Born Chengde, Hebei, China.

2008 ..... B.S. Department of Physics and Astronomy, Shanghai Jiaotong University, Shanghai, China.

2009-2011 ..... Graduate Research Assistant. The Ohio State University, Columbus, Ohio, U.S.

2011-2016 ..... Graduate Research Assistant. The Johns Hopkins, University, Baltimore, Maryland, U.S.